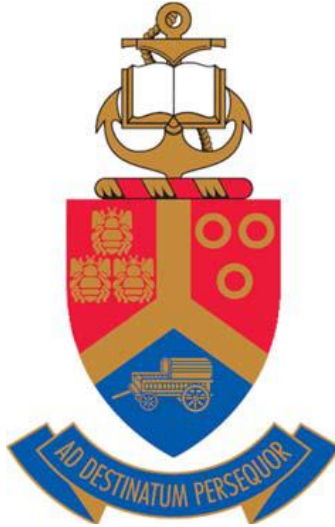# Structural and electrical properties of annealed Ru thin films on SiC

by

Kinnock Vundawaka Munthali

Submitted in partial fulfilment of the requirements for the degree of

DOCTOR OF PHILOSOPHY IN PHYSICS

In the Department of Physics in the Faculty of
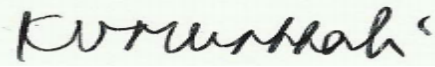Natural and Agricultural Sciences at the

University of Pretoria

July 2016

Supervisor: Prof. C.C. Theron
Co-supervisor: Prof. F. D. Auret

DECLARATION

I, **Kinnock Vundawaka Munthali**, declare that the thesis/dissertation, which I hereby submit for the degree **DOCTOR OF PHILOSOPHY (PhD) IN PHYSICS** at the University of Pretoria, is my own work and has not previously been submitted by me for a degree at this or any other tertiary institution.

Signature: _KVmunthali_   **Date:** **14 July 2016**

SUMMARY

Structural and electrical properties of annealed Ru thin films on SiC

by

Kinnock Vundawaka Munthali

Supervisor: Prof. C. C. Theron
Co-supervisor: Prof. F. D. Auret

Submitted in partial fulfilment of the requirements for a degree **DOCTOR OF PHILOSOPHY (PhD) IN PHYSICS** in the Faculty of Natural and Agricultural Sciences, **University of Pretoria.**

Silicon carbide (SiC) is both used as a diffusion barrier in Tristructural Isotropic (TRISO) coated nuclear fuel particles in nuclear reactors and as a wide band gap semiconductor in microelectronics applications. SiC has physical properties of high strength and hardness, high melting point and is chemically inert.

This thesis investigates the effectiveness of SiC as a barrier to ruthenium diffusion in TRISO coated nuclear fuel particles. In addition, the electrical performance and degradation mechanism of ruthenium-SiC based Schottky barrier diodes (SBDs), and their ability to operate at extremely high temperatures are also investigated.

In TRISO coated fuel particles, the high strength SiC layer acts as a containment layer to the high pressure generated in the kernel by the fission nuclear reaction. One element produced during the nuclear fission reaction is ruthenium (Ru). In this thesis, the Ru solid state reaction with SiC has been investigated by annealing a thin film of Ru on 4H-SiC and 6H-SiC in the air, argon and a vacuum. Analysis of the thin films after various annealing temperatures were performed by Rutherford Backscattering Spectrometry, X-Ray Diffraction analysis, Scanning electron microscopy, and Raman Spectroscopy. The study has shown that diffusion of Ru into SiC starts at a much higher annealing temperature in a vacuum, whereas, in air annealing, diffusion commences at a much lower temperature. The study has shown that SiC is not a perfect barrier to the diffusion of metallic fission products.

Due to its wide band gap property, electronic devices made from SiC can operate at very high temperatures, with very high power and fast switching times. Ru also happens to be a suitable material for making Schottky contacts with SiC. Due to its high melting temperature (2250°C), and chemical inertness, the Ru Schottky contact can function at very high operating temperatures.

The electrical characteristics of Ru/SiC SBDs have been investigated by annealing the diodes in various environments namely air, argon and vacuum. The electrical characterisation of the SBDs after each annealing temperature was done by using current-voltage (IV) and capacitance-voltage (CV) characterisation techniques. This study has shown that Ru/4H-SiC SBDs will remain operational after annealing in vacuum up to temperatures of above 1000 ^{o}C and that the diodes degrade at a very low temperature of 400 ^{o}C when annealed in air. Ru/4H-SiC SBDs under argon annealing degrade at a temperature of 1000 ^{o}C. The degradation of the Ru/4H-SiC SBDs, when annealed in air, is explained by the fact that there is a possibility of formation of an oxide of Ru which is not conducting which leads to a high series resistance of the diode at the degradation temperature of 400 ^{o}C. In the case of argon annealing, the degradation of Ru/4H-SiC SBDs is due to the diffusion of Ru into 4H-SiC.

In a vacuum, the Ru/6H-SiC SBDs degrade at a temperature of 800 ^{o}C. The IV data show that Ru Schottky contact on 6H-SiC becomes ohmic at 900 ^{o}C. The formation of an ohmic contact is attributed to the formation of graphite flakes as evidenced by Raman analysis of Ru/6H-SiC thin films.

In atmospheric annealing environment, the Ru/6H-SiC SBDs degrade at a higher temperature (of 700 ^{o}C) than that of Ru/4H-SiC SBDs (400 ^{o}C).

Under argon annealing, there is very little difference in the degradation temperature between Ru-4H-SiC and Ru/6H-SiC SBDs. This study has shown that, in general, the SBDs degrade at higher temperatures when annealed in vacuum and argon while in air degradation takes place at a very much lower temperature.

Keywords:

To

MY LATE SON, SANGWANI MUNTHALI

Acknowledgements

I would like to thank my supervisors Prof. C.C. Theron and Prof. F. D. Auret for their guidance and support. I would also like to thank the University of Pretoria for the financial support. I am also grateful to the following people:
- Dr Sergio Coelho for his help in fabricating Schottky diodes, and thin film deposition.
- Dr Linda Prinsloo for her help in Raman Analysis.
- Ms Wiebke Grote for her help in XRD analysis.
- Fellow PhD student Dr Eric Njoroge for RUMP simulations.
- My wife and daughters for their moral support.

CONTENTS

4. RESULTS FOR SOLID STATE REACTION AND DIFFUSION OF RUTHENIUM IN 6H-SIC AND 4H-SIC UNDER DIFFERENT ANNEALING ENVIRONMENTS.

5. RESULTS ON OPERATIONAL STABILITY OF Ru/6H-SiC AND Ru/4H-SiC SCHOTTKY BARRIER DIODES ANNEALED IN THE AIR, ARGON AND A VACUUM.

CHAPTER 1

RESEARCH INTRODUCTION

1.1 Introduction

SiC when compared with silicon, has superior qualities of a large band gap, high breakdown electric field, high thermal conductivity, high saturation carrier velocity, and high mechanical strength [1]. Due to these properties, SiC-based diodes and electronic devices can operate at extreme temperature conditions such as in avionics, microwaves, high voltage switching, deep sea wells and space rockets. The wide band gap property of SiC (3.0 eV for 6H and 3.2 eV for 4H) finds applications in the emission (this has applications in quantum computing) and detection of short wavelength light [1, 2]. SiC's properties of high breakdown electric field ($2.2x10^6$ V/cm and $2.4x10^6$ V/cm for 4H–SiC and 6H–SiC respectively) and high thermal conductivity (4.9 W/cmK for 6H and 4H) are ideal for high voltage, high power and high packing density of discrete electronic devices [1]. Sic Schottky rectifiers have a large reverse breakdown voltage, high turn-off speed due to their minimal reverse recovery current flow, and ability to handle large current flow [3].

One of the important parameters of a Schottky barrier diode (SBD) is the Schottky barrier height (SBH). The SBH determines the electrical character of an ohmic or Schottky contact. An ohmic contact is important for making outside interconnection to a device. A good ohmic contact will exhibit a linear and symmetric current–voltage relationship for both positive and negative voltages, and its resistance compared with the bulk of the device will be negligible. A low SBH generally creates good ohmic contact while a large SBH will lead to a good Schottky contact [4].

Ruthenium (Ru) has a high melting point (2250° C), high chemical stability, low electrical resistance, high mechanical resistance to abrasion and fatigue [5]. These properties make Ru a good candidate as a Schottky contact for high-temperature operation Schottky barrier diodes. At such high operating temperatures, there is a high possibility of occurrence of chemical reactions and diffusion of elements at the interface of the Schottky contact and SiC. However, there has been limited literature on the solid state reaction of Ru with SiC and its linkage with the electrical performance of Ru Schottky contacts. In addition, minimal attempts have been made by researchers in determining the failure mechanisms of the Ru/SiC Schottky diodes at high operating temperatures. Stuchlikova *et al* [1] studied the behavior of RuO_2 Schottky contacts on 4H-SiC by sputter-deposition of Ru, in an oxygen/argon environment and at a temperature of 500° C, on 4H-SiC. The authors found the SBH of the Schottky contact to be 0.88 eV and ideality factor to be 1.28 at 300 K. The main thrust of the authors' work was on the electrical characterisation of the Schottky contacts and no studies on interface properties were carried out. Buc *et al* [5] also characterised RuO_2 Schottky contacts on 4H-SiC under similar experimental conditions like those of reference 1 (with the exception that the samples were characterised at

different temperatures).The researchers only used electrical characterisation techniques in analysing the Schottky contacts. They found the SBH of the Schottky contacts to be 0.88 eV. In a separate experiment, Buc *et al* [6] investigated the behaviour of RuO_2 Schottky contacts on 4H-SiC at different annealing temperatures in a nitrogen environment. The authors found that the forward turn-on voltage of the Schottky diodes shifted upwards from 1 V to 1.8 V with reducing the temperature from 450 K to 83 K. They also found out that the ideality factor decreased with increasing annealing temperature. It should be mentioned that the researchers, just like in the previously mentioned cases, only used electrical characterisation tools in the analysis of the Schottky contacts. Roy *et al* [7] investigated the thermal stability of Ru- β -SiC contacts at different annealing temperatures in a hydrogen/air environment. The researchers used Rutherford backscattering spectrometry (RBS), x-ray diffraction technique (XRD) and secondary ion mass spectrometry (SIMS) to characterise the Ru-SiC interface. The authors found that Ru oxidation and its diffusion into SiC commenced at an annealing temperature of $800\,^{\circ}$ C. The researchers, in this case, did not clearly link the interface changes to the electrical performance of the Schottky contact. Venter *et al* [8] performed the electrical investigation of the behaviour of Ru Schottky contacts on 6H-SiC at different annealing temperatures in the argon environment. The authors found that the SBH varied from 0.95 to 1.35 eV in a temperature range of 25 to $400\,^{\circ}$ C. No attempt was made to link the behaviour of the diodes to interface changes in this case as well.

Apart from explaining the behaviour of the Ru Schottky interface, microstructure investigation of Ru-SiC interface has other applications in nuclear reactors. This is due to the fact that SiC is also used as a layer in tristructural isotropic (TRISO) coated fuel particles in high-temperature nuclear reactors because of its properties of high mechanical strength, chemical inertness, and high melting temperature. The purpose of TRISO fuel configuration is to act as a containing vessel of actinides and fission products so as to reduce the risk of leakage and coolant contamination [9]. The TRISO coated fuel particle (Fig. 1) is a microsphere which consists of a fuel kernel surrounded by a buffer layer of low-density carbon, followed by layers of inner pyrolytic carbon (IpyC), silicon carbide and outer pyrolytic carbon (OpyC). Each TRISO coating layer has a special function, but SiC is the most important layer that provides most of the structural strength and dimensional stability and acts as the main barrier of metallic fission products.

OUTER PYROCARBON

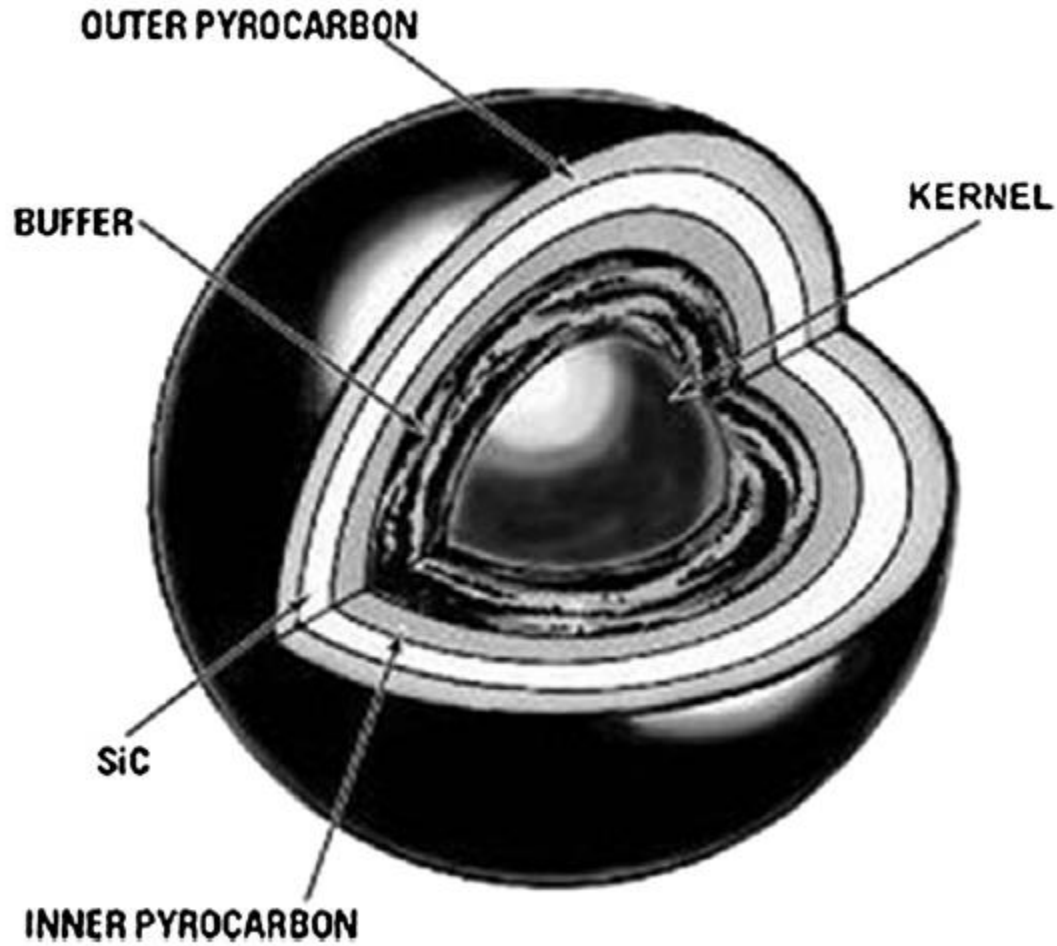KERNEL

BUFFER

SiC

INNER PYROCARBON

Fig. 1 Schematic of TRISO fuel particle [9].

Metals such as ruthenium, rhodium, palladium, molybdenum, technicium, and silver are produced with high yields during the fission of uranium and plutonium oxide fuels [9, 10]. A number of researchers have studied the diffusion of these elements in SiC. Olivier *et al* [11] investigated the reaction of Pd with different types of SiC at typical high-temperature gas cooled nuclear-reactor (HTGR) operating temperatures. They found that there was a formation of palladium silicide. Penetration and transport of palladium silicides into SiC along grain boundaries were also observed. Neethling *et al* [12] studied the behavior of palladium-silver compound which were in contact with 3C-SiC and 6H-SiC. The researchers found that silver together with palladium penetrated polycrystalline SiC along grain boundaries. They suggested that silver transport in SiC took place along grain boundaries in the form of moving nodules which consisted of silver and palladium combined together.

Minato *et al* [13], in their experiments on zirconium carbide TRISO-coated uranium dioxide fuel particles, found a substantial release of ^{106}Ru when compared to other released fission products of cesium and europium. Its fraction increased from 0.13 at 1600 ºC for 4500 h to 0.86 at 1800 ºC for 3000 h. Measurements by a gamma ray spectrometer at the Chernobyl nuclear disaster area indicated the existence of ruthenium radionuclides mainly composed of the following isotopes ^{103}Ru and ^{106}Ru [14]. However, the vast literature on fission metal interaction with SiC is concentrated on three metals namely palladium, caesium and silver [15-23]. There is a dearth of literature on the solid state reaction and transport of ruthenium in the SiC layer of TRISO coated fuel particles.

1.2 Research Scope

This research was divided into two broad investigations. One part of the investigation dealt with the electrical performance of ruthenium Schottky diodes made from SiC after annealing in three different environments namely air, argon and vacuum. The other part of the investigation involved the microstructure characterisation of the Ru-SiC interface so as to determine the occurrence (or not) of the interface changes, phase formation, and diffusion processes.

The electrical investigation of the diodes attempted to fill the gaps in the reviewed Ru/SiC Schottky diodes literature. To this end, the research mainly investigated the behaviour of Ru Schottky contacts on n-type 4H-SiC and 6H-SiC in three different annealing environments (namely air, argon, and vacuum) and attempted to find the impact of interface changes of Ru-SiC Schottky contacts on the electrical performance of the diodes. The study investigated the following questions:

- When the temperature of the Ru Schottky contact is increased, what changes take place at the Ru/SiC interface? And what is the linkage between these changes and the electrical performance of the Schottky diode?

- At extremely high temperatures, the Schottky junction is likely to degrade and fail, and when this happens, what are the likely causes of the electrical degradation of the junction?
- In which annealing environment will the Ru-Schottky diode achieve its highest temperature of operation before degradation kicks in?
- In terms of the Schottky junction stability, which SiC polytype is better suited for a high-temperature operation?

The microstructure characterisation part of investigation attempted to achieve two aims of the study. One aim was to determine the effectiveness of SiC as a barrier to ruthenium transport, as SiC is used as a containment layer in TRISO coated nuclear fuel particles. To this end, an investigation of the microstructure evolution of the Ru/SiC layer after the annealing process was carried out to determine the occurrence of diffusion, the products that result from the reactions and phase transformations. This part of the research basically investigated these research questions:

- How effective is the SiC layer as a diffusion barrier in TRISO coated fuel particles?
- What are the products of solid state reaction at the Ru-SiC interface when annealed in the three different environments of air, argon, and a vacuum?

The other aim of this part of the investigation was to link interface changes and electrical performance of the Schottky diodes as discussed above.

The structure of the thesis is as follows. The theoretical background of semiconductor device physics and an introduction to metal interactions with SiC are given in Chapter 2. Chapter 3 gives information on the experimental techniques that were used in this research. The results of the study are outlined in Chapter 4 and chapter 5. Chapter 6 gives the overall general summary, conclusion, and future work.

1.3 References

[1] L. Stuchlikova, D. Buc, L. Harmatha, U. Helmersson, W. H. Chang, I. Bello, *Deep energy levels in RuO₂/4H–SiC Schottky barrier structures*, Applied Physics Letters 88, 153509, (2006).

[2] F. Fuchs, V. A. Soltamov, S.Vath, P. G. Baranov, E. N. Mokhov, G. V. Astakhov, V. Dyakonov, *Silicon carbide light-emitting diode as a prospective room temperature source for single photons*, Scientific Reports, 3, 1637, (2013).

[3] M. Bhatnagar, B.J. Baliga, *Comparison of 6H-SiC, 3C-SiC and Si for power devices*, IEEE Transactions on Electronic Devices, Vol. 40, No. 3, (1993).

[4] F. La Via, F. Roccaforte, A. Makhtari, V. Raineri, P. Musumeci, L. Calcagno, *Structural and electrical characterization of titanium and nickel silicide contacts on silicon carbide*, Microelectronic Engineering 60 269–282, (2002).

[5]   D. Buc, L. Stuchlikova, U. Helmersson, W.H. Chang, I. Bello I, *Investigation of RuO2/4H–SiC Schottky diode contacts by deep level transient spectroscopy*, Chemical Physics Letters 429 617–621 (2006).

[6] D. Buc, L. Stuchlikova, L. Harmatha, I. Hotovy, *Electrical characterization of 4H–SiC Schottky diodes with a RuO$_2$ and a RuWO$_x$ Schottky contacts*, J Mater Sci: Mater Electron 19:783–787 (2008).

 [7] S. Roy, C. Jacob, M. Zhang, S. Wang, A.K. Tyagi, S. Basu, *SIMS, RBS and glancing incidence X-ray diffraction studies of thermally annealed Ru/β-SiC interfaces*, Applied Surface Science **211** 300–307 (2003).

 [8] A. Venter, M. E. Samiji, A. W. R. Leitch, *Thermal stability of Ru, Pd and Al Schottky contacts to p-type 6H-SiC*, Phys. stat. sol. (c) **1**, No. 9, 2264– 2268, (2004).

[9] T.M. Besmann, R.E. Stoller, G. Samolyuk, P.C. Schuck, S.I. Golubov, S.P. Rudin, J.M. Wills, J.D. Coe, B.D. Wirth, S. Kim, D.D. Morgan, I. Szlufarska, *Modelling Deep Burn TRISO particle nuclear fuel*, Journal of Nuclear Materials 430 181-189, (2012).

[10] X.W. Zhou, C.H. Chang, *Current status and future development of coated fuel particles for high temperature gas-cooled reactors*, Progress in Nuclear Energy 53 182-188, (2011).

[11] E.J. Olivier, J.H. Neethling, *Palladium transport in SiC*, Nuclear Engineering and Design Volume 244, 25–33, (2012).

[12] J.H. Neethling, J.H. O'Connell, E.J. Olivier, *Palladium assisted silver transport in polycrystalline SiC*, Nuclear Engineering and Design**, Volume 251, Pages 230–234, (2012).

[13] K. Minato, T. Ogawa, T. Koya, H. Sekino, T. Tomita, *Retention of fission product caesium in ZrC-coated fuel particles for high-temperature gas-cooled reactors*, Journal of Nuclear Materials, 279, 181–188, (2000).

[14] R. Pollanen, *Highly radioactive ruthenium particles released from the Chernobyl accident-particle characteristics and radiological hazard*, Radiation Protection Dosimetry vol. 71 No.1, pp. 23-32, (1997).

[15] D. Shrader, S.M. Khalil, T. Gerczak, T. R. Allen, A. J. Heimc, I. Szlufarska, D. Morgan, *Ag diffusion in cubic silicon carbide*, Journal of Nuclear Materials, 408 257–271, (2011).

[16] K. Minato, K. Fukuda, A. Ishikawa, N. Mita, *Advanced coatings for HTGR fuel particles against corrosion of layer*, Journal of Nuclear Materials 246 215-222, (1997).

[17] P. Demkowicz, K. Wright, J. Gan, D. Petti, *High temperature interface reactions of TiC, TiN, and SiC with palladium and rhodium*, Solid State Ionics 179, 2313–2321,(2008).

[18] J. Rabone, E. López-Honorato, *Density functional theory metadynamics of silver, caesium and palladium diffusion at 3C-SiC grain boundaries*, Journal of Nuclear Materials, 458 56–63, (2015).

[19] I. J. van Rooyen, T. M. Lillo, Y. Q. Wu, *Identification of Silver and Palladium in Irradiated*, TRISO Coated Particles of the AGR-1 Experiment, Journal of Nuclear Materials, DOI:10.1016/j.jnucmat.2013.11.028, (2014).

[20] E. Lopez-Honorato, D. Yang, J. Tan, P.J. Meadows, P. Xiao, *Silver Diffusion in Coated Fuel Particles*, Journal of American Ceramic Society, 93, [10], 3076–3079, (2010).

[21] J.H. O'Connell, J.H. Neethling, *Ag transport in high temperature neutron irradiated 3C–SiC*, Journal of Nuclear Materials, 445, 20–25, (2014).

[22] A. Londono-Hurtado, A. J. Heim, S. Kim, I. Szlufarska, D. Morgan, *Cs and Ag co-incorporation in cubic silicon carbide*, Journal of Nuclear Materials 439, 65–71, (2013).

[23] T.M. Lillo, I.J. van Rooyen, *Associations of Pd, U and Ag in the SiC layer of neutron-irradiated TRISO fuel*, Journal of Nuclear Materials 460, 97–106, (2015).

CHAPTER 2

THEORETICAL BACKGROUND

2.1 Introduction

This chapter provides background information on semiconductor theory, properties of silicon carbide, ruthenium, and nickel. TRISO coated fuel particles are briefly introduced. Section 2.2 describes the crystal structure of SiC while section 2.3 outlines the physical and electrical properties of SiC. Sections 2.4 and 2.5 briefly describe the properties of ruthenium and nickel respectively. Metal-semiconductor junctions theory is discussed in section 2.6 and finally section 2.7 outlines metal-SiC interactions.

2.2 Crystal Structure of Silicon carbide

Silicon carbide has over 200 polytypes which basically depend on how the Si-C close-packed atomic planes are stacked. In this thesis, two polytypes of SiC have been used for investigations namely 4H-SiC and 6H-SiC. The core structural unit of all SiC polytypes is the covalently-bonded tetrahedron with either SiC_4 or CSi_4 [1]. This core structural unit is shown in Fig 2.1.
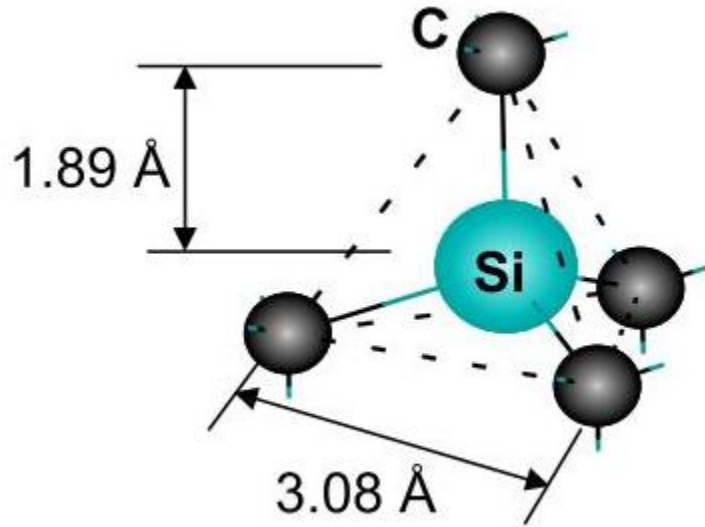
Fig 2.1 SiC core structural unit [1].

The Si-C tetrahedral basic unit is periodically repeated in hexagonal bilayers, with C-Si single bonds being perpendicular to the basal plane. The various polytypes are identified by the stacking sequence and the Ramsdell notation is used. A single stacked bilayer is indicated with letters A, B and C. The polytype 3C has a cubic structure with an ABC stacking sequence whereas the 2H, 4H, and 6H polytypes have hexagonal structures with an AB, ABAC, ABCACB stacking sequence respectively as illustrated in Fig 2.2 [2]. All the polytypes of SiC are referred to in a hexagonal coordinate system which is made up of three a-plane coordinates a1, a2, and a3, and a c-axis coordinate (Fig 2.3) [3]. An interesting feature of silicon carbide is its polarity along the c – axis, where a surface perpendicular to the c-axis (for example the (0001) face in 4H–SiC) is made of Si atoms, the opposite surface (000$\underline{1}$) is composed solely of C atoms, with different chemical properties. These surfaces are denoted as "Si–face" and "C–face" respectively [4].
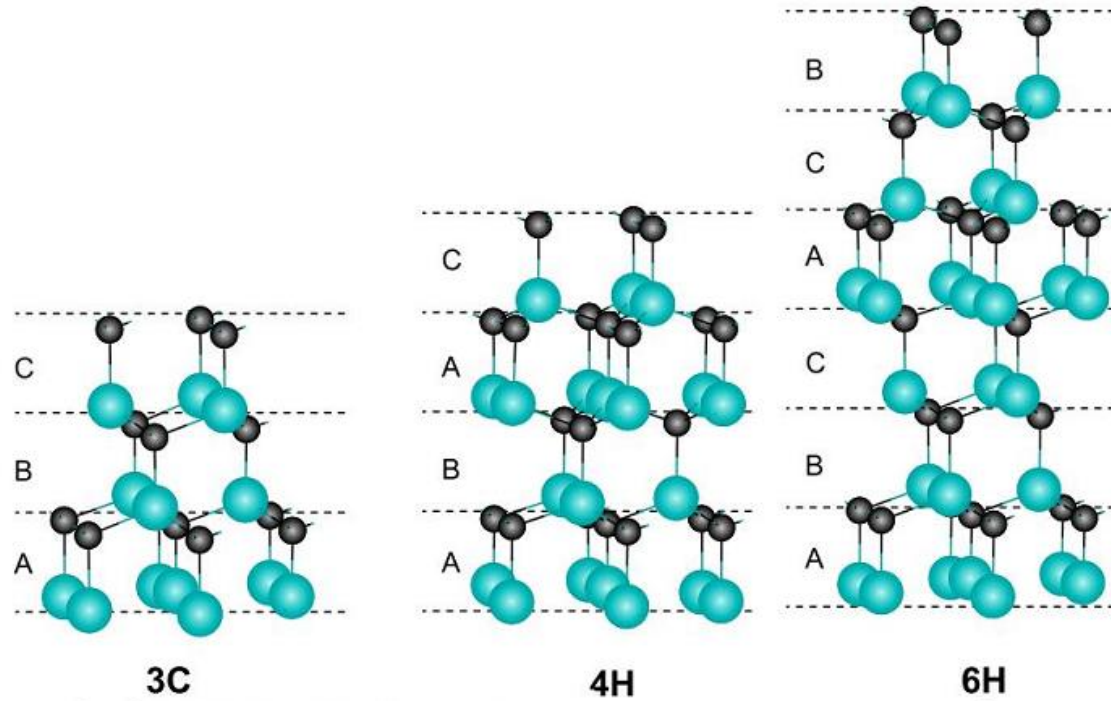
Fig 2.2 3C, 4H, and 6H polytypes stacking sequence [2].
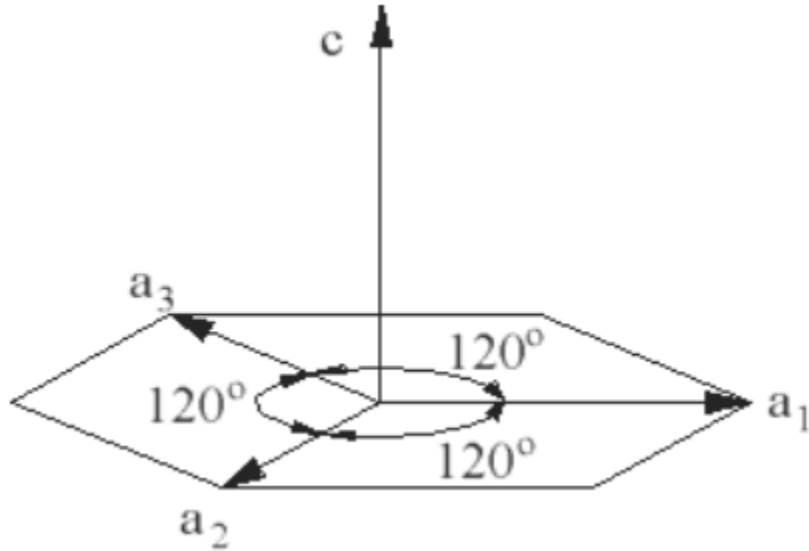
Fig 2.3 The Miller indices describing the hexagonal structure [3].

4H-SiC and 6H-SiC are the most common hexagonal polytypes. 4H-SiC is made up of equal amounts cubic and hexagonal bonds whereas 6H-SiC is two-thirds cubic [3].

2.3 Properties of SiC
2.3.1 Introduction

Silicon carbide, when compared with silicon, has a large band gap, high breakdown electric field, high thermal conductivity, high saturation carrier velocity, and high mechanical strength [4]. These properties make SiC-based diodes and electronic devices operate at extreme temperature conditions such as in avionics, microwaves, high voltage switching, deep sea wells and space rockets.

2.3.2 Electrical Properties of SiC

Table 1 compares the electrical properties of silicon carbide with other types of semiconductors [2].

Wide band gap

SiC has a band gap which is almost three times that of silicon. This means that for an electron to be excited from the valence band to the conduction band, it will require three times the excitation energy of that of silicon. This means that SiC-based devices can operate at very high temperature without thermal breakdown. The wide band gap property of SiC (3.0 eV for 6H and 3.2 eV for 4H) finds applications in high power electronic circuits.

High breakdown electric field

The high breakdown electric field (2.2×10^6 V/cm—4H–SiC, 2.4×10^6 V/cm—6H–SiC) and high thermal conductivity (4.9 W/cmK for 6H and 4H) properties of SiC are ideal for high voltage, high power and high packing density of discrete electronic devices. Due to its high electron mobility power devices can operate at high frequencies [4]. Wide band gap materials have high breakdown electric field due to the fact that wide band gap requires high impact ionisation energy [2].

Table 1 Comparison of properties of SiC with other semiconductors [2, 5].

Property	Si	GaAs	GaN	3C-SiC	6H-SiC	4H-SiC
Bandgap, E_g (eV at 300K)	1.12	1.43	3.4	2.4	3.0	3.2
Critical field, E_c (V/cm)	$2.5 \cdot 10^5$	$3 \cdot 10^5$	$3 \cdot 10^6$	$2 \cdot 10^6$	$2.5 \cdot 10^6$	$2.2 \cdot 10^6$
Thermal Conductivity, λ (W/cmK at 300K)	1.5	0.5	1.3	3-4	3-4	3-4
Saturated electron drift velocity, v_{sat} (cm/s)	$1 \cdot 10^7$	$1 \cdot 10^7$	$2.5 \cdot 10^7$	$2.5 \cdot 10^7$	$2 \cdot 10^7$	$2 \cdot 10^7$
Electron mobility, μ_n (cm^2/V·s)	1350	8500	1000	1000	500	950
Hole mobility, μ_p (cm^2/V·s)	480	400	30	40	80	120
Dielectric constant, ε_r	11.9	13.0	9.5	9.7	10	10
Breakdown voltage (V)	300	500	6000	-	19200	19200

2.3.3 Physical and chemical properties of SiC

Mechanical strength and hardness

SiC has high mechanical strength. It has a high elastic modulus which decreases with increasing porosity and impurity concentration [1]. The elastic modulus E at room temperature is a function of porosity V_p and is expressed as

$$E = E_o \exp(-CV_p)$$ (2.1)

Where E_o is the elastic modulus of pore-free SiC and C is a constant.
At high temperatures elastic modulus is given by

$$E = E_O - BT \exp(-\frac{T_O}{T})$$ (2.2)

Where B and T_o are constant characteristics of the material with units of GPaK^{-1} and K respectively.

SiC is a covalently bonded material and has a very high hardness. Hardness is a property which involves elastic and plastic deformation as well as crack initiation and propagation. Both 2H and 4H SiC show anisotropy in their degree of hardness [1].

Chemical Properties

The covalent bonding of SiC makes it very stable, but thermal decomposition occurs at a temperature of 2818 K. SiC reacts with oxygen to form SiO_2 at high oxygen partial pressure and temperature. The oxidation kinetics depends on the type and size of the SiC form (for example sintered or powder), atmosphere, temperature, and oxygen partial pressure. Significant reaction occurs at temperatures greater than 1673 K [1].

Thermal conductivity

The thermal conductivity K of covalent carbides is directly proportional to thermal diffusivity α_d, density ρ, and specific heat capacity C_p [1] i.e.

$$K = \alpha_d C_p \rho$$ (2.3)

The high thermal conductivity of SiC means that heat generated in the device is quickly transported away. Due to this property SiC-based devices will not need a robust cooling system thereby saving power and reducing the cost of manufacturing electronic products. This also helps in miniaturising the devices.

2.4 Applications of SiC Materials

Due to its good physical, electrical and chemical properties as described above,   SiC has applications in high frequency and high power electronic devices which can operate at extremely high temperature and radiation-intensive environments [6]. SiC-based sensors and electronic devices can, therefore, be deployed in nuclear reactors, automotive engines and space applications. SiC has also been emerging as a promising material for light emitting diodes (LED) after the discovery by S. Kamiyama that nitrogen (N) and boron (B) co-doped SiC has a very high donor-acceptor pair (DAP) emission efficiency [7]. At the moment, most LEDs are made from gallium nitride (GaN) and phosphors, and SiC is used as a substrate material. The problem with phosphors is that they have a short life time and contain rare earths which makes them very expensive. On the other hand, SiC-based LEDs have a high conversion efficiency and produce a better quality light when compared with GaN-based LEDs [8]. In addition, the LEDs have a simpler thermal management because of the high thermal conductivity of SiC. Room temperature generation of a single photon with high efficiency and telecom wavelength has been demonstrated in a pn junction SiC, and this has huge positive implications in quantum computing and information processing [9].

Apart from electronic applications, SiC is also used as a fission products diffusion containment layer in TRISO coated fuel particles in nuclear reactors. The TRISO coated fuel particles are made of three layers of pyrolytic carbon and one layer of SiC. These coatings/layers are fundamental to the safety of the nuclear reactor due to the fact that they are responsible for the confinement of fission products inside the fuel particle. SiC provides the mechanical strength to the fuel particle and is the main diffusion barrier to the release of fission products [10]. In materials technology, SiC is used as a ceramic in high temperature structural applications such as heat exchangers, advanced gas turbine engines, and internal combustion engines [11].

2.5 Properties of ruthenium.

Ruthenium has a high melting point (2250° C), high chemical stability, low electrical resistance, high mechanical resistance to abrasion and fatigue [6]. These properties make ruthenium a good candidate as a Schottky contact for high temperature operating Schottky barrier diodes (SBDs).

2.6 Properties of nickel.

Nickel is the most common metal used for ohmic contacts. Nickel deposited on SiC after rapid thermal annealing (RTA) at high temperature, for example at 950° C, reacts with SiC to form nickel silicide which has a very low contact resistance [12].

2.7 Metal-Semiconductor Junctions.

2.7.1 Introduction

Semiconductor devices have to communicate with other devices through a metal contact, and this contact is done through a non-rectifying metal-semiconductor junction called an ohmic contact. An ohmic contact is a low resistance junction which conducts current in both directions [13]. If the metal-semiconductor junction is rectifying then it is called a Schottky contact.

2.7.2 Schottky Junction

2.7.2.1 Qualitative analysis

Fig 2.4 (a) is an energy band diagram of an isolated metal and n-type semiconductor and Fig 2.4 (b) is an energy band diagram of a metal-semiconductor contact in thermal equilibrium [14].The metal and semiconductor work-functions are $q\phi_m$ and $q\phi_s$ respectively where q represents the charge on an electron. Work-function is the energy difference between the Fermi and vacuum levels. The energy difference between the conduction band edge and the vacuum level in a semiconductor is called electron affinity and is given by $q\chi$. For an intimate contact between the metal and semiconductor at thermal equilibrium, the Fermi level in the two materials will be equal. The ideal barrier height for metal and n-type semiconductor contact is given by

$$q\phi_{Bn} = q\phi_m - q\chi \qquad\qquad (2.4)$$

The ideal barrier height for metal and p-type semiconductor contact is given by

$$q\phi_{Bp} = E_g - (q\phi_m - q\chi) \qquad\qquad (2.5)$$

where E_g is the band gap energy of the semiconductor.

From the two equations, we can see that the sum of the barrier heights on n-type and p-type semiconductor substrates should be equal to the band gap of the semiconductor.
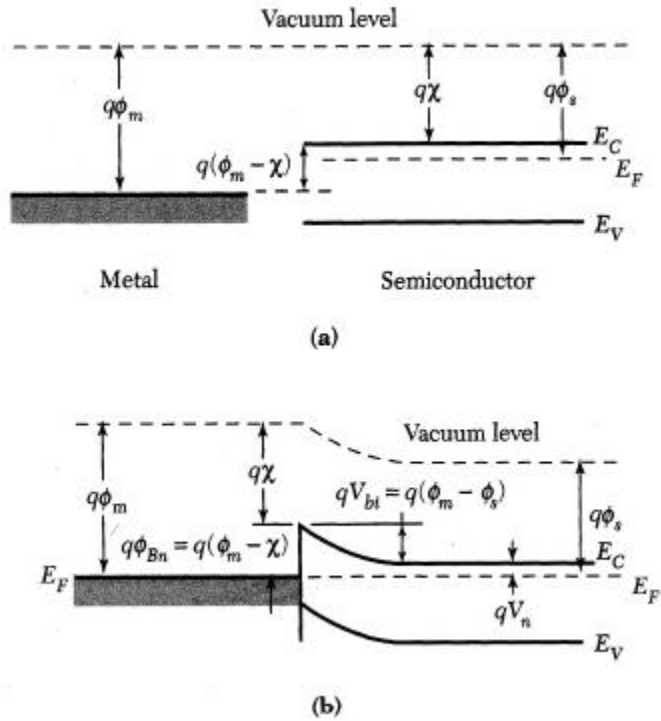
Fig.2.4 Energy band diagram of an isolated metal adjacent to an isolated n-type semiconductor under thermal nonequilibrium condition. (b) Energy band diagram of a metal-semiconductor contact in thermal equilibrium [14].

The built-in potential is the potential seen by electrons in the conduction band which would like to move to the metal and is given by

$$V_{bi} = \phi_{Bn} - V_n \qquad\qquad (2.6)$$

where qV_n is the energy difference between the conduction band and Fermi level [14].

Equations 2.4 and 2.6 are technically called the Schottky-Mott limit for an ideal metal-semiconductor contact.

The size of the Schottky barrier height (SBH) which is usually denoted by Φ_B will determine whether the contact becomes ohmic or Schottky. A low SBH will lead to an ohmic contact and a large value of SBH will create a good Schottky contact.

In condensed form, the Schottky-Mott limit theorem is given by

$$\Phi_B = \Phi_M - \chi_S \qquad (2.7)$$

where Φ_M and χ_S are the metal work function and semiconductor electron affinity respectively. From this equation, we can see that the choice of the metal will determine the SBH. This does not happen in practice. This led to a theory by Bardeen that argued that SBH depends on the density of surface states [15]. In practical Schottky diodes, the disruption of the crystal lattice at the semiconductor surface produces a large number of surface energy states which are located in the forbidden bandgap. The surface states may be dangling bonds at the surface or other types of defects. The relative constancy of the barrier height with metals of various work functions is sometimes attributed to Fermi level pinning, where the Fermi level in the semiconductor is pinned at some energy in the band gap to create a depletion-type contact [16]. Bardeen found out that if the density of surface states is so high, they predetermine the barrier height such that it (the barrier height) is completely independent of the metal work function [15]. These surface states can act as donors or acceptors [14].

2.7.2.2 Current Transport

Thermionic Emission

Majority carriers are mainly responsible for current transport in a Schottky junction. For SBDs operated around room temperature, the thermionic emission is the dominant transport mechanism of majority carriers from the semiconductor into the metal. An electron can be thermionically emitted from the semiconductor surface into the metal if it has an energy which is greater than the barrier height. The number of electrons emitted thermionically [14] is given by

$$n_{th} = N_C \exp(-\frac{q\phi_{Bn}}{kT}) \qquad (2.8)$$

where N_C is the effective density of states in the conduction band, k is the Boltzmann constant and T is the temperature in kelvin. At thermal equilibrium the current flow from metal to the semiconductor is equal to the current flow from semiconductor to metal, and these currents are directly proportional to n_{th}. Mathematically we write

$$\left|J_{s\rightarrow m}\right| = \left|J_{m\rightarrow s}\right| = C_1 N_C \exp(-\frac{q\phi_{Bn}}{kT}) \qquad (2.9)$$

Where $J_{s\rightarrow m}$ and $J_{m\rightarrow s}$ are the current densities from semiconductor to metal and metal to semiconductor respectively, and C_1 is the proportionality constant.

When a forward biasing voltage V_F is applied to the Schottky contact, the potential barrier at the junction is reduced by the amount equal to the applied voltage, and the new electron density at the semiconductor surface becomes

$$n_{th-new} = N_C \exp[-\frac{(q\phi_{Bn-V_F})}{kT}]$$ (2.10)

The current density $J_{s\rightarrow m}$ also increases by the same factor while $J_{m\rightarrow s}$ remains the same due to the fact that ϕ_{Bn} maintains its equilibrium value. The net current density flowing in the forward biasing condition is given by

$$J = J_{s\rightarrow m} - J_{m\rightarrow s} = C_1 N_C \exp[-\frac{(q\phi_{Bn-V_F})}{kT}] - C_1 N_C \exp(-\frac{q\phi_{Bn}}{kT})$$

$$= C_1 N_C \exp\left(-\frac{q\phi_{Bn}}{kT}\right)\left[\exp\left(\frac{qV_F}{kT}\right)-1\right]$$ (2.11)

Under the reverse-biasing condition, V_F is replaced by $-V_R$ in equation 2.11. The coefficient $C_1 N_C$ is equal to $A^* T^2$ where T is the temperature in Kelvin and A^* is called the Richardson constant.

In condensed form the thermionic emission condition for a metal-semiconductor junction is given by

$$J = J_s \left[\exp\left(\frac{qV}{kT}\right)-1\right]$$ (2.12)

$$J_s = A^* T^2 \exp(-\frac{q\phi_{Bn}}{kT})$$ (2.13)

where V can be forward-biasing voltage or reverse biasing voltage, and J_s is the saturation current density. The saturation current depends on SBH and temperature. Equation 2.12 assumes that the ideality factor η is a unity which is the case for an ideal diode. If this is not the case the equation becomes

$$J = J_s \left[\exp\left(\frac{qV}{\eta kT}\right)-1\right]$$ (2.14)

Diffusion and quantum tunneling process

Diffusion is current transport which happens when charge carriers move from a place of high concentration to a place of low concentration. This takes place when there is a spatial variation of charge carrier concentration in the semiconductor material.

In the situation where an electron has less energy than the barrier height but is able to transport itself across the barrier, the process is called quantum tunneling phenomenon [14].

2.7.3 Series Resistance

Series resistance R_S is the resistance of the bulk material of the semiconductor plus that of the back ohmic contact. To account for the series resistance, equation 2.14 is modified to the following equation [17];

$$J = J_s[\exp\left(\frac{q(V-IR_S)}{\eta kT}\right)-1]$$
(2.15)

where I is the current flowing in the diode.

From equation 2.15 the diode forward voltage drop V_F [18] can be derived to give

$$V_F = \frac{kT}{q}\ln(\frac{J_F}{J_S})+R_{on,sp}J_F$$
(2.16)

Where $R_{on,sp}$ is the specific on-resistance of the diode and is basically the total resistance for an area of 1 cm^2. The drift region, the substrate and any contact resistances make up the specific on-resistance.

2.7.4 The Ohmic contact

An ohmic contact is generally defined as a metal-semiconductor contact which has a negligible resistance when compared to the series resistance of the of the bulk material of the semiconductor. The specific contact resistance R_C is defined as

$$R_C = \left(\frac{\partial J}{\partial V}\right)^{-1}_{V=0}$$ (2.17)

The thermionic emission dominates the current transport for metal-semiconductor contacts with low doping concentrations, and we can obtain R_C from equation 2.15.

$$R_C = \frac{k}{qA^*T} \exp\left(\frac{q\phi_{Bn}}{kT}\right)$$ (2.18)

2.7.5 Junction capacitance

Fig 2.4 depicts the charge and field distribution of a metal-semiconductor junction [14].
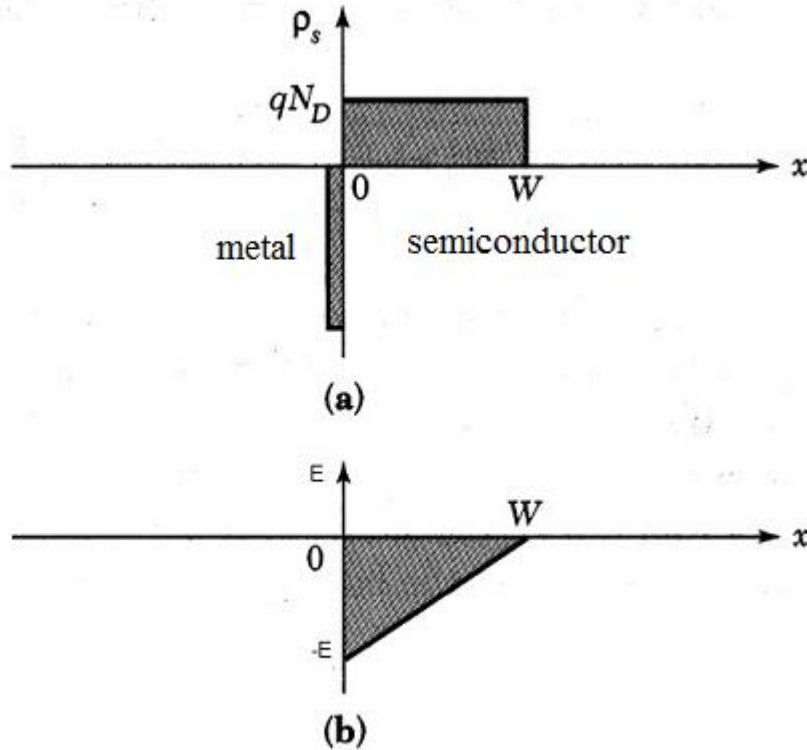
Fig 2.5 (a) Charge distribution and (b) electric-field distribution in a metal semiconductor contact [14].

The metal and the semiconductor form an abrupt junction. The space charge region has a width of W. The charge density in the depletion region is given by

$$\rho_s = qN_D, \quad x < W$$
$$= 0, \quad\quad x > W \tag{2.19}$$

where N_D is the donor doping density. The electric field is maximum at the interface and decreases linearly with distance x. The electric field is given by

$$|E(x)| = \frac{qN_D}{\varepsilon_s}(W - x) = E_m - \frac{qN_D x}{\varepsilon_s} \tag{2.20}$$

$$E_m = \frac{qN_D W}{\varepsilon_s} \tag{2.21}$$

where ε_s is the dielectric permittivity of the conductor. The voltage across the space charge region (depletion layer) is given by the area under the field curve in Fig 2.4(b).

$$V_{bi} - V = \frac{E_m W}{2} = \frac{qN_D W^2}{2\varepsilon_s} \tag{2.22}$$

$$W = \sqrt{\frac{2\varepsilon_s(V_{bi} - V)}{qN_D}} \tag{2.23}$$

In the semiconductor, the space charge density is given by

$$Q_{SC} = qN_D W = \sqrt{2q\varepsilon_s N_D(V_{bi} - V)} \tag{2.24}$$

The junction capacitance per unit area is equal to a partial differentiation of Q_{SC} with respect to voltage V.

$$C = \left| \frac{\partial Q_{SC}}{\partial V} \right| = \sqrt{\frac{q\varepsilon_s N_D}{2(V_{bi} - V)}} = \frac{\varepsilon_s}{W} \tag{2.25}$$

$$\frac{1}{C^2} = \frac{2(V_{bi} - V)}{q\varepsilon_s N_D} \tag{2.26}$$

A plot of $\frac{1}{C^2}$ versus V will give a straight line, and a donor doping density N_D can be extracted from the graph. The Schottky barrier height (SBH) is determined from the voltage intercept by the following equation

$$\phi_{Bn} = V_{bi} + V_o \tag{2.27}$$

Where V_{bi} is the voltage intercept, and

$$V_o = \frac{kT}{q} \ln\left(\frac{N_C}{N_D}\right) \tag{2.28}$$

where N_C is the effective density of states in the conduction band of 6H-SiC or 4H-SiC. N_C is equal to $8.9 \times 10^{19} \text{cm}^{-3}$ for 6H-SiC and $1.7 \times 10^{19} \text{cm}^{-3}$ for 4H-SiC at 300K [19].

2.8 Interaction and diffusion of metals in SiC

Due to the fact that SiC is used a layer in TRISO coated fuel particles, and that nuclear fission reaction of uranium and plutonium oxide fuels releases high yields of metals such as ruthenium, rhodium, palladium, molybdenum, technicium, and silver [20,21], it is important to study these metals' interaction and their diffusion mechanism with SiC. Diffusion, which is defined as the movement of atoms from a higher concentration to a lower concentration, is regarded as the main mechanism of mobility of metals in SiC [22,23]. Diffusion is governed by the following equation [21].

$$\frac{\partial C}{\partial t} = D\nabla^2 C \tag{2.29}$$

where C is particle concentration and D is the diffusion coefficient.
The diffusion coefficient D obeys an Arrhenius equation which is given by

$$D = D_o \exp(\frac{-E_a}{RT}) \tag{2.30}$$

where R is the gas constant, E_a is the activation energy, T is the absolute temperature and D_o is a pre-exponential factor.

Gentile *et al* [24] in their study of the interaction of palladium with 3C-SiC and H-SiC at different temperatures in an argon environment found that palladium reacted with SiC to form silicides with stoichiometry Pd_2Si and Pd_3Si at temperatures of 774 K and above. Graphite was also observed to form on the surface at a temperature of 1723 K. Neethling *et al* [22] investigated the transport of palladium with silver in polycrystalline 3C-SiC grown on Si (0 0 1) and 6H-SiC single crystalline wafers by annealing a palladium-silver compound in contact with SiC in an argon environment. They found that palladium reacted with SiC at 1000 °C to form Pd_2Si. They also observed that both the palladium and silver penetrated the SiC layer to a depth of 400-600 nm. They suggested that silver transport in SiC took place in the form of moving nodules consisting of a silver-palladium mixture and that these nodules moved along grain boundaries by dissolving the SiC at the leading edge followed by the reprecipitation of SiC at the trailing edge.

The literature for the interaction of silver, palladium and caesium with SiC is vast [25-33] but very few have dealt with the interaction of Ru with SiC (see chapter 1). Therefore to shed more light on Ru/SiC interaction, part of this research study investigated Ru interaction with 4H-SiC and 6H-SiC in three annealing environments namely air, argon, and vacuum. The microstructure characterization part of the research basically investigated phase transformation and diffusion at the Ru-SiC interface after annealing in the three different environments mentioned above. The information obtained from this part of the investigation sheds more light on the effectiveness of SiC as a containment layer in TRISO coated fuel particles.

2.9 TRISO Coated fuel particles

The TRISO coating technique is the most common technology for fabricating fuels for high temperature gas reactors (HTGR). The coated fuel particle is a microsphere with a diameter of about 1 mm with five distinct regions. At the centre of the particle (Fig. 1) is the fuel kernel which is usually an oxide, carbide or oxycarbide of uranium, plutonium, thorium or transuranic elements [34]. The fuel kernel is surrounded by a porous carbon buffer whose functions are to attenuate recoiling fission fragments, accommodate internal gas buildup and particle dimensional changes. The outer layers are made up of an inner pyrolytic carbon (IpyC) layer, SiC layer, and an outer pyrolytic (OpyC) layer. The SiC layer acts as the main pressure vessel of the particle and is supposed to withstand internal gas buildup stresses, and

provide a diffusion barrier to gaseous and metallic fission products. The PyC layers protect the SiC from chemical attack and also act as diffusion barriers to fission products. A TRISO particle is considered to have failed when the structural layers surrounding the fuel kernel are damaged or breached thereby allowing the release of fission products. The main causes of TRISO particle failures are overpressurisation, fission product attack and the amoeba effect [35]. Amoeba effect also called kernel migration happens when the temperature gradient across the fuel compact becomes very high due to extreme operating conditions leading to the removal of carbon from the "hot" side and deposition of carbon on the "cold" side of the IpyC layer resulting in a visual impression of fuel kernel migration towards the "hot" side [36].

2.10 Atomic collision theory and RBS

RBS is based on the classical scattering in a central-force field. Apart from the accelerator which provides a collimated beam of MeV particles, the RBS apparatus has semiconductor nuclear particle detectors that give an output voltage pulse proportional to the energy of the particles scattered from the sample into the detector [37]. The kinematics of the collision and the scattering cross section are independent of chemical bonding, therefore, RBS measurements are insensitive to electronic configuration or chemical bonding of the target. Monoenergetic particles in the incident beam collide with target atoms and are scattered backwards into the detector-analysis system (Fig 2.6 a) where the energies of the particles are measured. During collision energy is transferred from the moving incident particle to the stationary target atom, and the reduction in energy of the scattered particle depends on the masses of incident and target atoms and provides the signature of the target atoms [37].
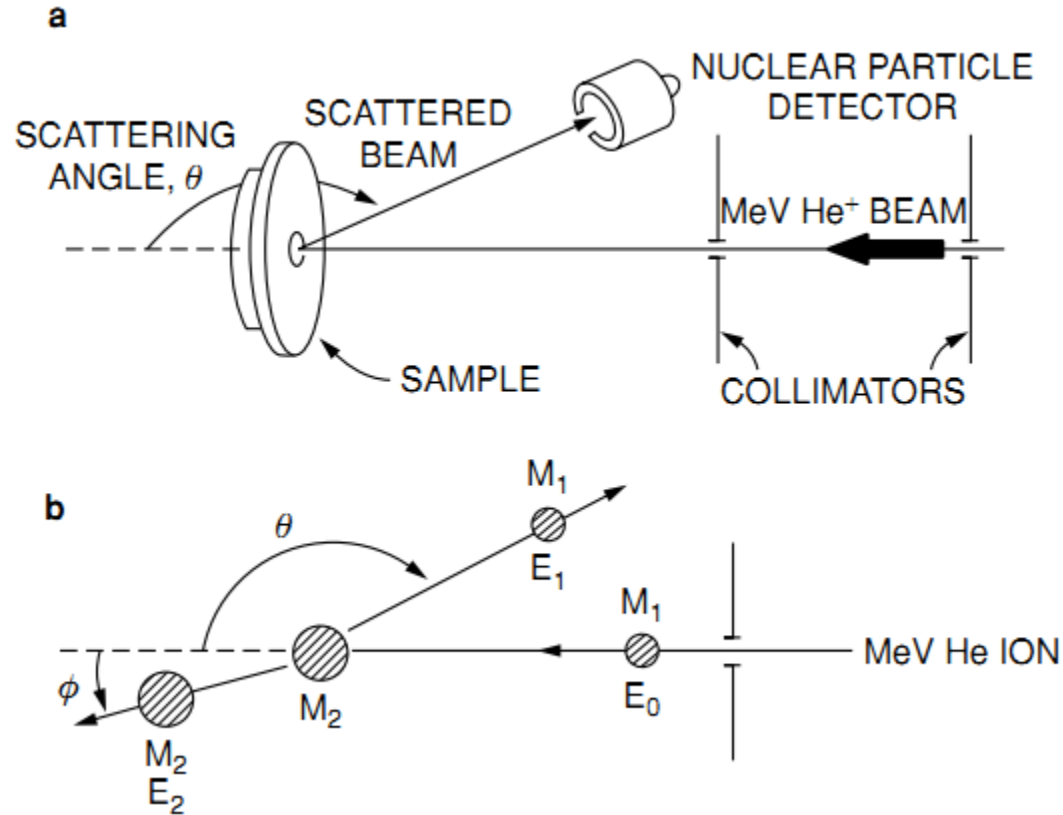
Fig 2.6 Nuclear particle detector and the scattering angle [37].

The principles of conservation of energy and momentum are used to describe the energy transfer and kinematics of the elastic collision of the particles. The collision geometry and notation is given in Fig 2.6 b where θ and ϕ are called the scattering and recoil angles respectively. M_1 and M_2 are the incident and target particles respectively.

Using conservation of energy and momentum give the following equations;

$$\frac{1}{2}M_1 v^2 = \frac{1}{2}M_1 v_1^2 + \frac{1}{2}M_2 v_2^2, \qquad (2.31)$$

$$M_1 v = M_1 v_1 \cos\theta + M_2 v_2 \cos\phi, \qquad (2.32)$$

$$0 = M_1 v_1 \sin\theta - M_2 v_2 \sin\phi. \qquad (2.33)$$

Solving these equations gives the ratio of particle velocities as

$$\frac{v_1}{v} = \left[\frac{\pm(M_2^2 - M_1^2 \sin^2\theta)^{1/2} + M_1 \cos\theta}{M_2 + M_1} \right]. \qquad (2.34)$$

The ratio of the projectile energies for $M_1 < M_2$ is given by

$$\frac{E_1}{E_0} = \left[\frac{(M_2^2 - M_1^2 \sin^2\theta)^{1/2} + M_1 \cos\theta}{M_2 + M_1} \right]^2. \qquad (2.35)$$

The energy ratio which is called the kinematic factor $K = E_1/E_0$, shows that the energy
after scattering depends only on the masses of the particle and target atom and the scattering angle. The lowest value of energy ratio is obtained through a backscattering angle of 180° and is given by

$$\frac{E_1}{E_0} = \left(\frac{M_2 - M_1}{M_2 + M_1} \right)^2 \qquad (2.36)$$

The energy ratio at scattering angle of 90° is given by

$$\frac{E_1}{E_0} = \frac{M_2 - M_1}{M_2 + M_1}. \tag{2.37}$$

The maximum value of energy E_2 is transferred to the target atom at the backscattering angle of 180 and its expression is given by the following equation;

$$\frac{E_2}{E_0} = \frac{4M_1 M_2}{(M_1 + M_2)^2}, \tag{2.38}$$

This equation is generalised to the following expression;

$$\frac{E_2}{E_0} = \frac{4M_1 M_2}{(M_1 + M_2)^2} \cos^2 \phi. \tag{2.39}$$

 Most RBS apparatuses use a surface-barrier solid-state nuclear-particle detector for measurement of the energy spectrum of the backscattered particles where the nuclear particle detector operates by the collection of the hole-electron pairs created by the incident particle in the depletion region of the reverse-biased Schottky barrier diode. The signals from the semiconductor detector electronic system are in the form of voltage pulses where the heights of the pulses are proportional to the incident energy of the particles. The pulse height analyzer stores pulses of a given height in a given voltage bin or channel (multichannel analyzer). The channel numbers are calibrated in terms of the pulse height, hence, there is a direct relationship between channel number and energy for the RBS spectrum [37]. RBS has applications in the analysis of thin films where their composition can be determined. RBS can provide depth distribution without the requirement of the destruction of the sample [38].

2.11 Reference

[1] L.L. Snead, T.Nozawa Y.Katoh, T. Byun , S. Kondo, D.A. Petti, *Handbook of SiC properties for fuel performance modeling,* Journal of Nuclear Materials 371 329–377, (2007).

[2] H. Lee, Fabrication and Characterisation of Silicon Carbide Power Bipolar Junction Transistors, Ph.D. Thesis, KTH, Royal Institute of Technology, (2008).

[3] S.Lee, Processing and Characterization of Silicon Carbide (6H- and 4H-SiC) Contacts for High Power and High Temperature Device Applications, Ph.D. Thesis, KTH, Royal Institute of Technology, (2002).

[4] D. Perronne, Process and characterisation techniques on 4H - Silicon Carbide. Ph.D. Thesis, Politecnico di Torino, (2007).

[5] B. Ozpineci, L. M. Tolbert, Comparison of wide-band semiconductor for power applications, United States Department of Energy (2003)

[6] L. Stuchlikova, D. Buc, L. Harmatha, U. Helmersson, W. H. Chang, I. Bello, *Deep energy levels in RuO$_2$/4H–SiC Schottky barrier structures*, Applied Physics Letters 88, 153509, (2006).

[7] H. Ou, Y. Ou , A. Argyraki, S. Schimmel, M. Kaiser, P. Wellmann, M.K. Linnarsson, V. Jokubavicius, J. Sun, R. Liljedahl, M. Syvajarvi, *Advances in wide bandgap SiC for optoelectronics*, The European Physical Journal B, 87:58, (2014).

[8] M. Syväjärvi, J. Müller, J.W. Sun, V. Grivickas, Y. Ou, V. Jokubavicius, M. Kaisr, K. Ariyawong, K. Gulbinas, P. Hens, R. Liljedahl, M. K. Linnarsson, S. Kamiyama, P. Wellmann, E. Spiecker, H. Ou, *Fluorescent SiC as a new material for white LEDs*, Physica Scripta, T148, 014002, (2012).

[9] F. Fuchs, V. A. Soltamov, S.Vath, P. G. Baranov, E. N. Mokhov, G. V. Astakhov,   V. Dyakonov, *Silicon carbide light-emitting diode as a prospective room temperature source for single photons*, Scientific Reports, 3, 1637, (2013).

[10] E. Lopez-Honorato, J. Tan, P.J. Meadows, G. Marsh, P. Xiao, TRISO coated fuel particles with enhanced SiC properties, Journal of Nuclear Materials 392, 219-224, (2009).

[11] P. Demkowicz, K. Wright, J. Gan, D. Petti, *High temperature interface reactions of TiC, TiN, and SiC with palladium and rhodium*, Solid State Ionics 179, 2313-2321, (2008).

 [12] A. Kakanakova-Georgieva, Ts. Marinova, O. Noblancb, C. Arnodob, S. Cassetteb,   C. Brylinskib, *Characterization of ohmic and Schottky contacts on SiC*, Thin Solid Films 343-344, 637-641, (1999).

[13] D. Neamen, Semiconductor Physics and Devices, McGraw-Hill, New York, (2003).

[14] S.M Sze, Semiconductor Devices Physics Technology, John Wiley & Sons, New York, (2002).

[15] L. M Porter, R.F Davis, A *critical review of ohmic and rectifying contacts for SiC*, Material Science and Engineering B34, 83-105, (1995).

[16] D. K. Schroeder, Semiconductor Material and Device Characterisation, John Wiley & Sons, New Jersey, (2006).

[17] V. Aubrey, F. Meyer, *Schottky diodes with high series resistance: Limitations of forward I-V methods*, Journal of Applied Physics 76 (12), (1994).

[18] M. Bhatnagar, B.J. Baliga, *Comparison of 6H-SiC, 3C-SiC and Si for power devices*, IEEE Transactions on Electronic Devices, Vol. 40, No. 3 (1993).

[19] http://www.ioffe.rssi.ru/SVA/NSM/Semicond/SiC/bandstr.html, accessed on 25 April 2013.

[20] T.M. Besmann, R.E. Stoller, G. Samolyuk, P.C. Schuck, S.I. Golubov, S.P. Rudin, J.M. Wills, J.D. Coe, B.D. Wirth, S. Kim, D.D. Morgan, I. Szlufarska, *Modeling Deep Burn TRISO particle nuclear fuel*, Journal of Nuclear Materials 430 181-189, (2012).

[21] X.W. Zhou, C.H. Chang, *Current status and future development of coated fuel particles for high temperature gas-cooled reactors*, Progress in Nuclear Energy 53 182-188,(2011).

[22] J.H. Neethling, J.H. O'Connell, E.J. Olivier, *Palladium assisted silver transport in polycrystalline SiC*, Nuclear Engineering and Design 251, 230–234, (2012).

[23]T.T. Hlatshwayo, Diffusion of silver in 6H-SiC, Ph.D. Thesis, University of Pretoria, (2010).

[24] M. Gentile, P. Xiao, T. Abram, *Palladium interaction with silicon carbide*, Journal of Nuclear Materials, 462, 100–107, (2015).

[25] D. Shrader, S.M. Khalil, T. Gerczak, T. R. Allen, A. J. Heimc, I. Szlufarska, D. Morgan, *Ag diffusion in cubic silicon carbide*, Journal of Nuclear Materials, 408 257–271, (2011).

[26] K. Minato, K. Fukuda, A. Ishikawa, N. Mita, *Advanced coatings for HTGR fuel particles against corrosion of layer*, Journal of Nuclear Materials 246 215-222, (1997).

[27] P. Demkowicz, K. Wright, J. Gan, D. Petti, *High temperature interface reactions of TiC, TiN, and SiC with palladium and rhodium*, Solid State Ionics 179, 2313–2321,(2008).

[28] J. Rabone, E. López-Honorato, *Density functional theory metadynamics of silver, caesium and palladium diffusion at 3C-SiC grain boundaries*, Journal of Nuclear Materials, 458 56–63, (2015).

[29] I. J. van Rooyen, T. M. Lillo, Y. Q. Wu, *Identification of Silver and Palladium in Irradiated*, TRISO Coated Particles of the AGR-1 Experiment, Journal of Nuclear Materials, DOI:10.1016/j.jnucmat.2013.11.028, (2014).

[30] E. Lopez-Honorato, D. Yang, J. Tan, P.J. Meadows, P. Xiao, *Silver Diffusion in Coated Fuel Particles*, Journal of American Ceramic Society, 93, [10], 3076–3079, (2010).

[31] J.H. O'Connell, J.H. Neethling, *Ag transport in high temperature neutron irradiated 3C–SiC*, Journal of Nuclear Materials, 445, 20–25, (2014).

[32] A. Londono-Hurtado, A. J. Heim, S. Kim, I. Szlufarska, D. Morgan, *Cs and Ag co-incorporation in cubic silicon carbide*, Journal of Nuclear Materials 439, 65–71, (2013).

[33] T.M. Lillo, I.J. van Rooyen, *Associations of Pd, U and Ag in the SiC layer of neutron-irradiated TRISO fuel*, Journal of Nuclear Materials 460, 97–106, (2015).

[34] J.J. Powers, B.D. Wirth, *A review of TRISO fuel performance models*, Journal of Nuclear Materials 405, 74-82, (2010).

[35] I.E. Porter, T.W. Knight, M.C. Dulude, E. Roberts, J. Hobbs, *Design and fabrication of an advanced TRISO fuel with ZrC coating*, Nuclear Engineering and Design 259, 180-186, (2013).

[36] X.W. Zhou, C.H. Chang, *Current status and future development of coated fuel particles for high temperature gas-cooled reactors*, Progress in Nuclear Energy 53 182-188, (2011).

[37] T.L. Alford, L.C. Feldman, J.W. Mayer, Fundamentals of Nanoscale analysis, Springer, (2007).

[38] W. K. Chu, J. W. Mayer, and M.A. Nicolet, Backscattering Spectrometry, Academic Press, New York, (1978).

CHAPTER 3

EXPERIMENTAL TECHNIQUES

3.1 Introduction

This chapter describes the equipment and analytical tools used in the study. Section 3.2 explains sample preparation techniques while section 3.3 outlines the annealing process of Schottky diodes and thin films of both SiC polytypes used in this study. Section 3.4 describes the electrical characterisation techniques, whereas section 3.5 outlines the microstructure characterisation tools and techniques used in this

research. It should be mentioned at the outset that the main tool that was used for thin film characterisation was RBS. This was due to the fact that this tool was readily available to the researcher. The other tools such as scanning electron microscopy, x-ray diffraction technique, and Raman spectroscopy were not readily available to the researcher, and therefore, were used for a very small number of samples.

3.2 Sample preparation techniques

The preparation of metal-SiC interfaces has a critical effect on the physical, chemical and electrical behaviour of the contact, and also on its reliability. Experiments have shown that the electrical performances of Schottky contacts or films on SiC, as well as their physical and chemical properties, are strongly dependent on the quality of the metal–semiconductor interface and, hence, on the surface preparation prior to metallization [1]. For example, surface roughness, interfacial contaminants, and residual thin oxide layers have been shown to be major culprits in the non-ideal current–voltage characteristics, high leakage current and high device on-resistance in SiC diodes.

3.2.1 Preparation of SiC and deposition of the metal contacts for Schottky diodes fabrication

Both n-type bulk-grown 6H-SiC and n-type 4H-SiC with an epilayer obtained from Cree Research Inc. were used in the fabrication of Schottky barrier diodes.

The n-type 6H-SiC, as well as n-type 4H-SiC with an epilayer, were prepared for metallization by degreasing, using an ultra-sonic bath for a period of 5 minutes for each step, in trichloroethylene, acetone and methanol, followed by rinsing in deionised water after each stage of chemical cleaning. The samples were then deoxidized in 10% HF. The samples were finally rinsed with deionised water and then dried with nitrogen before loading them into the vacuum chamber where 100 nm of nickel (Ni) was deposited by resistive evaporation in a vacuum of 10^{-6} mbar pressure. The samples were then annealed in an argon atmosphere at a temperature of 950°C for 1 minute to make the contact ohmic. The annealed samples were then chemically cleaned again in trichloroethylene, acetone, and methanol, and deionised water before a 50 nm thick of ruthenium was deposited by e-beam through a metal contact mask at 10^{-6} bar pressure. The ruthenium film thickness was monitored by the Infincon meter until the required thickness was obtained. Dots of Schottky contacts of diameter 0.6mm were fabricated.

3.2.2 Preparation of samples for microstructure characterisation

Samples of n-type 6H-SiC (as well as n-type 4H-SiC with epilayer) for microstructure characterisation were cleaned as in 3.2.1, before depositing by e-beam a thin film of 50 nm of ruthenium on the smooth surface of the sample at 10^{-6} mbar pressure.

3.2.3 Thin film, Schottky and ohmic contact fabrication

Nickel ohmic contacts were deposited on the unpolished side of both 6H-SiC and 4H-SiC by the resistive evaporation technique. A schematic of the vacuum resistive evaporation deposition system [2] is shown in Fig 3.1. The chamber is evacuated to a pressure of 10^{-6} mbar before nickel is deposited on the sample. Nickel is placed in the metal crucible where current is passed through, which makes the nickel to evaporate and deposit on the substrate (4H-SiC or 6H-SiC) placed above it.
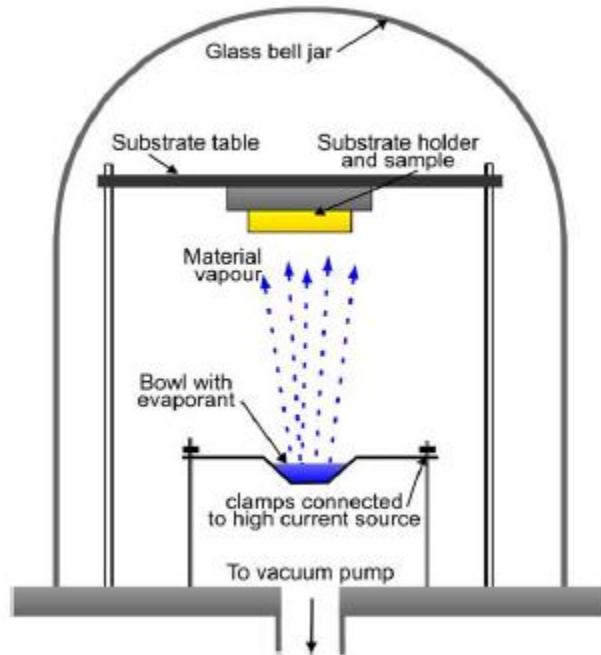

Fig 3.1 Schematic of vacuum resistive evaporation system [2].

The ruthenium Schottky contacts were deposited on the polished side of both 4H-SiC and 6H-SiC by an electron-beam deposition technique. The e-beam deposition system [3] is shown in Fig 3.2. The chamber was evacuated to a pressure of less than 10^{-6} mbar before the start of the deposition process. In the e-beam system, a hot filament emits electrons which are then focussed on the target material by magnetic and electric fields. In this investigation, the target material was ruthenium in a carbon crucible.
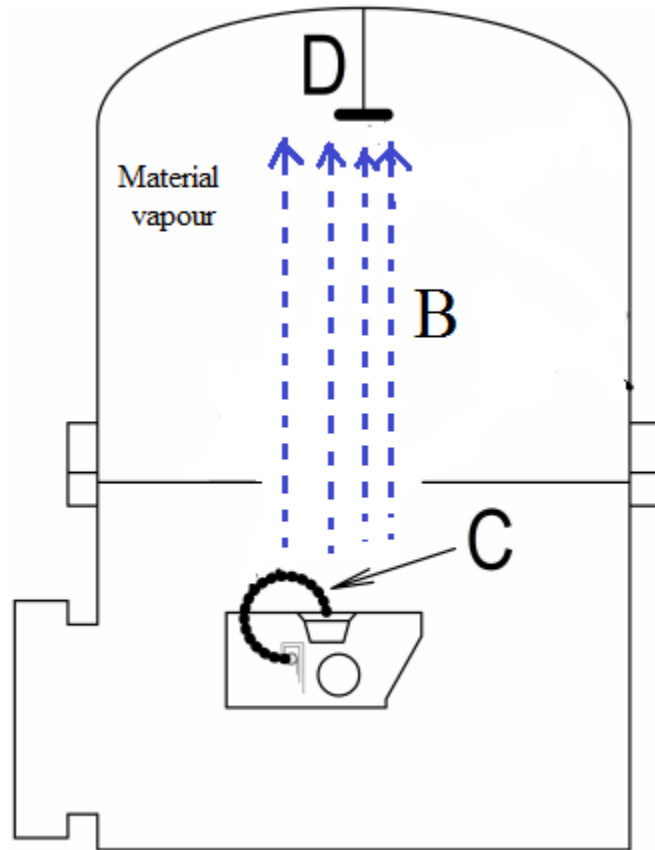
Fig 3.2 Schematic of electron-beam evaporation system showing electron beam path (C), evaporant motion (B) and the SiC wafer positioned at the top of the chamber (D) [3].

The impact of the electrons on the ruthenium sample made it evaporate and get deposited on the sample substrate(4H-SiC or 6H-SiC) placed above the carbon crucible. A metal contact mask was placed on 4H-SiC and 6H-SiC samples so as to fabricate Schottky dots of diameter 6 mm.

The process of deposition of ruthenium thin films was the same as the one immediately described above except that metal contact mask with holes was not used.

3.3 Annealing process

Samples of Ru/SiC (both 6H-SiC and 4H-SiC) thin films and Schottky diodes were annealed in argon, and air ambient in a Lindberg hevi-duty furnace for a period of 15 minutes at temperatures ranging from 100 ^{o}C to 1000 ^{o}C. Samples of Ru/SiC thin films and Schottky diodes were also annealed in a vacuum furnace at a pressure of less than 10^{-7} mbar for 1 hour at temperatures ranging from 500 ^{o}C to 1000 ^{o}C. The maximum limit of the annealing temperature in the vacuum furnace was 1000 ^{o}C.

3.4 Current-voltage (IV) and Capacitance-voltage (CV) characterisation

Full IV and CV characterisation of the diodes was performed at an ambient temperature of 24 ^{0}C after each annealing process using 4140B pA meter /DC voltage source Hewlett Packard measuring instrument which was interfaced to a LabVIEW operated computer. The CV measurements were done at a frequency of 1MHz. Both the IV and CV measurement data were automatically saved in the computer by LabVIEW. The sample measurements were done in darkness and screened from electrical noise by a metal box.

3.5   Microstructure Characterisation tools

3.5.1 RBS

RBS uses a beam of monoenergetic (usually α, ^{4}He+ and ^{1}He+) particles produced in an accelerator which bombard the sample to be investigated. Some of the projectiles will undergo close collisions with the nuclei of single atoms, and get backscattered. By measuring the energy change of the backscattered projectiles at a certain angle, information on the nature and concentration of the target atoms as well their depth distributions can be obtained [4,5].

As an example, a sample (which has atoms of mass M) is to be analysed by exposing it to a beam of ions with a mass m and with an energy E_o which is usually in the range of MeV. A solid state detector is used to view the backscattered ions at a deflection angle of θ. The backscattered ions create electron-hole pairs in the detector, which are then separated by an applied electric field and a charge pulse is created [5]. The number of electron-hole pairs is proportional to the energy of the backscattered ions. The energy of the backscattered ions [6] is given by

$$E = E_o \left[\frac{\sqrt{1-\left(\dfrac{m}{M}\right)^2 \sin^2\theta} + \left(\dfrac{m}{M}\right)\cos\theta}{1+\left(\dfrac{m}{M}\right)} \right]^2 \qquad (3.1)$$

The ion beam penetrating the sample will lose energy due to its collisions with electrons and nuclei of the sample. The ratio of the energy of the backscattered particle to that of the incident energy is called the kinematic factor K. Thus

$$E = KE_o \qquad (3.2)$$

The energy loss per unit distance is called the stopping power [5,6] of the material.

Stopping power $= \dfrac{\Delta E}{\Delta x}$ $\qquad (3.3)$

where Δx is measured in 10^{15} atoms/cm^2. From equation 3.1, it can be observed that ion beams colliding with a heavy target material will lose less energy than those colliding with a lower atomic mass target material. The stopping power, therefore, depends on the target material and the energy of the incident ion beams. Fig 3.3 (a) depicts a typical example of RBS experiment.
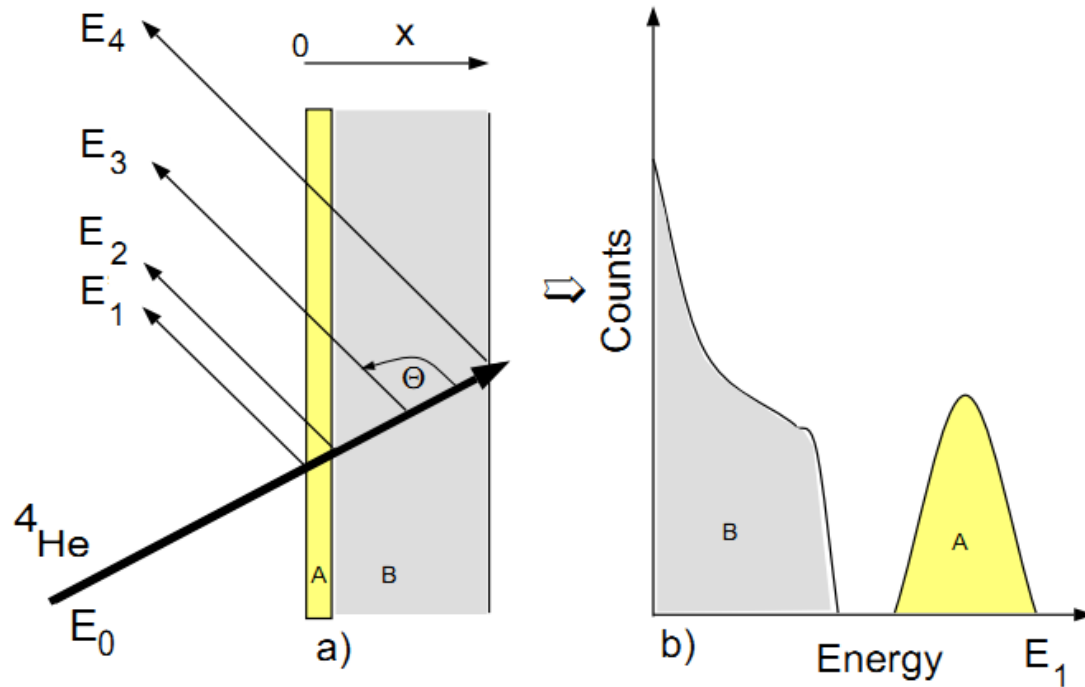
Fig 3.3 (a) Schematic diagram of an RBS experiment, (b) RBS spectrum [6].

A thin top layer A of atoms with a high atomic mass M_A is situated on top of the bulk substrate B with a lower atomic mass M_B. In the energy spectrum of backscattered particles (Fig. 3.3b), the film A gives a spectral peak at higher energies. Scattering of the ions from the B layer produces a broadened step at lower energies. The higher energy side of this step originates from ion beams scattering from the top most part of the B layer [6].

In this study, the helium (^{4}He+) ions of energy 1.4 MeV and 1.6 MeV were used as projectiles for studying the interface reactions between ruthenium and SiC. The schematic of the RBS system attached to a Van de Graaff accelerator [2] that was used in this investigation is shown in Fig 3.3. The charged particles which are produced from the ion source are accelerated by a large potential difference that exists across the accelerator tube. The beam current in this investigation was kept below 14 nA and the target chamber was kept at a pressure below 1×10^{-4} Pa during the measurement process. The backscattered particles in the target chamber are detected by

the silicon surface barrier detector. The output voltage from the detector is proportional to the backscattered energy of the projectiles. The amplified output voltage is converted to a digital signal in the multi-channel analyser (MCA). The MCA basically gives an output of yield (count) vs channel number where yield and channel number are proportional to the number of backscattered particles and backscattered energy respectively of the projectiles [2].

The energy,E, of the detected particle is linearly proportional to the channel number (ch) of the MCA [7]:

$$E = kch * ch + E_0 \qquad\qquad (3.4)$$

where kch (keV/channel) and E_0 (zero offset) are the energy calibration coefficients. These parameters are needed for fitting a theoretical spectrum to the experimental
one (i.e. simulation). Both parameters are needed for the calibration of the analyser. Two channel positions of known energy values (usually the surface edges of known peaks in the RBS spectrum) are sufficient to calculate kch and E_0 by using a linear graph.
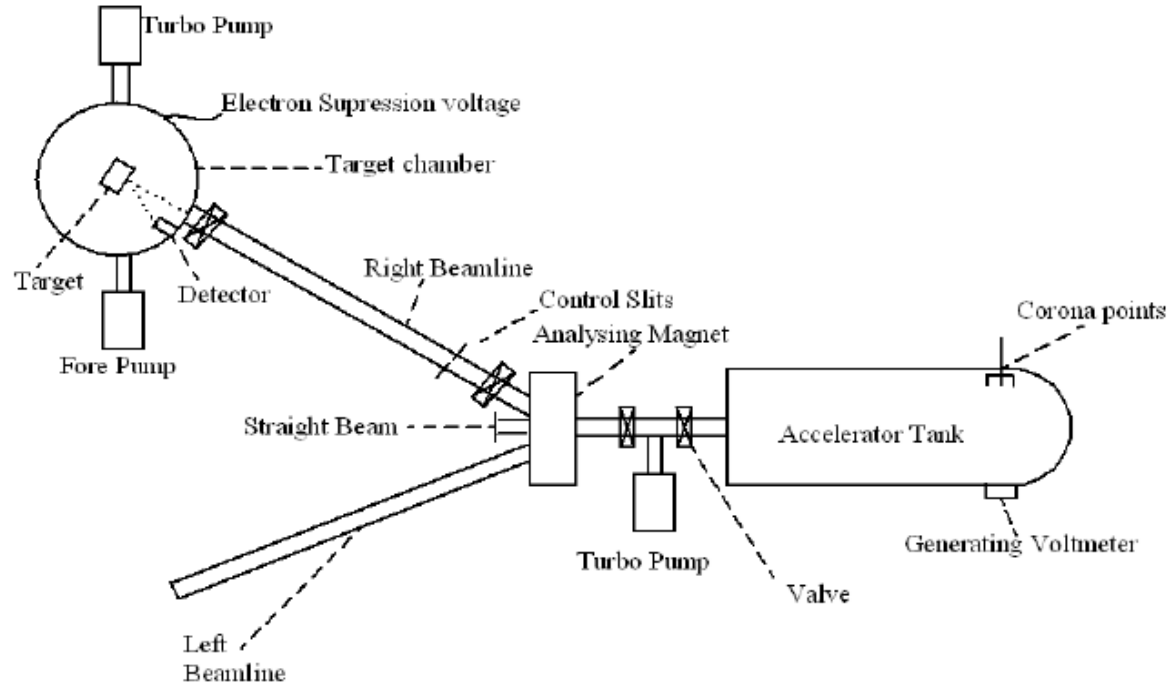
Fig 3.3 RBS system attached to Van de Graaff accelerator [2].

To obtain the concentration depth profile of the sample, a software programme called RUMP [8] is used. The programme generally works as follows. The user first prescribes the depth profiles of all elements and then compares the simulated spectrum with the spectrum of the measured data. The depth profiles are then adjusted through a number of iterative steps until one obtains a reasonable agreement of simulated and measured data. Fitting with RUMP is done through trial and error, and a good model of the sample is usually assumed. The RUMP simulation procedure has several shortcomings. In many cases there is an ambiguity between different depth profiles or compositions which fit the data equally well [6].

3.5.2 Raman Spectroscopy

Raman spectroscopy works on the principle that when light interacts with matter, the photons which make up light may be absorbed or scattered, and when these scattered photons are observed by collecting light at an angle to the incident beam, information on the composition of matter can be obtained [9]. The sample under investigation is irradiated with an intense monochromatic light source usually laser light. The radiation can be scattered by the sample at the same wavelength as that of the incident laser radiation in a process known as Rayleigh scattering. A small fraction of the incident radiation is scattered at a wavelength that is shifted from the original laser wavelength as illustrated in Fig 3.4 [10].

In vibrational physics, a molecule at rest is said to be in the ground vibrational and electronic states. The incident laser beam excites the molecule to higher energy state. The molecule may lose its energy by transitioning to the first vibrational level; in a process called Stokes-Raman shift. Stokes-Raman shift produces light of lower energy and longer wavelength than that of the incident radiation. Some molecules in the system may initially be in the excited vibrational level, and may transition to a ground state during the Raman process. This scattering process is called anti-stokes-Raman scatter and produces light of higher energy and lower wavelength than the incident beam. The schematic of a Fourier Transform (FT)-Raman Spectroscopy system [9] is illustrated in Fig 3.5. FT-Raman uses single-element, near-infrared detectors such as liquid nitrogen-cooled germanium (Ge) detectors. An interferometer converts the Raman signal into an interferogram. A Fourier transform algorithm converts the interferogram into a conventional Raman spectrum. In conventional Raman spectroscopy, the spectrum is usually plotted with intensity on the y-axis and wave number on the x-axis. The intensities of the bands in the Raman spectrum will depend on the nature of the vibrations of the molecules in the sample. The relative intensities of the peaks will give an indication that the correct vibrations of the molecules have been picked out. The position of the peaks is used to identify the molecules or phases that are available in the sample [11].
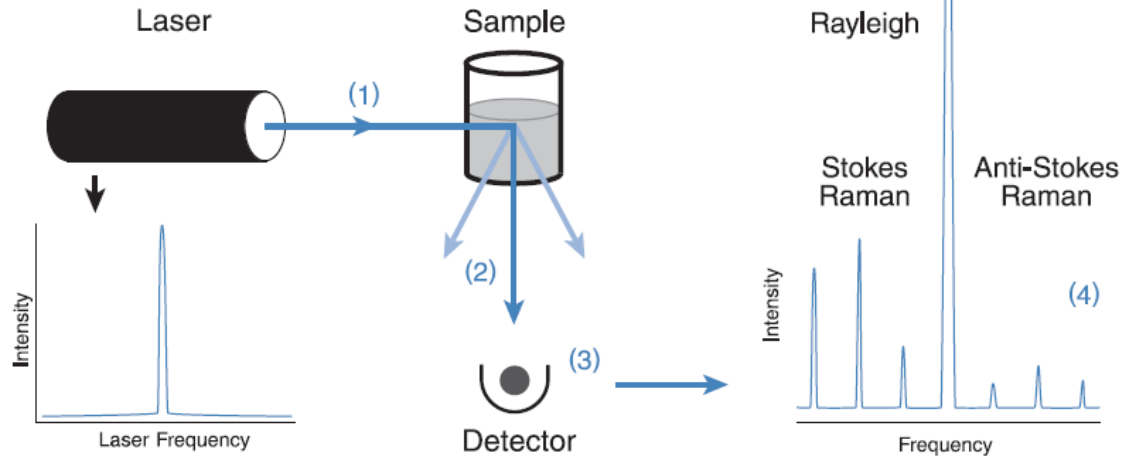
(1) Laser light excites the sample.
(2) This light is scattered in all directions.
(3) Some of this scattered light is directed to the detector, which records the Raman spectrum.
(4) This spectrum shows light at the original laser (or Rayleigh) frequency and the Raman spectral features unique to the sample.

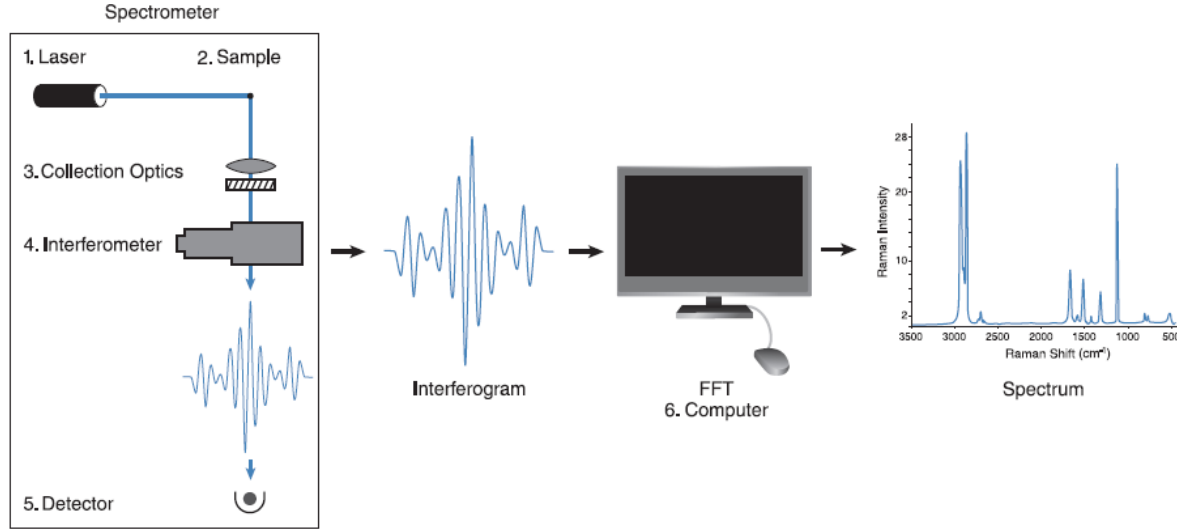Fig 3.4 Raman analysis of a sample [9].

Fig 3.5 Schematic of FT-Raman Spectroscopy System [9].

3.5.3 X-ray diffraction analysis

X-ray diffraction (XRD) analysis works on the principle that when electromagnetic radiation (usually x-rays) impinges on periodic structures with geometrical variations on the length scale of the wavelength of the radiation [12], there is constructive interference at certain angles of incident radiation. The condition for constructive interference is given by Bragg's Law equation.

$$2d \sin \theta = n\lambda \qquad\qquad\qquad (3.5)$$

where d is the plane separation, n is the order of diffraction, θ is the angle of incidence, λ is the wavelength of radiation. The diffraction pattern is strong if the distance between the atoms in the sample is comparable to the wavelength of the x-rays. By observing the radiation that comes out of the sample at certain angles, information on the composition of the sample is obtained.

Detectors are used to observe the diffraction pattern of the x-rays usually at a diffraction angle of 2θ (Fig 3.6). One example of a detector uses a silicon chip charge-coupled

Device (CCD). In this device, a phosphor is used to convert x-ray photons to visible photons. These visible photons are transferred to a CCD chip and are then stored in the pixels of the chip through the generation of electrons. A voltage applied to the chip maintains these electrons until a readout is made which basically involves shifting the charge to a readout amplifier. Every single row of pixels is read out, and a stationary controller converts the positions of the pixels with their charges to x, y coordinates on the detector face to corresponding intensities. The XRD data will, therefore, be a plot of intensities versus the diffraction angle 2θ. Because the crystal structure of the elements and compounds is different, unique diffraction patterns are observed. Thus, the diffraction patterns act as finger prints of the elements and compounds in the sample under investigation.
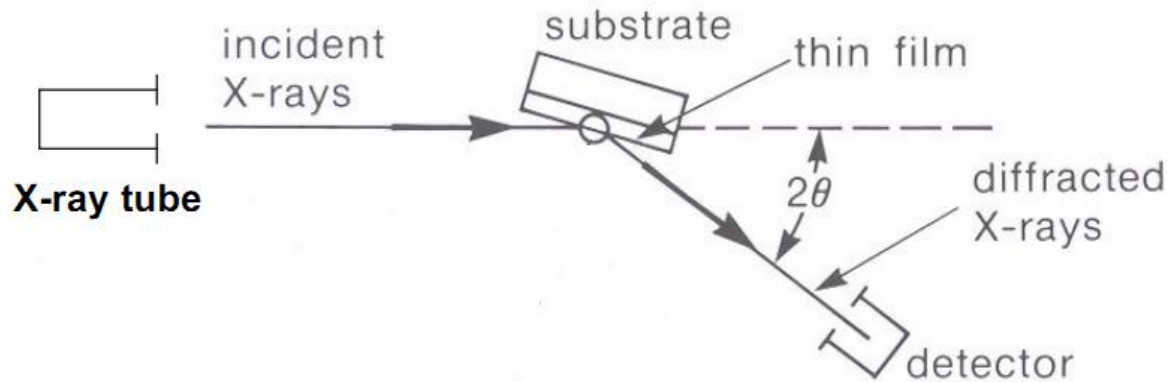

Fig. 3.6 Schematic representation of an x-ray experiment [13].

XRD data in this study were analysed by using X'pert software [14]. X'pert software uses a search-match algorithm of the peaks and profile data to identify the phases in the sample with the help of reference databases.

3.5.4 Scanning Electron Microscope

A scanning electron microscope (Fig 3.7) is a high-resolution microscope that uses electrons for imaging [2, 15]. The electron gun in the heated filament creates the electrons. These electrons guided into the aperture by a lens system impinge on the sample surface thereby stimulating the emission of further electrons. The impinging electrons that are reflected are called backscattered electrons. The electrons that are emitted from the sample are called secondary electrons, and these have less energy (<50 eV) when compared to the highly energetic backscattered electrons [16].

The signal from the secondary electrons is used to study the surface topology of the sample. The impinging electrons may also lead to the production of x-rays wich can be used to find the chemical composition of the sample with the help of a technique called energy dispersive x-rays spectroscopy (EDS). The backscattered electrons are used to form an electron backscatter diffraction (EBSD) image which can be used in determining the crystal structure of the sample. In this study, a Zeiss Ultra 55 field emission scanning electron microscope was used, and the images were obtained by backscattered electrons using an inlens detector.
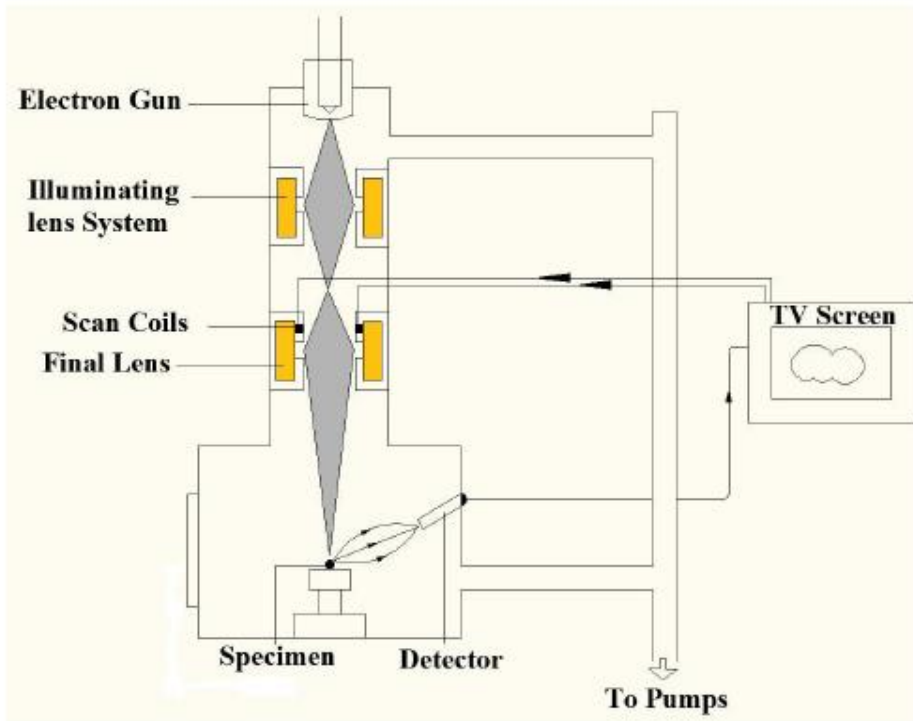

Fig 3.7 Scanning electron microscope [2].

3. 6. Reference

[1] T. Ayalew T, SiC Semiconductor Devices: Technology, Modeling and Simulation, Ph.D. Thesis, Technical University of Vienna, (2004).

[2] A. Chawanda, Electrical and structural characterisation of metal germanides, Ph.D. Thesis, University of Pretoria, (2010).

[3] S.M.M. Coelho, Electrical characterisation of process induced defects in germanium, Ph.D. Thesis, University of Pretoria, (2014).

[4] J.J. Grob, P. Siffert, *Rutherford Backscattering Spectroscopy*, Progress in Crystal Growth and Characterization, Volume 8, Issues 1–2, Pages 1-187 (1984).

[5] W. Chu, J.W. Mayer, M.A. Nicolet, Backscattering Spectrometry, Academic Press Inc, (1978).

[6] U.V. Toussant, K. Krieger, R. Fischer, V. Dose, Profile Reconstruction from Rutherford backscattering Data, Physics Data conference (1998).

[7] IAEA, Instrumentation for PIXE and RBS, Vienna, (2000).

[8] L.R. Dolittle, *Algorithms for the rapid simulation of Rutherford backscattering spectra*, Nuclear Instruments and Methods in Physics Research Section B: Beam Interactions with Materials and Atoms, (1985).

[9] W.E. Smith, G. Dent, Modern Raman Spectroscopy A Practical Approach, John Wiley & Sons, (2005).

[10] Thermo Scientific, Introduction to Raman Spectroscopy , Madison, (2008).

[11] John R. Ferraro, Kazuo Nakamoto, Chris W. Brown, Introductory Raman Spectroscopy, Second Edition, Elsevier, (2003).

[12] M. Bilcholz, Thin Film Analysis by X-Ray Scattering, Wiley-VCH Verlag (2006).

[13] A. Cunha, X-ray diffraction analysis, Instituto Superior Tecnico (2010).

[14] Panalytical, Total x-ray powder pattern analysis, Almelo (2009).

[15] W. Zhou, Z. L. Wang, Scanning Microscopy for Nanotechnology Techniques and Applications, New York, Springer, (2006).

[16] T.T. Hlatshwayo, Diffusion of silver in 6H-SiC, Ph.D. Thesis, University of Pretoria, (2010).

CHAPTER 4

RESULTS FOR SOLID STATE REACTION AND DIFFUSION OF RUTHENIUM IN 4H-SIC AND 6H-SIC UNDER DIFFERENT ANNEALING ENVIRONMENTS.

4.1 Introduction

In this study, thin films of Ru of thickness 50 nm were deposited on n-type 4H-SiC (with an epilayer) and n-type bulk grown 6H-SiC as described in section 3.2. The samples were annealed in a vacuum, air, and argon. RBS, Raman spectroscopy, SEM, and XRD were used to study the reaction, diffusion and microstructure evolution at the Ru-SiC interface. RBS was used to characterise the interface of all the samples due to the fact that it was readily available to the researcher. Raman spectroscopy, SEM, and XRD were used to characterise a small number of samples due to the fact that they were not readily available.

4.2 Solid state reaction of ruthenium with 4H-SiC and 6H-SiC.

4.2.1 Ru reaction and diffusion in 4H-SiC and 6H-SiC under atmospheric annealing environment.

RBS analysis of the thin films of Ru/4H-SiC annealed in air indicate a pure Ru peak for the as-deposited sample (Fig. 4.1), and the commencement of oxidation at a temperature of 400 $^{\circ}$C (Fig. 4.2) as seen by the presence of an oxygen peak at channel number 178. There is increased oxidation as evidenced by a more pronounced oxygen peak for the Ru/4H-SiC sample annealed at 500 $^{\circ}$C (Fig.4.3). Diffusion of Ru into 4H-SiC commences at this temperature as evidenced by the slight broadening of the base of the Ru signal. Extensive interdiffusion of Ru and Si at the Ru-4H-SiC interface is observed after annealing at a temperature of 600 $^{\circ}$C (Fig. 4.4), as evidenced by the widening of the base and the reduction in height of the Ru signal. Oxidation continues to take place at this temperature as well. Depth profiles of Ru/4H-SiC which were obtained from RUMP [1] simulations of RBS spectra also indicate a pure Ru layer on the surface (Fig 4.5), surface oxidation at 400 $^{\circ}$C (Fig. 4.6) and Ru diffusion into 4H-SiC (Fig. 4.7) at 500 $^{\circ}$C. The sharp edges in the depth profile are a result of the simulation procedure which emanates from our limited knowledge of the exact sample profile and finite detector resolution. It should be understood that the real profiles could be more smooth than portrayed but there is no way to decide on this. Therefore the simplest model that fits the data has been used. In this study, Ru oxidation commences at a much lower temperature when compared with the work of Roy *et al* [2], where Ru oxidation was observed only after annealing at a temperature of 800 $^{\circ}$C. It should be mentioned that their investigation conditions were slightly different from this work as they were using 3C-SiC and the annealing environment was 2% H_2 diluted in the air.

The analysis of XRD spectra of the samples by using X'Pert Highscore plus software   indicates the presence of pure Ru, SiC (the diffraction peak positions are indicated in the peak list table) and the formation RuSi (Fig.4.8) as indicated by diffraction peaks at 36°, 51.6°, 64°, 77°, 88° and 98° at an annealing temperature of 600 °C. According to Roy *et al* [2], the formation of different phases of silicides will depend on the atomic percentage of silicon in the system, and near the equi-atomic composition two distinct crystal structures of RuSi have been reported to exist. The oxidation of Ru has not been indicated by the XRD. One possible explanation may be that the oxide formed may be too low to be detected by XRD. There is also a heavy suspicion that the oxide formed in Ru/4H-SiC is not the semiconducting oxide RuO_2 but other oxide compounds such as gaseous RuO and low temperature melting RuO_4 or RuO_3 which is known to vaporise at 1200 °C or Ru_2O_3 which is largely unknown[3, 4]. These oxides are rare and may not have been available in the database of X'Pert software. Furthermore, in the Raman spectrum of the Ru/4H-SiC sample annealed at 600 °C (Fig.4.8), there is a clear absence of RuO_2 peaks [3] which is an indication of the absence of the Ru oxide with this stoichiometry. Instead, there is a clear peak of Ru_2Si_3 at position 203 cm^{-1} [5], and typical three main phonon bands of 4H-SiC with A1, and E2 symmetries [6]. The planar E2, transverse optic E1, and the longitudinal optic A1 modes are at positions 776 cm^{-1}, 797 cm^{-1} and 964 cm^{-1} respectively.
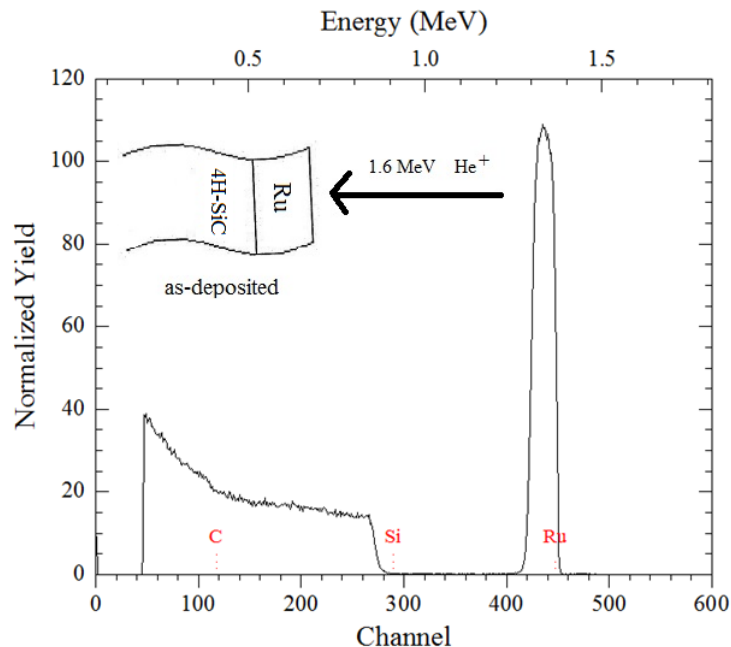
Fig.4.1. RBS spectra of as-deposited Ru/4H-SiC obtained by using 1.6 MeV of helium ions. The spectrum indicates the presence of a pure Ru on the surface.
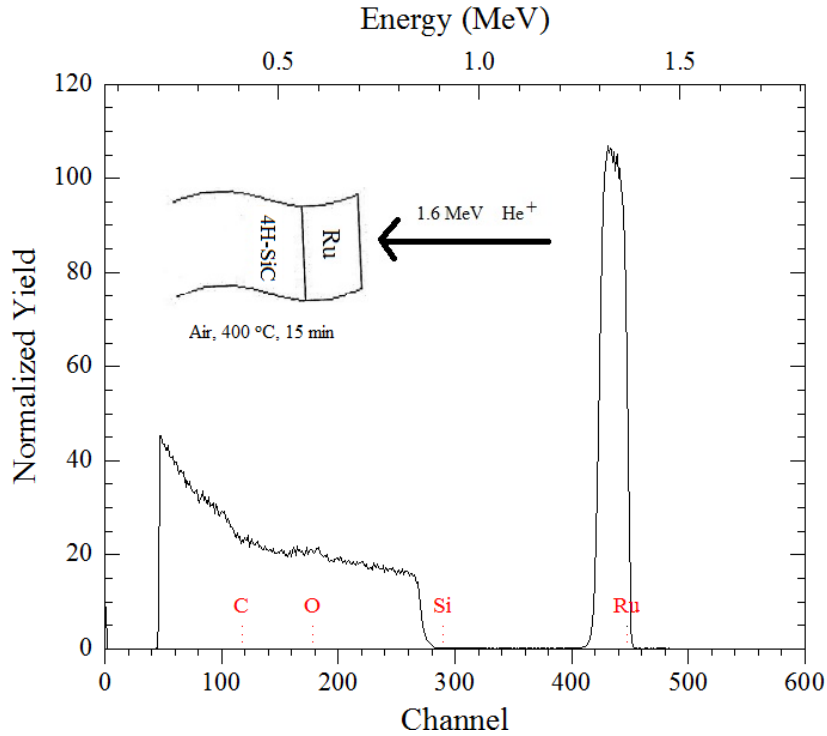

Fig.4.2. RBS spectra of Ru/4H-SiC annealed in air at 400°C obtained by using   1.6 MeV of helium ions. Oxidation commences at this temperature as evidenced by the appearance of an oxygen peak at channel number 178.
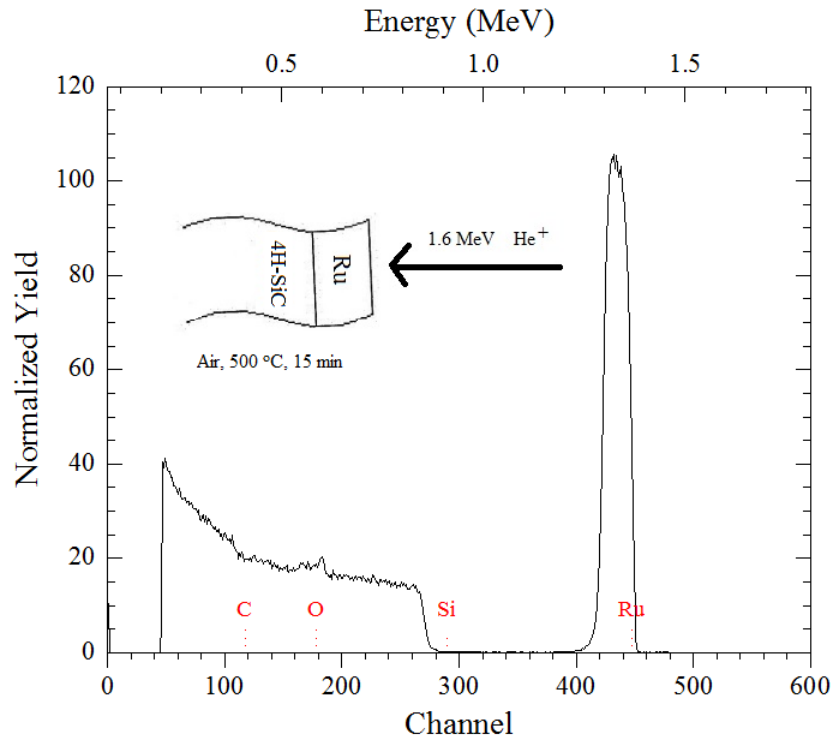
Fig.4.3. RBS spectra of Ru/4H-SiC annealed in air at 500ºC obtained by using 1.6 MeV of helium ions. More oxidation takes place at this temperature as indicated by a pronounced oxygen peak at channel number 178. Diffusion of Ru into 4H-SiC commences at this temperature as well.
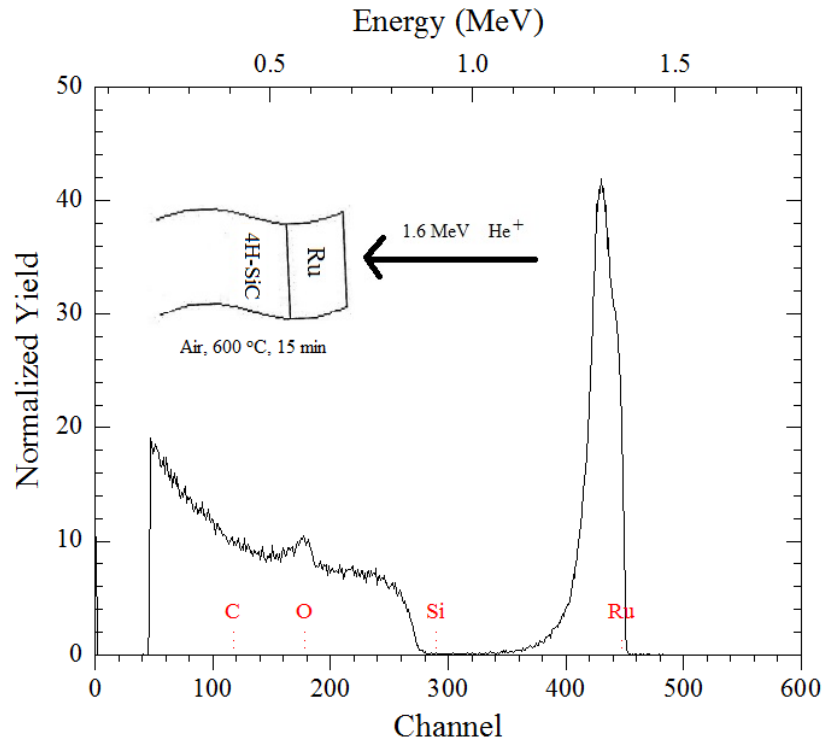
Fig.4.4. RBS spectra of Ru/4H-SiC annealed in air at 600ºC obtained by using 1.6 MeV of helium ions. Diffusion of Ru into 4H-SiC commences at this temperature as evidenced by the widening of the base and reduction in height of Ru signal.
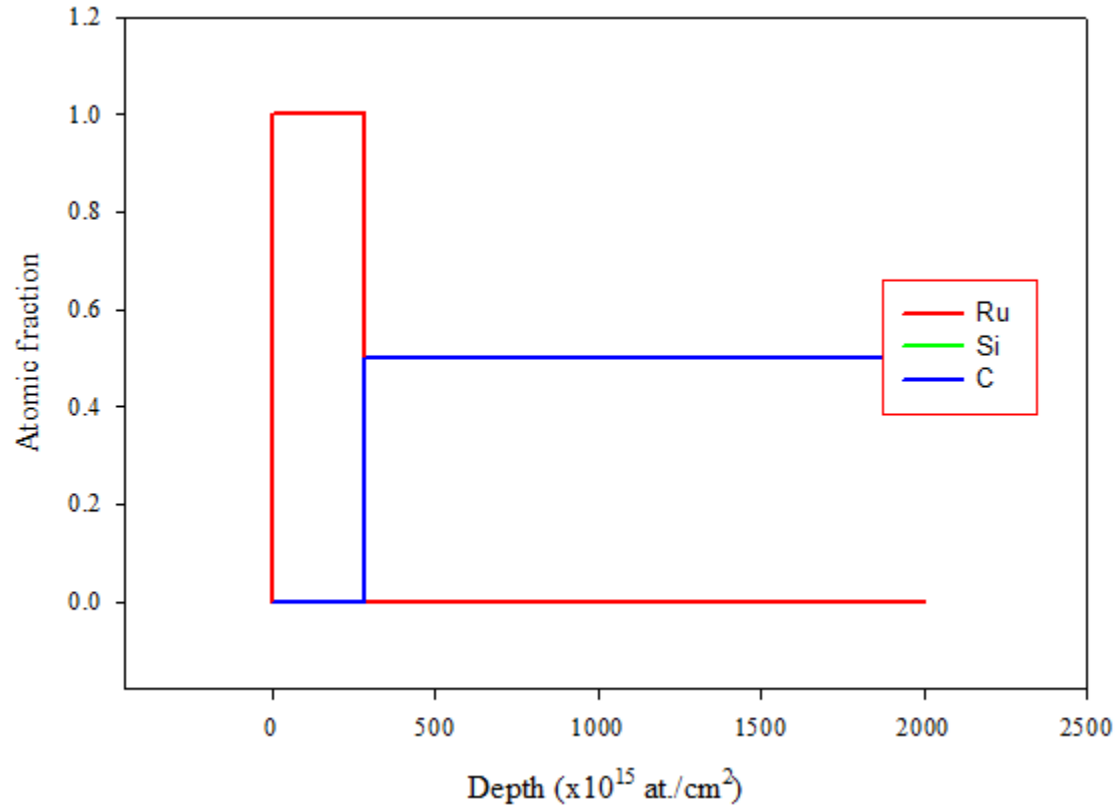
Fig 4.5. Depth profile of as-deposited Ru/4H-SiC, which indicates the presence of pure Ru on the surface of 4H-SiC.
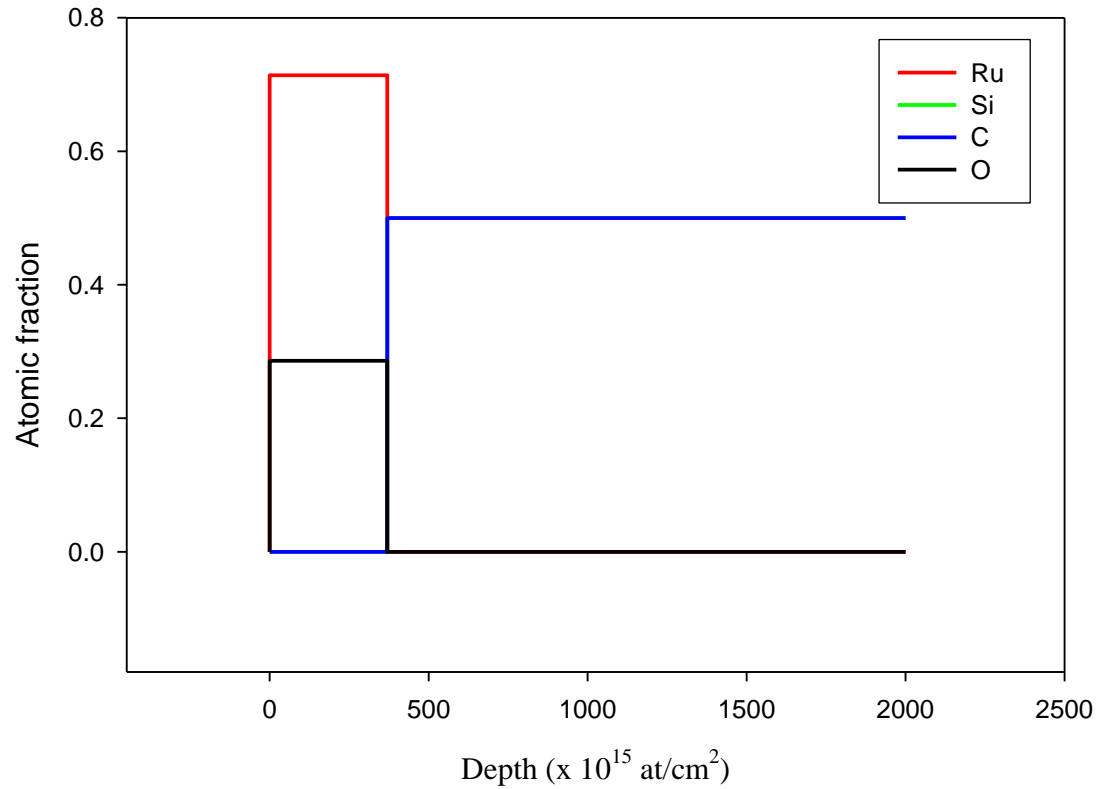
Fig 4.6. Depth profile of Ru/4H-SiC annealed in air at 400 ºC. Oxidation of Ru is observed to take place at this temperature.
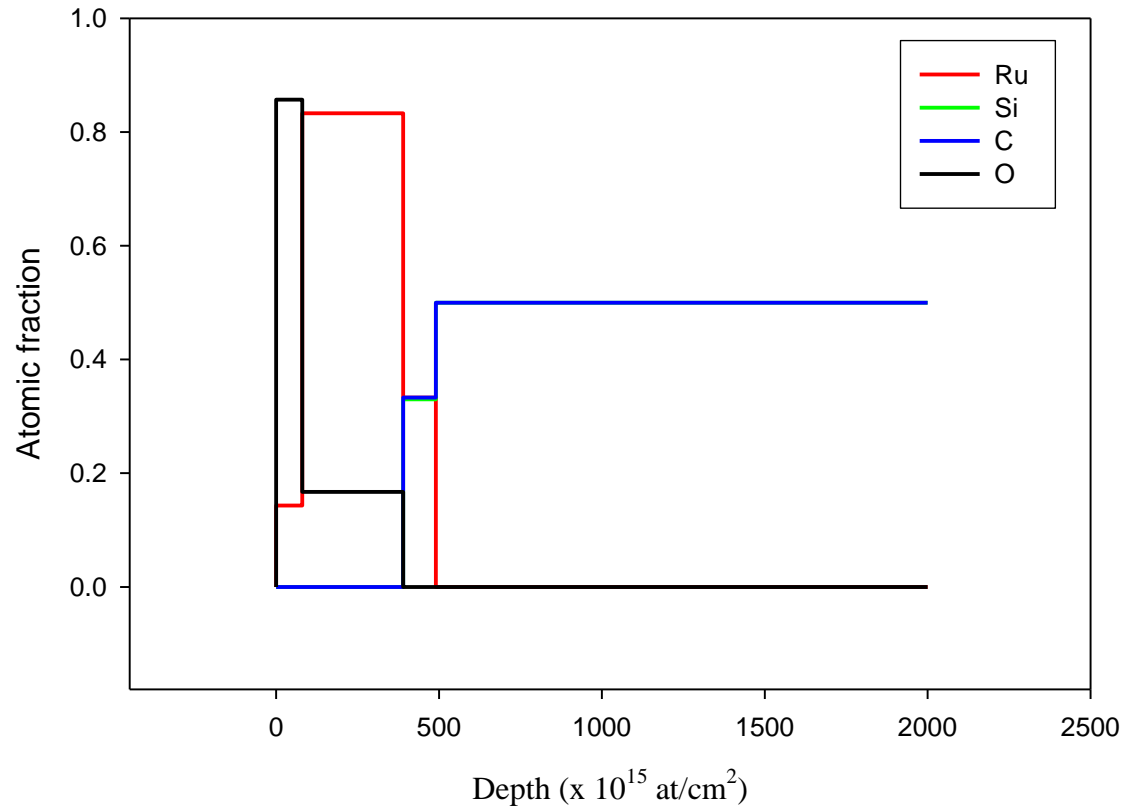
Fig. 4.7. Depth profile of Ru/4H-SiC annealed in air at 500 ºC. Diffusion of Ru into 4H-SiC and oxidation of Ru are observed at this temperature.
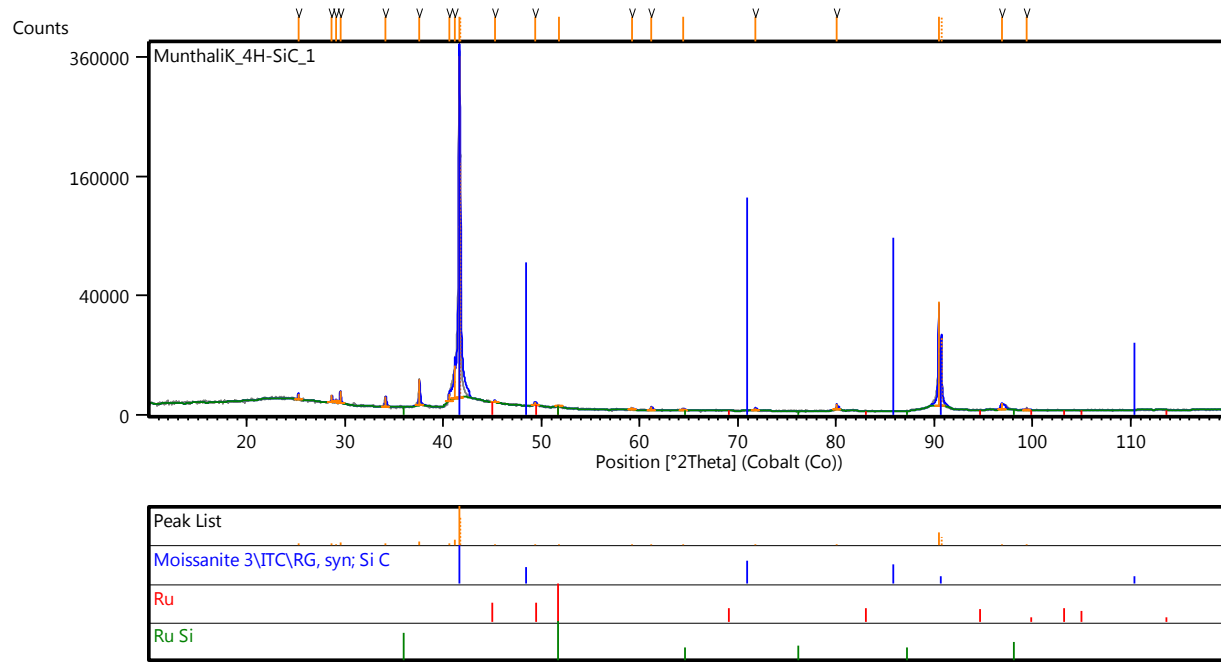
Fig .4.8. XRD spectra of Ru/4H-SiC annealed in air at 600 ºC. The spectrum indicates the formation of RuSi and the presence of Ru and SiC.
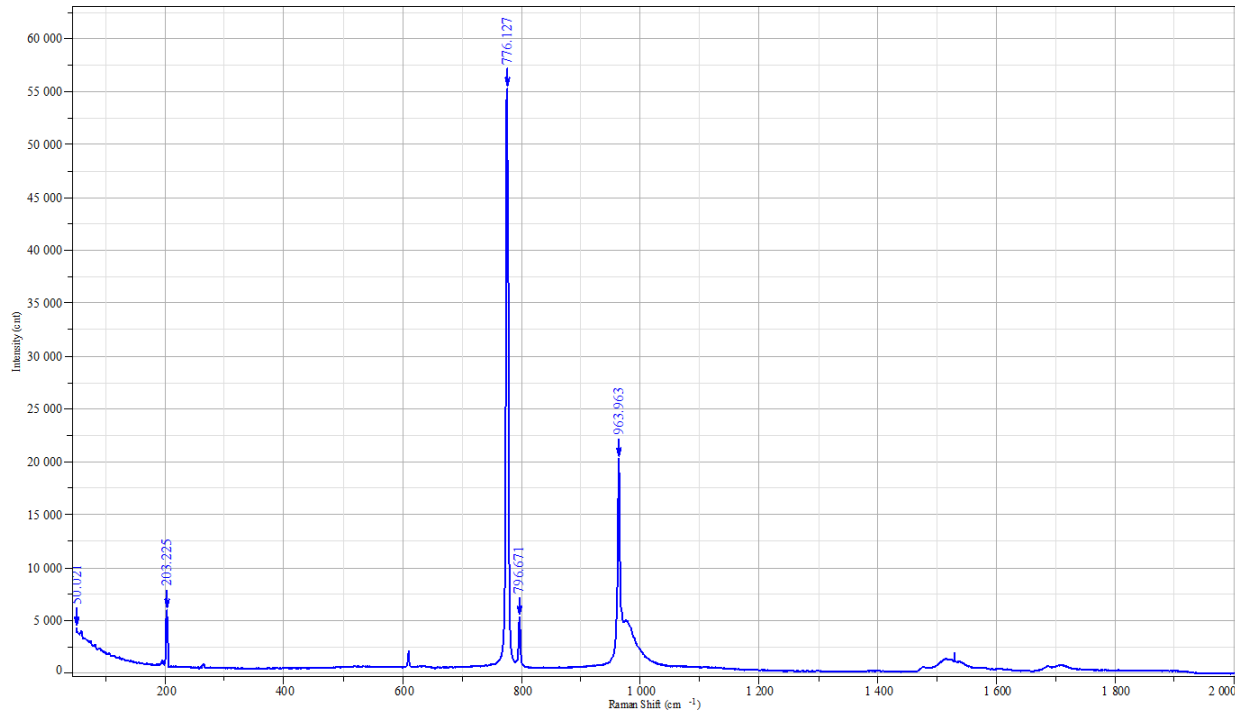
Fig. 4.9. Raman spectra of Ru/4H-SiC annealed in air at 600 °C. The spectrum indicates the formation of Ru_2Si_3 as indicated by the peak at position 203 cm^{-1}, and the presence of SiC as evidenced by peaks at positions 776 cm^{-1}, 797 cm^{-1} and 964 cm^{-1}.

RBS spectrum of the as-deposited thin film of Ru/6H-SiC annealed in the air indicates the presence of a pure Ru (Fig. 4.10). Oxidation is observed to commence at a temperature of 400 °C (not shown), and is seen to increase (Fig. 4.11) after annealing at 500 °C as indicated by a pronounced oxygen peak at channel number 178. Inter-diffusion of Ru and Si at the Ru/6H-SiC interface is also observed after annealing at a temperature of 500 °C (Fig. 4.11), as evidenced by the widening of the base and reduction in height of the Ru signal. At 600 °C, the inter-diffusion of Ru and Si at the Ru/6H-SiC interface is very deep as evidenced by the joining of the Ru and Si signals (Fig.4.12) at the base and the reduction in height of Ru signal. Oxidation of Ru also increases as indicated by a large height of the oxygen peak.

The analysis of XRD data by using X'Pert Highscore plus software provides evidence of the formation of RuO_2 in Ru/6H-SiC at 600 °C with diffraction peaks (Fig 4.13) at 41°,69°, and 74° which correspond to the indexed planes of crystals of RuO_2 (020), (301) and (311) respectively [7].

There are other RuO_2 diffraction peaks at 33°, 42° , 47° and other positions as indicated in the peak list table. There is also evidence of RuSi as evidenced by diffraction peaks at 36°, 51.6°, 64°, 77°, 88° and 98°. The XRD spectrum also indicates the presence of SiC and Ru in the sample whose peak positions are indicated in the peak list table. The Raman spectrum of Ru-6H-SiC annealed at 600 °C air (Fig. 4.14) indicates typical Raman bands of RuO_2 at positions 524, 643 and 711 cm^{-1}. These Raman bands are called E_g, A_{1g} and B_{2g} vibrational modes respectively of RuO_2 [3,8].
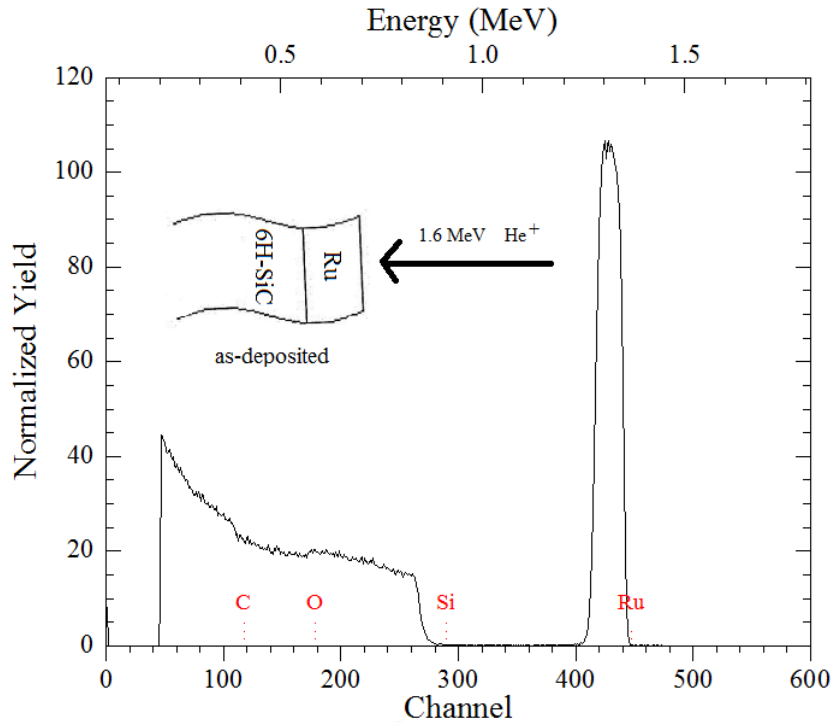
Fig. 4.10. RBS spectrum of as-deposited Ru/6H-SiC obtained by using 1.6 MeV helium ions. The spectrum shows the presence of pure Ru at the surface.

Fig .4.11. RBS spectra of Ru/6H-SiC annealed in air at 500 ºC obtained by using 1.6 MeV helium ions. The spectrum indicates the oxidation of Ru and diffusion of Ru into SiC as evidenced by the widening base of Ru signal.
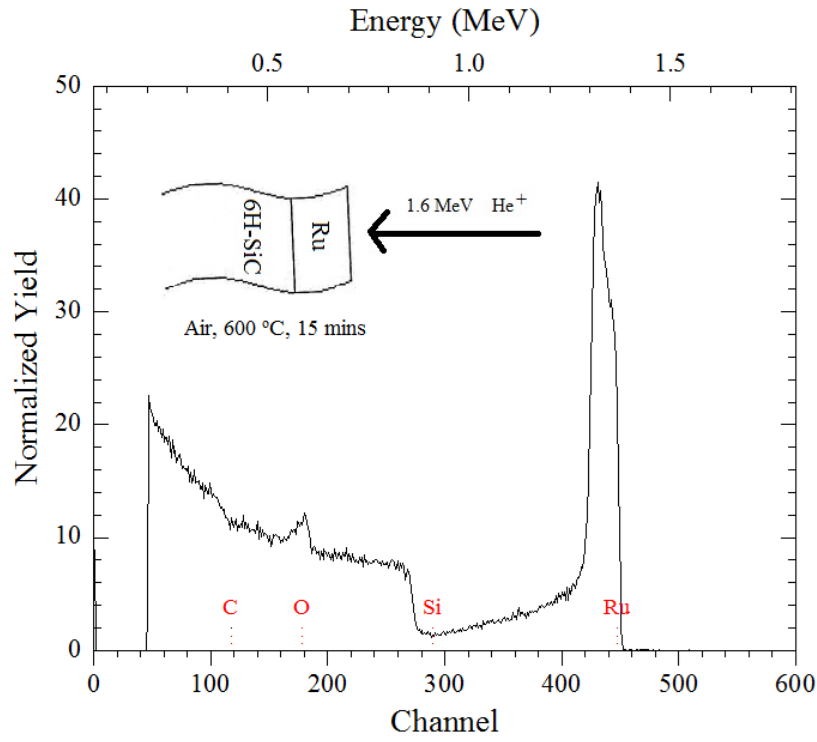
Fig .4.12. RBS spectra of Ru/6H-SiC annealed in air at 600 °C obtained by using 1.6 MeV helium ions. Extensive interdiffusion of Ru and Si elements at the interface takes place at this temperature as indicated by the joining at the base of the Ru and Si signals and the reduction in the Ru signal height.
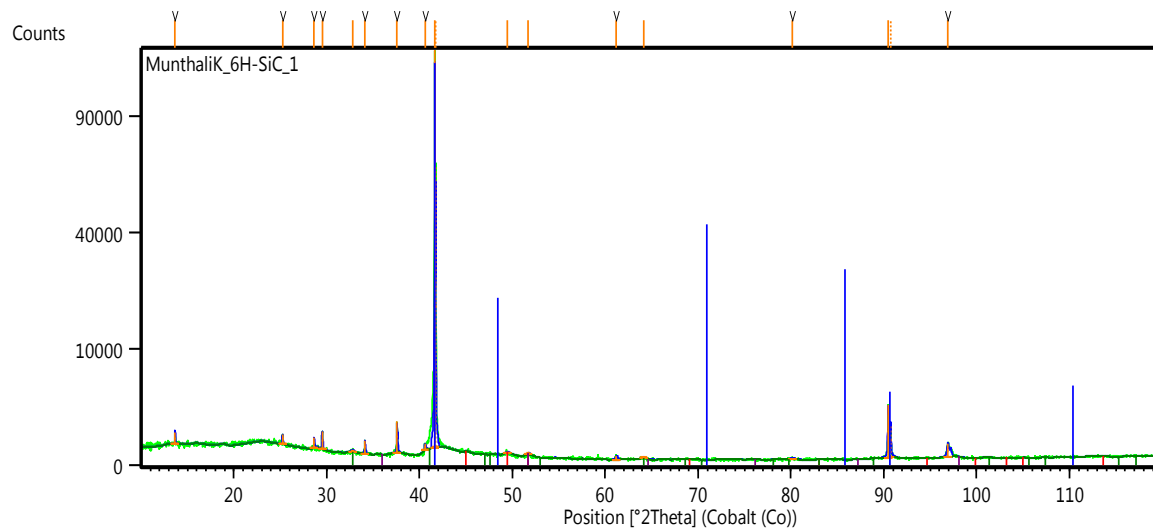
Fig. 4.13. XRD spectrum of Ru/6H-SiC thin film sample annealed in air at 600 °C. The spectrum indicates the formation of RuSi and RuO_2, and the presence of Ru and SiC.
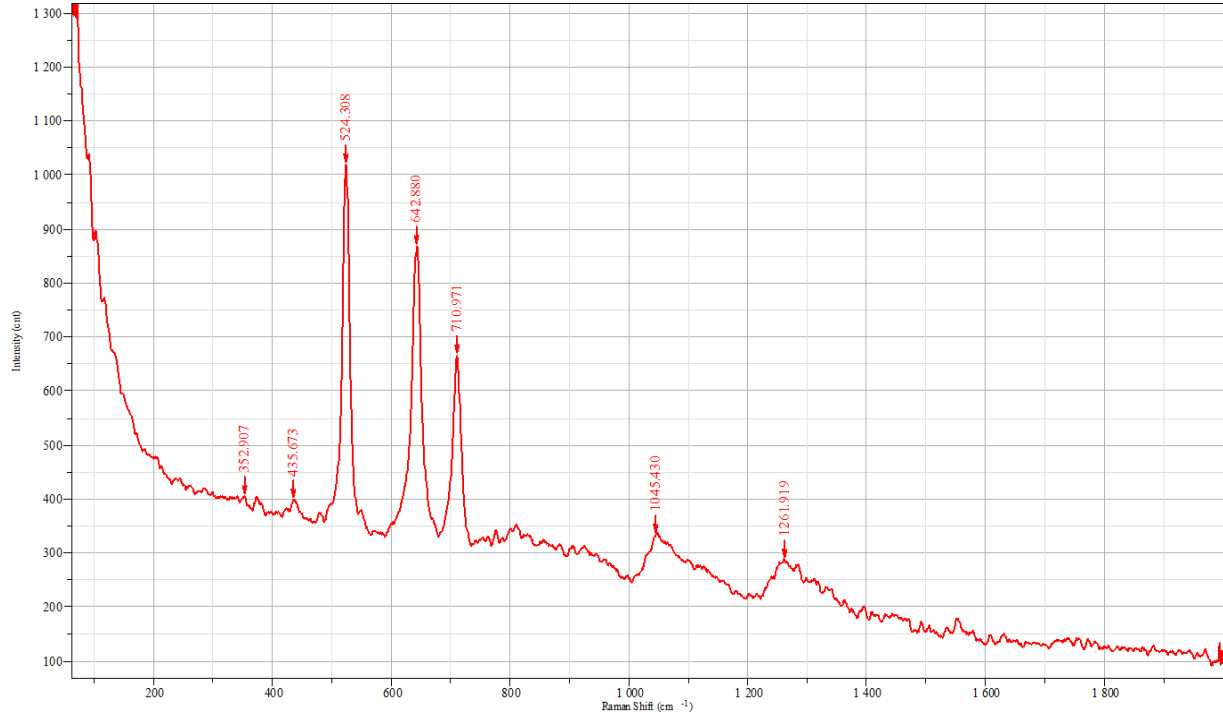
Fig. 4.14. Raman spectrum of Ru/6H-SiC thin film sample annealed in air at 600 $^\circ$C. The spectrum indicates the formation of RuO_2 as evidenced by peaks at positions 524, 637 and 710 cm^{-1}.

4.2.2 Ruthenium reaction and diffusion in 4H-SiC and 6H-SiC under argon annealing environment.

RBS analysis of as-deposited Ru/4H-SiC thin film (Fig.4.15) indicates the presence of a pure Ru on the surface. Ru silicide formation as indicated by a step on the high energy edge of Si, Ru oxide formation as evidenced by oxygen peak at channel 279, and Ru and Si inter-diffusion as shown by increasing base widths of both signals all appear to commence after annealing at 400 $^\circ$C (Fig. 4.16). At 800 $^\circ$C, the Ru and Si interdiffusion is very deep, and Ru oxidation is very high as exhibited by a pronounced oxygen peak (Fig. 4.17).

The Raman spectrum of as-deposited Ru/4H-SiC (Fig.4.18) shows a broad peak near position 1600 cm^{-1}, in addition to a smaller peak near 1400 cm^{-1}, that can be attributed to second-order Raman processes of 4H-SiC which appear in the same spectral region as the second-order Raman lines of 3C-SiC [9, 10].

For the Raman spectrum of the sample annealed at 900 °C (Fig.4.19), there are clear Ru_2Si_3 peaks at positions 173 cm^{-1} and 203 cm^{-1}, and RuO_2 peak appears at 610.1 cm^{-1} [5,11]. There is also an appearance of typical three main phonon bands of 4H–SiC with A1, and E2 symmetries [6] in the Raman spectrum. The planar E2, transverse optic E1, and the longitudinal optic A1 modes are at positions 776.4 cm^{-1}, 797 cm^{-1} and 975.6 cm^{-1} respectively.

Fig. 4.15. RBS spectrum of as-deposited Ru/4H-SiC obtained by using 1.4 MeV helium ions. The spectrum shows the presence of a pure Ru on the surface.
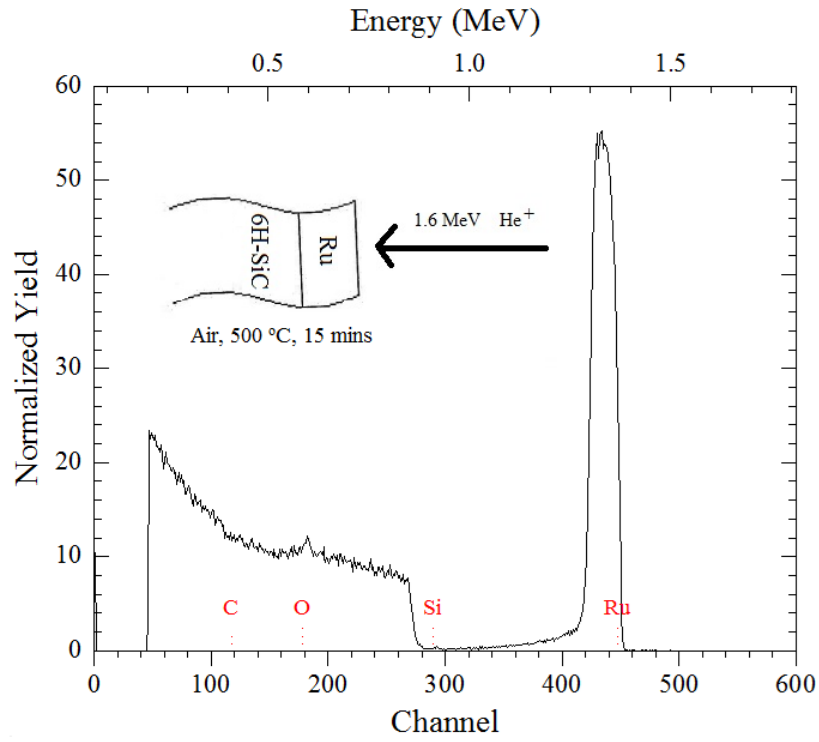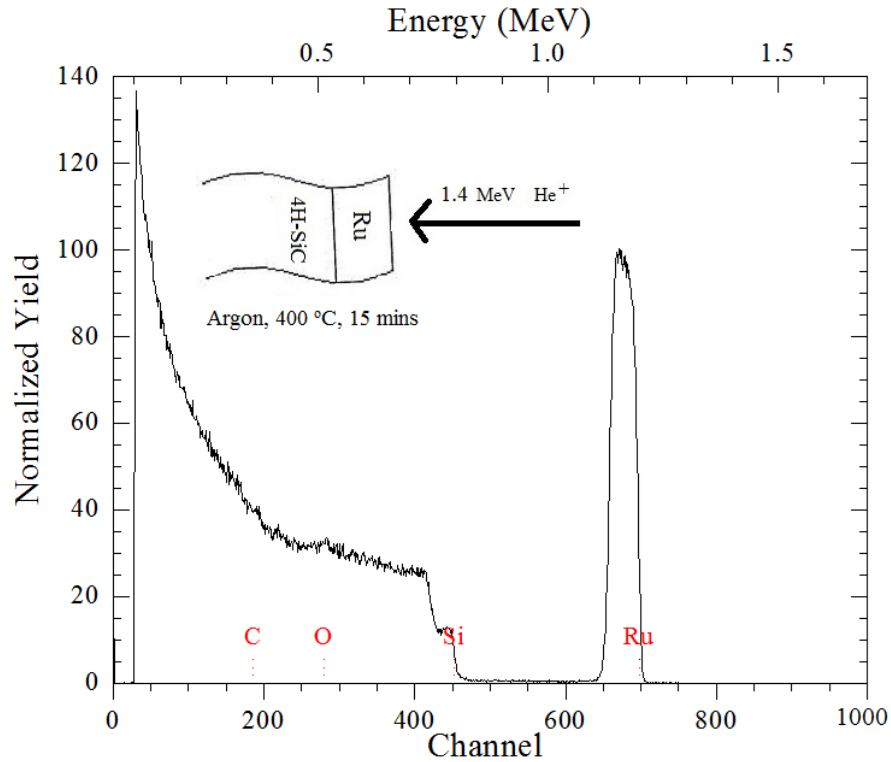

Fig. 4.16. RBS spectrum of Ru/4H-SiC annealed in argon at 400 °C obtained by using 1.4 MeV helium ions. The spectrum shows the formation of a silicide as indicated by a step on the high energy edge of Si. Oxidation is also observed to take place.
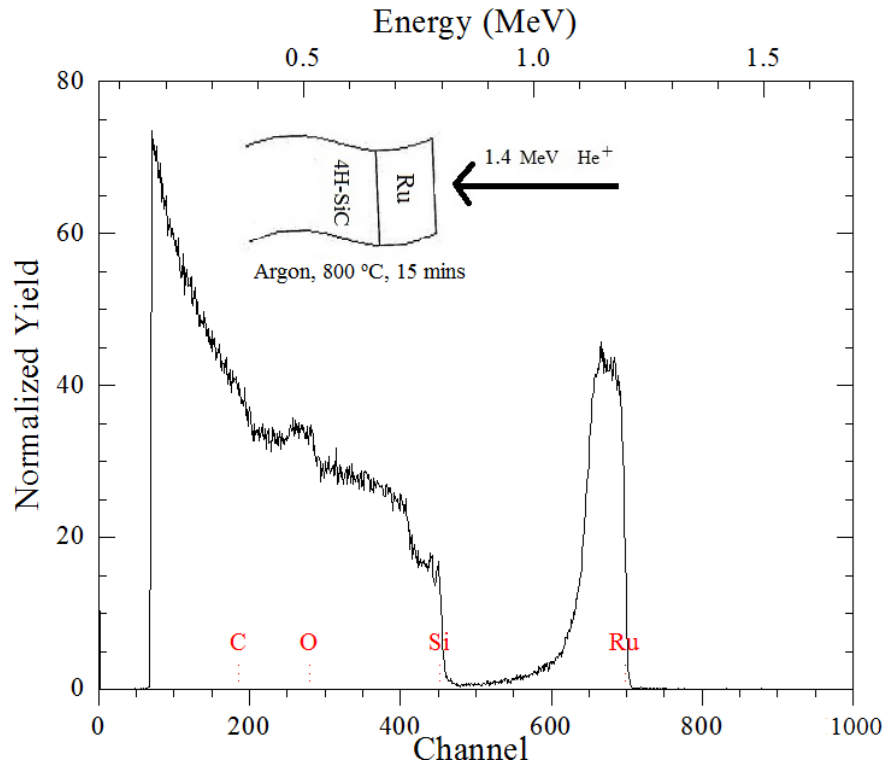
Fig. 4.17. RBS spectrum of Ru/4H-SiC annealed in argon at 800 ºC obtained by using 1.4 MeV helium ions. The spectrum indicates deep interdiffusion of Si, C, and Ru at the interface. Increased oxidation is observed to take place.
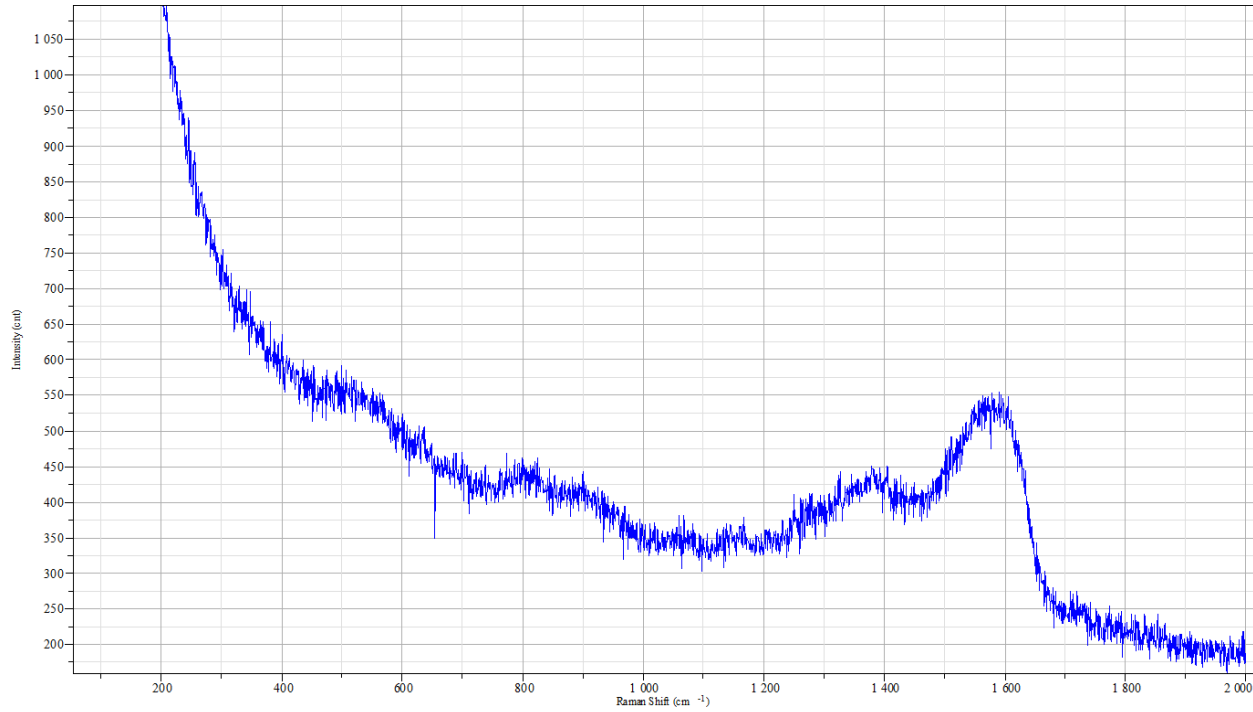
Fig 4.18. Raman spectrum of as-deposited Ru/4H-SiC. The spectrum shows second order Raman processes for 4H-SiC at positions 1600 cm^{-1} and 1400 cm^{-1}.
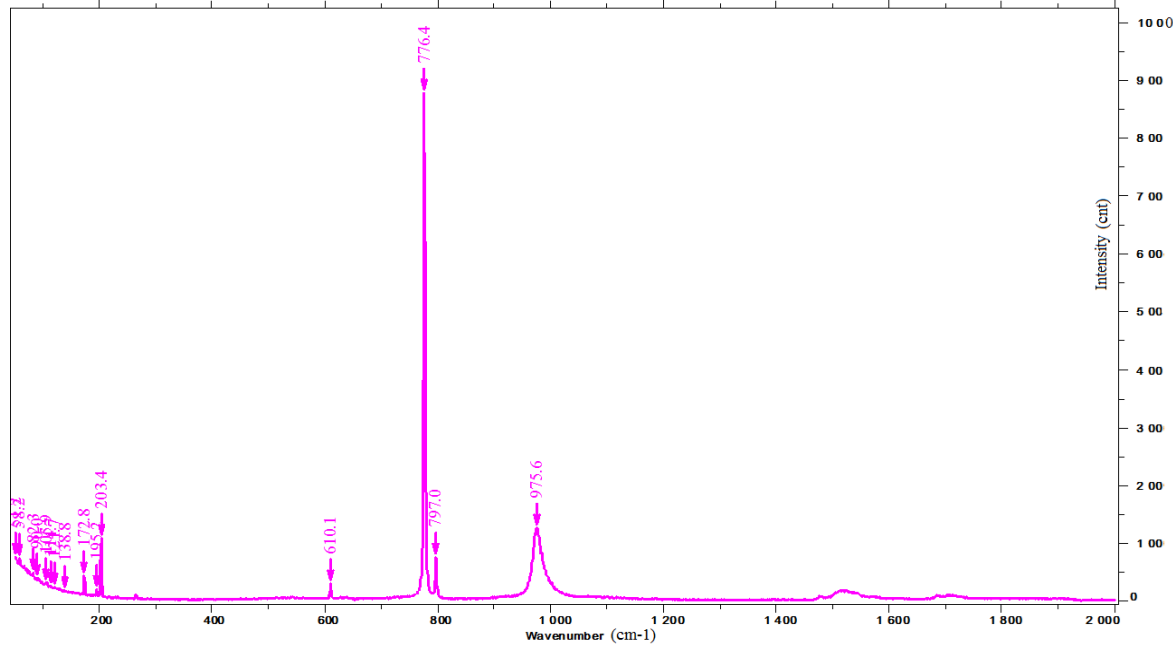
Fig 4.19. Raman spectrum of Ru/4H-SiC annealed in argon at 900 °C. The spectrum shows Ru_2Si_3 peaks at positions 173 cm^{-1} and 203 cm^{-1}, RuO_2 peak at 610.1 cm^{-1} and 4H–SiC peaks at positions 776.4 cm^{-1}, 797 cm^{-1} and 975.6 cm^{-1}.

RBS analysis of a thin film of as-deposited Ru/6H-SiC shows a pure film of Ru on the SiC (Fig. 4.20). The RBS spectra for samples annealed up to 400 °C (not shown) are similar to the as-deposited spectrum. Oxidation of Ru is observed at an annealing temperature of 500 °C (Fig. 4.21) as evidenced by a pronounced oxygen peak at channel 182. Diffusion of Ru into the SiC layer is seen to commence at 700 °C (not shown) and increases with annealing temperature as indicated by the widening of the base width of the Ru signal at 900 °C (Fig. 4. 22). There is increased oxidation of Ru at this temperature as demonstrated by a larger oxygen peak. At 1000 °C, it is observed that the interdiffusion of Ru and Si is so deep as indicated by the wide base of the Ru signal and the appearance of the Si at its surface energy position (Fig. 4.23).

The RBS data was also simulated by using RUMP. These simulations show that the as-deposited Ru/6H-SiC interface is located at 280x10^{15} at/cm^2 (Fig 4.24). Oxidation and minimal Ru, Si and C interdiffusion begin at an annealing temperature of 500 °C (Fig 4.25). Oxidation and

elements interdiffusion are observed to increase with annealing temperature (Fig 4.26), such that Ru is found at a depth of 1380×10^{15} at./cm^2 after annealing at 900 °C.

The charging current for RBS was unstable for the sample annealed at 1000 °C, and, therefore, its spectrum was not simulated.
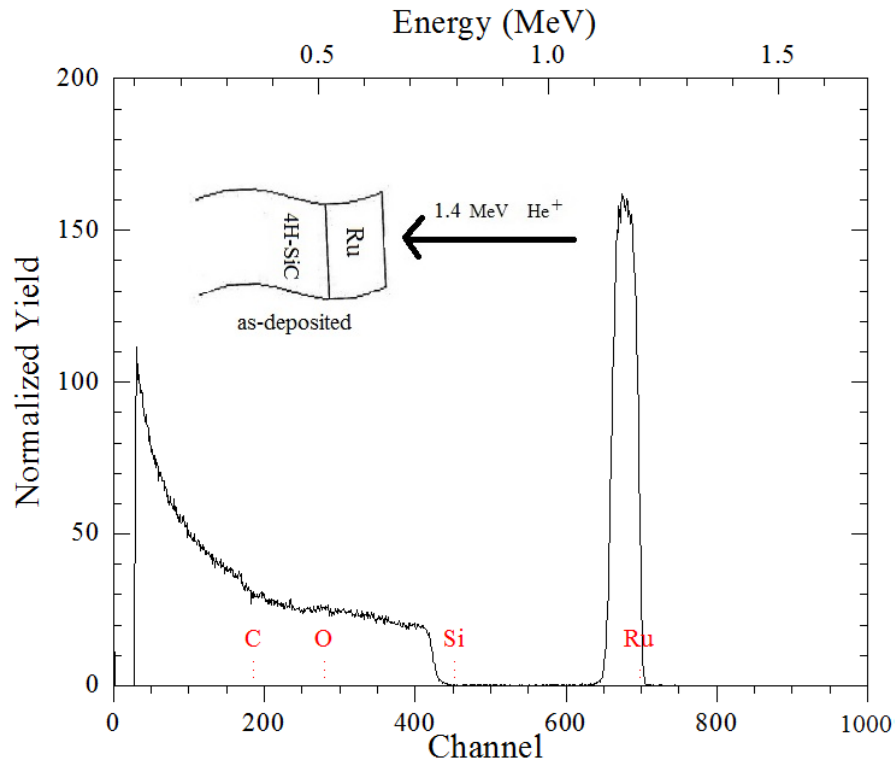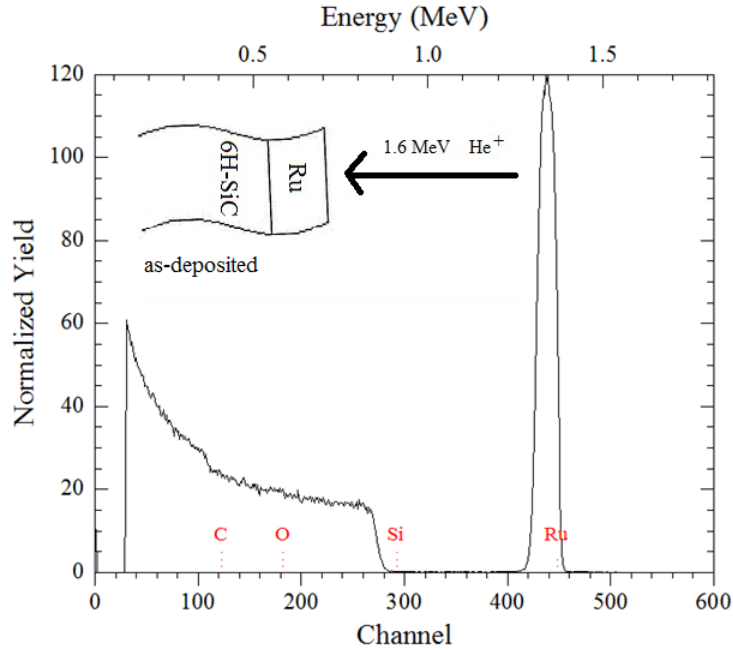

Fig. 4.20. RBS spectrum of a thin film of as-deposited Ru/6H-SiC obtained by using 1.6 MeV helium ions. The spectrum shows the presence of a pure Ru on the surface.
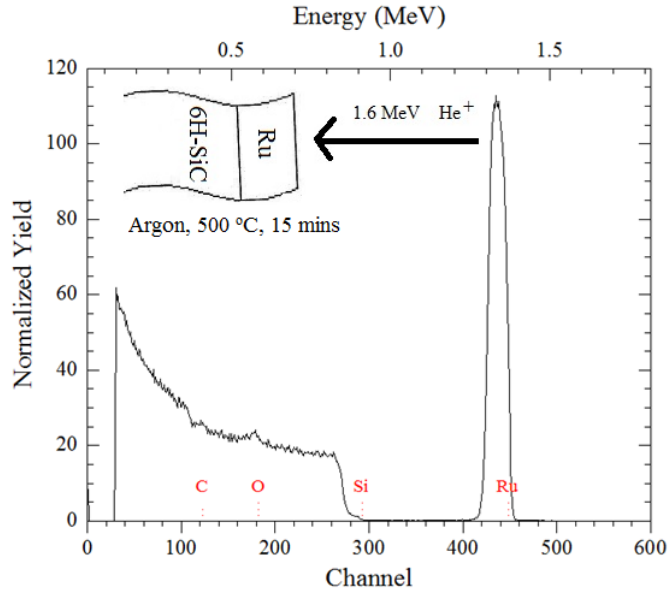
Fig. 4.21. RBS spectrum of a thin film of Ru/6H-SiC annealed in argon at 500 °C obtained by using 1.6 MeV helium ions. The spectrum shows oxidation of Ru as indicated by a sharp oxygen peak.
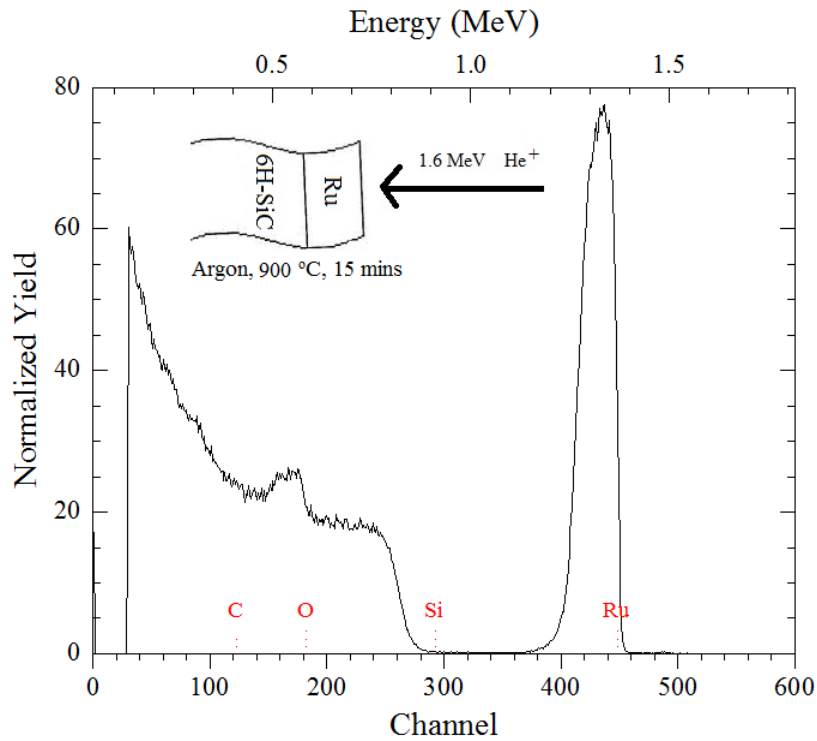
Fig. 4.22. RBS spectrum of a thin film of Ru/6H-SiC annealed in argon at 900 °C obtained by using 1.6 MeV helium ions. The spectrum indicates diffusion as indicated by the widening base and reduction in height of the Ru signal. Increased oxidation is also observed as indicated by a pronounced oxygen peak.
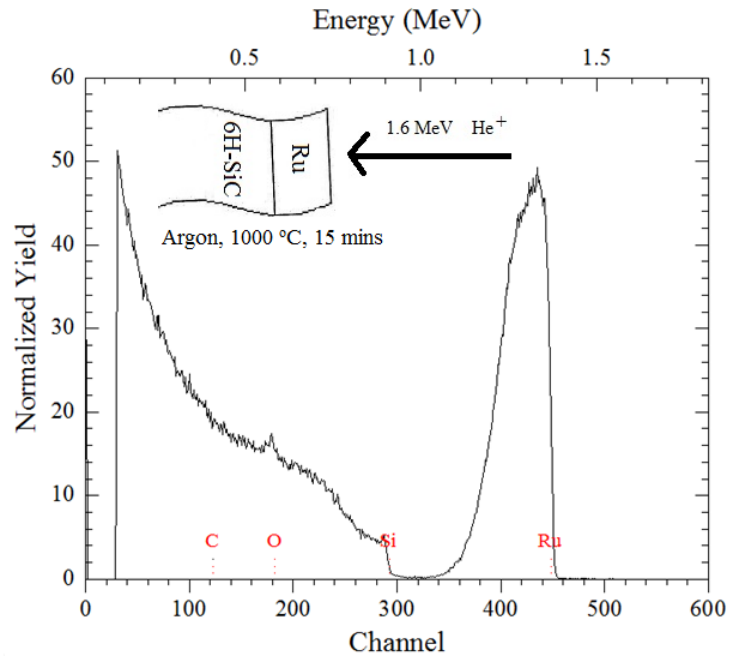
Fig. 4.23 RBS spectrum of a thin film of Ru/6H-SiC annealed in argon at 1000 °C obtained by using 1.6 MeV helium ions. The spectrum indicates oxidation and increased diffusion of the elements at the interface.
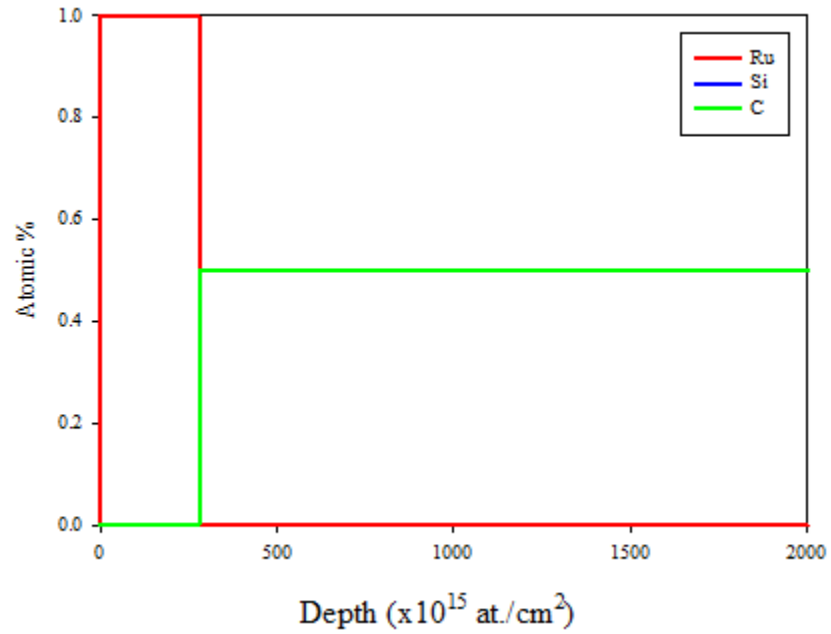
Fig 4.24 Depth profile of as-deposited Ru/6H-SiC. The profile shows a presence of pure Ru on the surface.
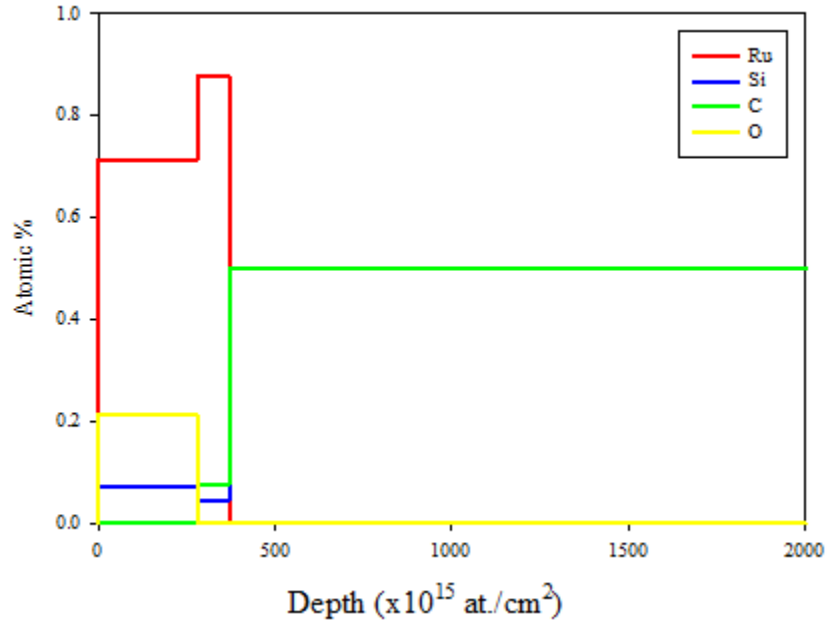
Fig 4.25 Depth profile of Ru/6H-SiC annealed in argon at 500 ºC. The profile shows oxidation and interdiffusion of elements at the interface.
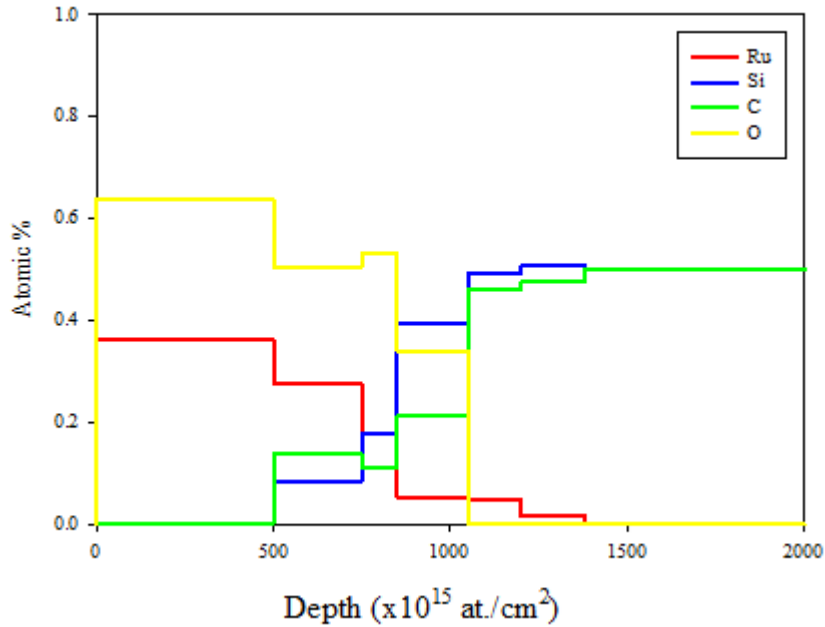
Fig 4.26 Depth profile of Ru/6H-SiC annealed in argon at 900 °C. The profile shows increased oxidation and elements interdiffusion.

SEM was used to analyse the as-deposited thin film sample of Ru/6H-SiC and the sample annealed at 500 °C to identify structural changes that took place during the annealing process. From the SEM images one can clearly see that the as-deposited thin film (Fig. 4.24) of ruthenium contains a mix of randomly oriented grains while the sample annealed at 500 °C (Fig. 4.25) is smooth which is an indication of the improvement in the grain quality of Ru or the microcrystalline nature of the ruthenium oxide formed during the annealing process.
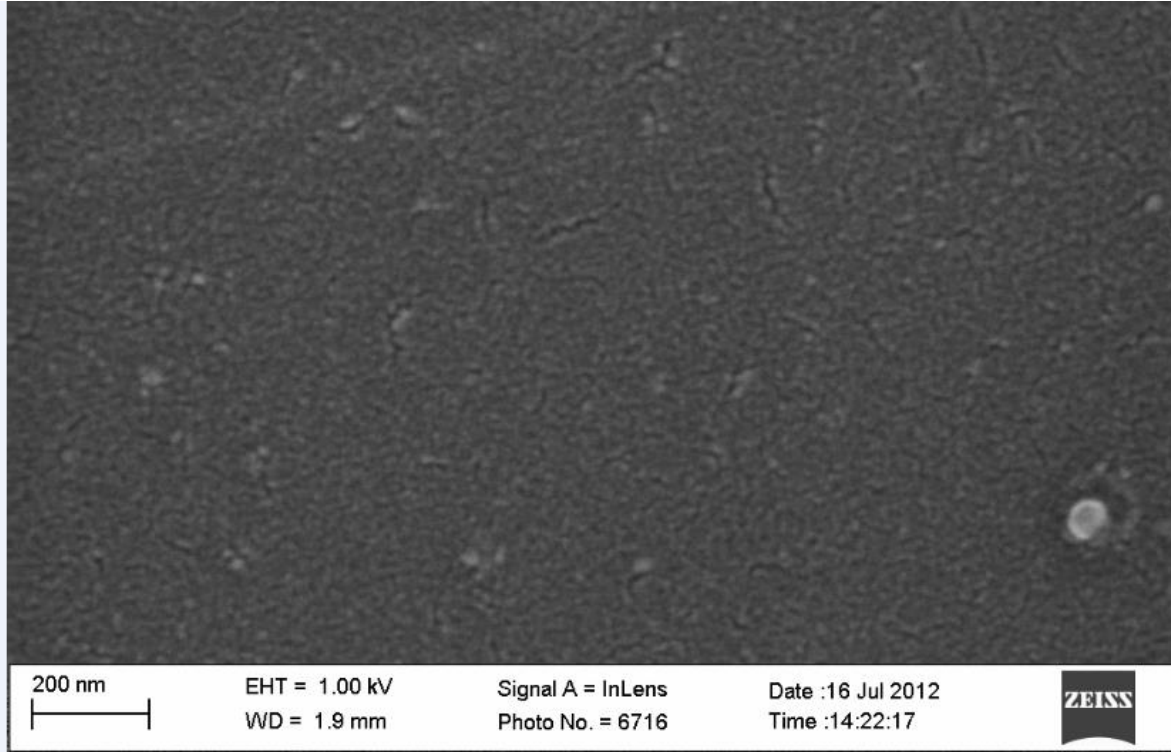
Fig. 4.27. SEM image of the as-deposited thin film of Ru/6H-SiC.

100 nm	EHT = 1.00 kV	Signal A = InLens	Date :16 Jul 2012	ZEISS
	WD = 2.0 mm	Photo No. = 6720	Time :14:25:48	
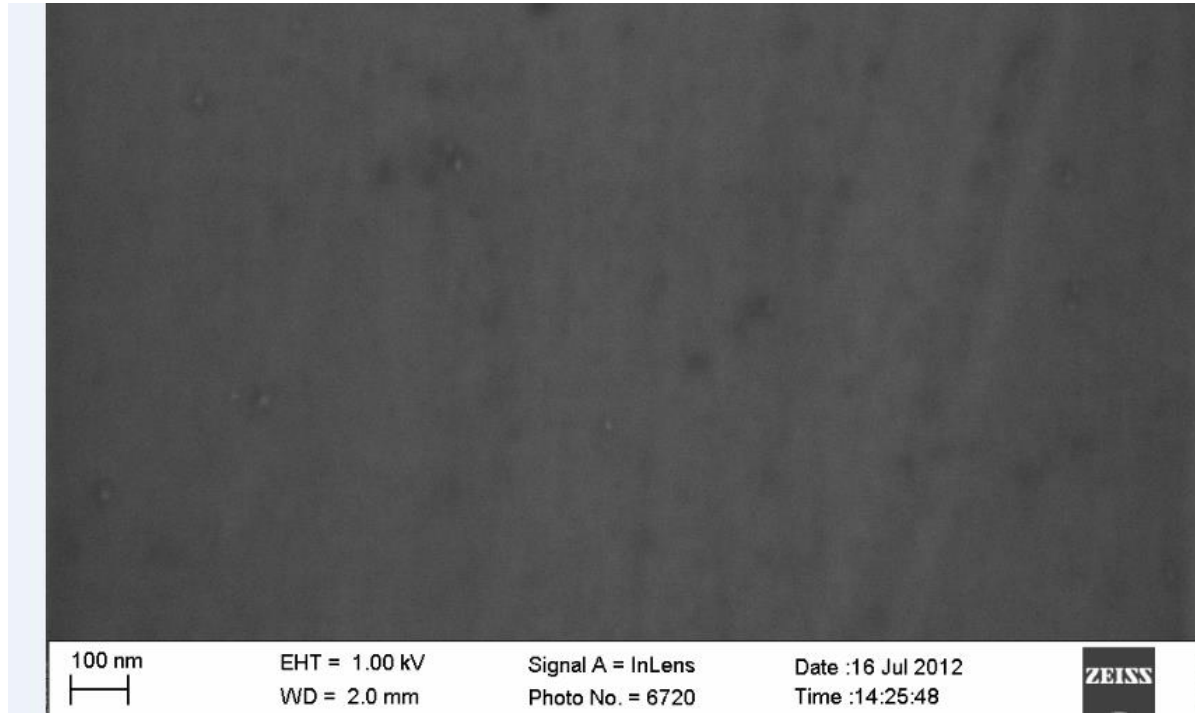
Fig. 4.28. SEM image of a thin film of Ru/6H-SiC annealed in argon at 500 ºC.

These findings are in agreement to those of Musschoot *et al* [12] who found that the as-deposited Ru on silicon had a random mix of grain orientation but when annealed in nitrogen at 800 ºC, the grains were preferentially out-of-plane oriented Ru (001) with a smooth surface.

4.2.3 Ruthenium reaction and diffusion in 4H-SiC and 6H-SiC under vacuum annealing environment.

RBS analysis of as-deposited Ru/4H-SiC displays the presence of pure Ru layer on the surface of 4H-SiC (Fig.4.29). The spectra for the samples annealed at 500 ºC and 600 ºC (not shown) are similar to the as-deposited. Silicidation is observed for the sample annealed at 700 ºC and 800 ºC. The silicide formation is evidenced by a step on the high energy edge of Si (Fig. 4. 30). The spectra for annealing temperatures of 900ºC and 1000ºC were similar to those of the sample annealed at 800ºC, and therefore, their spectra have not been included in this report.

Fig. 4.31 is the Raman spectrum obtained at room temperature of Ru-4H-SiC annealed at 1000°C. The spectrum shows the formation of graphite which is indicated by a clear carbon D peak at 1354 cm^{-1} and a G peak at 1589 cm^{-1} [13-16]. The carbon atoms diffuse through Ru and come from the silicide formation reaction of Ru and 4H-SiC. The intensity ratio of the D and G peaks can be used to approximate the size of the crystalline graphite or degree of disorder of the graphite that is formed [13]. The D band is generally thought to be an indication of disordered or defective hexagonal planar graphite structures. The G band originates from the stretching vibrations in the basal plane of ideal graphite, and a combination of D and G bands is generally regarded as an indication of polycrystalline graphitic structures [14]. The intensity ratio of D and G peaks (I_D/I_G) can be used to estimate the size of the graphite flakes or the degree of disorder of graphite. A lower ratio signifies a larger crystalline size or a higher degree of graphitization. Annealing the samples for a long time may lead to the production of graphene which has interesting electronic properties. The Raman spectrum also shows weak peaks at positions near 500 cm^{-1}, 750 cm^{-1} and 800 cm^{-1}. SiC has Raman peaks called planar E_2 mode, E_1 transverse optic (TO), and A_1 longitudinal optic (LO) mode centred at 777 cm^{-1}, 797 cm^{-1}, and 965 cm^{-1} respectively [6, 9, 18, 19]. However for this sample, the A_1 peak is very minute. The decrease in intensity of Raman peaks, and the appearance of new spectral bands in SiC, such as peaks near 500 cm^{-1} and 750 cm^{-1}, can be attributed to amorphisation of SiC during the donor implantation process [9]. According to Lu *et al* [10], the absence of a broad amorphous carbon peak at position 1510 cm^{-1} in the Raman spectrum is an indication of the absence (if not the minute presence) of this type of carbon in the sample. There is also an indication from Raman spectrum of the formation of Ru_2Si_3 as evidenced by the appearance of a small peak immediately left of 300 cm^{-1} position [19].
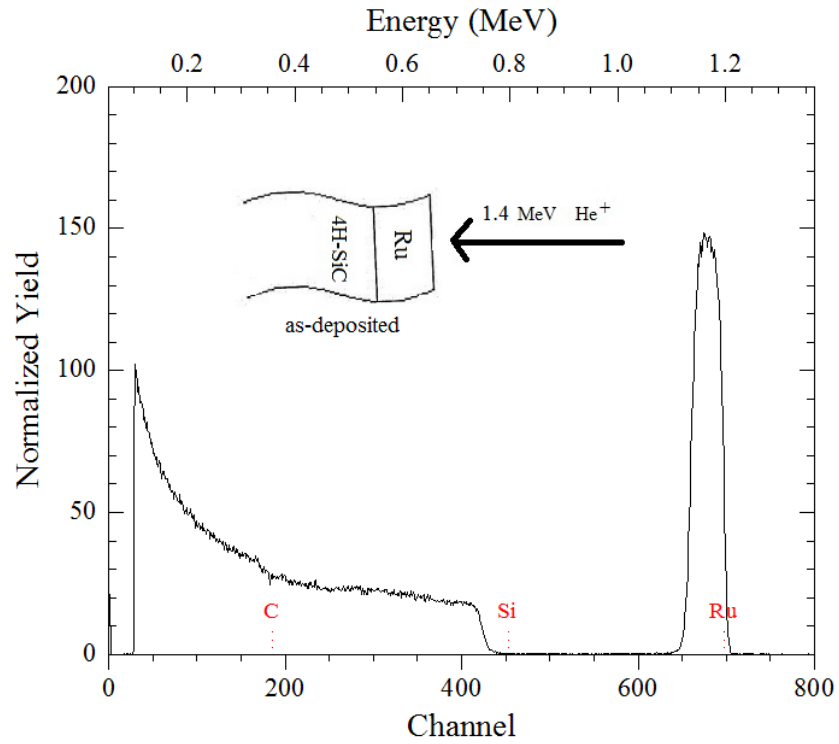
Fig.4.29.RBS spectrum of as-deposited Ru/4H-SiC film. The spectrum shows the presence of a pure Ru on the surface of 4H-SiC.
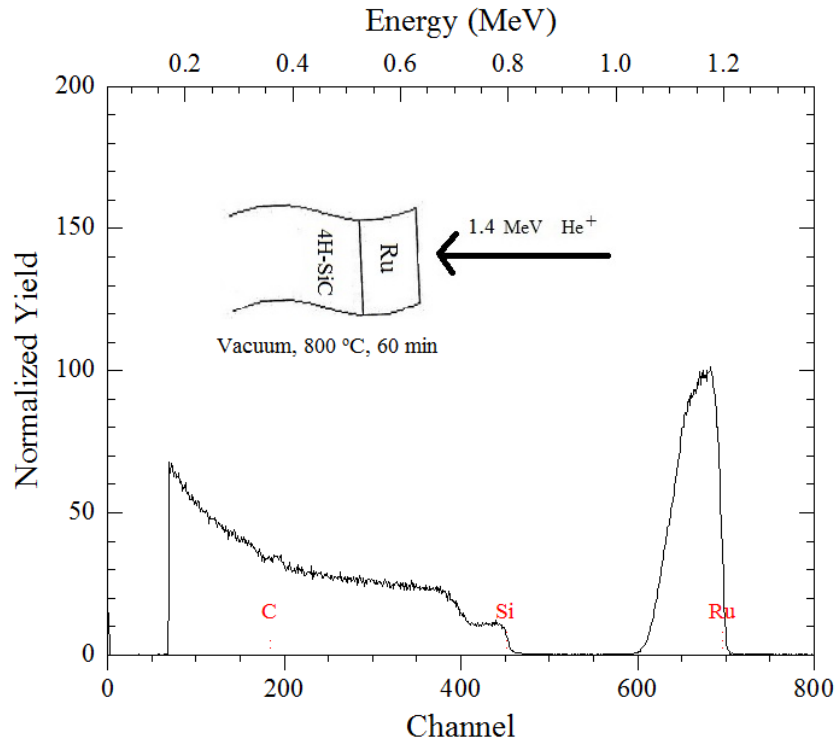
Fig. 4.30. RBS spectrum of Ru/4H-SiC film annealed in a vacuum at 800 °C. The spectrum shows the formation of a silicide as indicated by a step on the high energy edge of Si.

Fig.4.31. Raman spectra for Ru/4H-SiC annealed in vacuum at 1000 ºC. The spectrum indicates the presence of graphite flakes as evidenced by D and G peaks at 1354 cm^{-1} and 1589 cm^{-1} respectively. Ruthenium silicide is also indicated by a peak slightly to the left of position 300 cm^{-1}.

The as-deposited RBS spectrum of Ru/6H-SiC (not shown) is similar to the sample annealed at 500 ºC in a vacuum (Fig. 4.32). There is an indication of silicide formation at 600 ºC as evidenced by the presence of a step near the high energy step of Si (Fig.4.33). Diffusion of Ru into SiC commences at 800 ºC (not shown) and is more pronounced at 900 ºC as indicated by a very wide base of Ru signal (Fig.4.34). The silicide formation is more pronounced at an annealing temperature of 1000 ºC as indicated by steps on the high energy edge of Si and low energy edge of Ru (Fig.4.35). There is increased accumulation of carbon at the surface at 900 ºC and 1000 ºC as indicated by pronounced carbon peaks at channel number 180

(Fig.4.34 and Fig.4.35). This carbon is released from the formation of ruthenium silicide. Plots of depth profiles (Fig.4.36 and Fig. 4.37) have been obtained from RUMP [1] simulations. From these simulations, it is observed that Ru diffuses into 6H-SiC, and the dissociated Si and C

atoms also diffuse into Ru. The reaction zone increases with increasing annealing temperature. The Ru/6H-SiC interface of the as-deposited sample (Fig.4.41) is located 320x 10^{15} at./cm^2 from the surface of Ru. Ru is observed to react with 6H-SiC and is found at 2300 x 10^{15} at./cm^2 from the surface (Fig.4.37) after annealing at 1000°C.

Raman spectrum of Ru/6H-SiC thin films annealed in a vacuum at 1000 °C (Fig. 4.38) clearly indicates the formation of graphitic structures as evidenced by the D and G carbon peaks at 1356 cm^{-1} and 1589 cm^{-1} respectively [13-16].
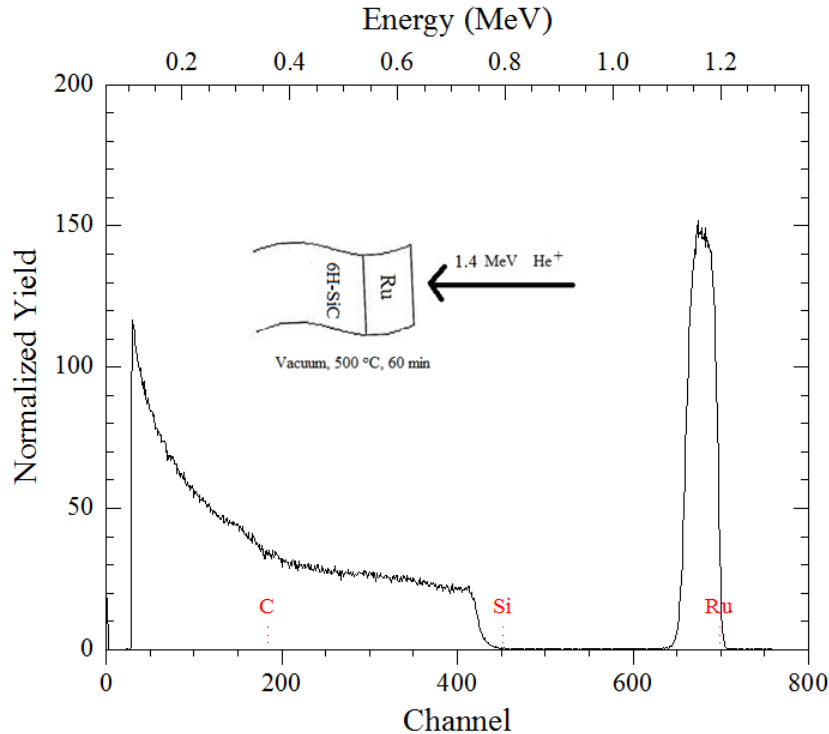
Fig 4.32. RBS spectra of Ru/6H-SiC annealed in a vacuum at 500°C obtained by using 1.4 MeV of helium ions. The spectrum shows the presence of pure Ru on the surface of 6H-SiC.
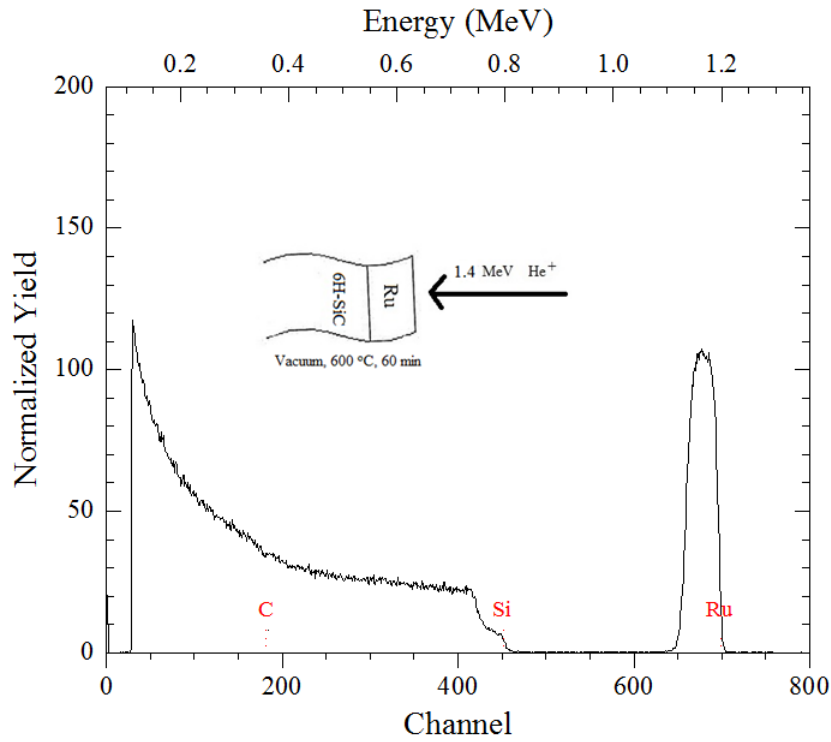
Fig 4.33. RBS spectra of Ru/6H-SiC annealed in a vacuum at 600°C obtained by using 1.4 MeV of helium ions. The spectrum shows the formation of ruthenium silicide as indicated by the step on the high energy edge of Si.
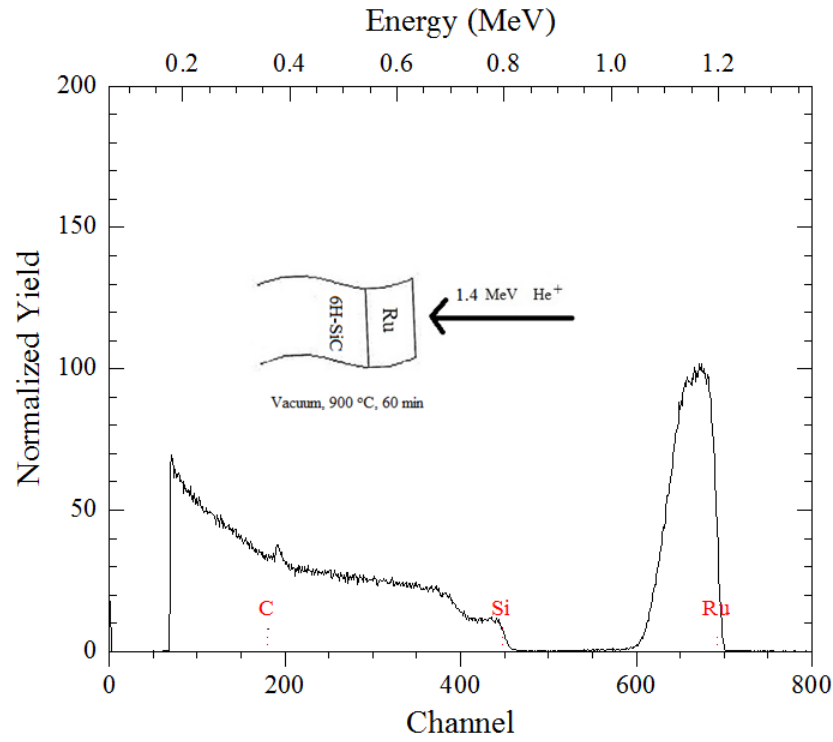
Fig.4.34. RBS spectra of Ru/6H-SiC annealed in a vacuum at 900ºC obtained by using 1.4 MeV of helium ions. The spectrum shows accumulation of carbon at the surface, as evidenced by a pronounced carbon peak, and silicide formation as indicated by the step on the high energy edge of Si. Ru diffusion into 4H-SiC is indicated by the widening of the base and height reduction of the Ru signal.
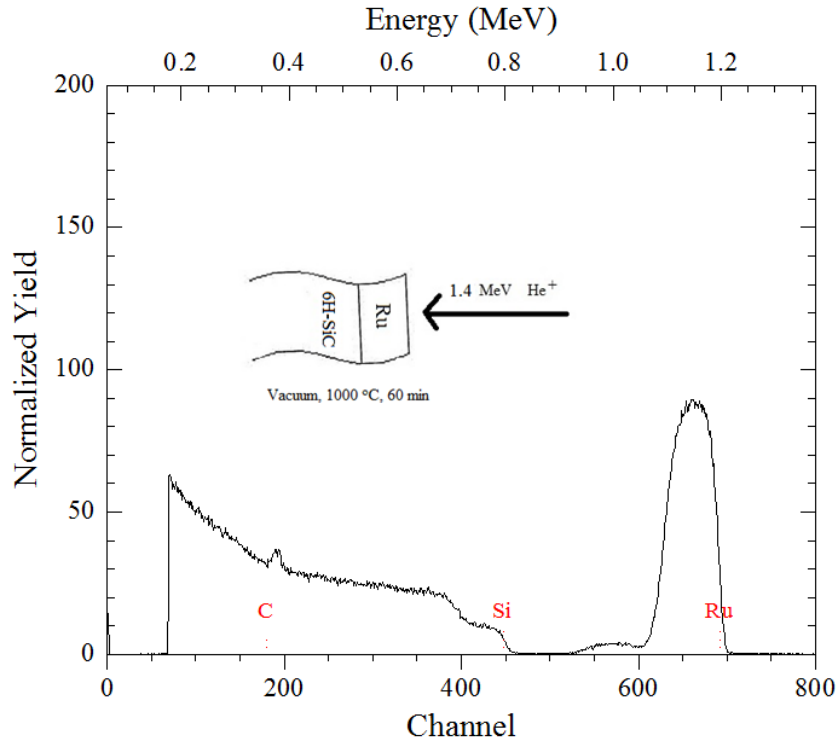
Fig.4.35. RBS spectra of Ru/6H-SiC annealed in a vacuum at 1000ºC obtained by using 1.4 MeV of helium ions. Silicide formation is indicated by the steps on the lower energy edge of Ru and high energy edge of Si. Carbon accumulation at the surface is indicated by a pronounced carbon peak.
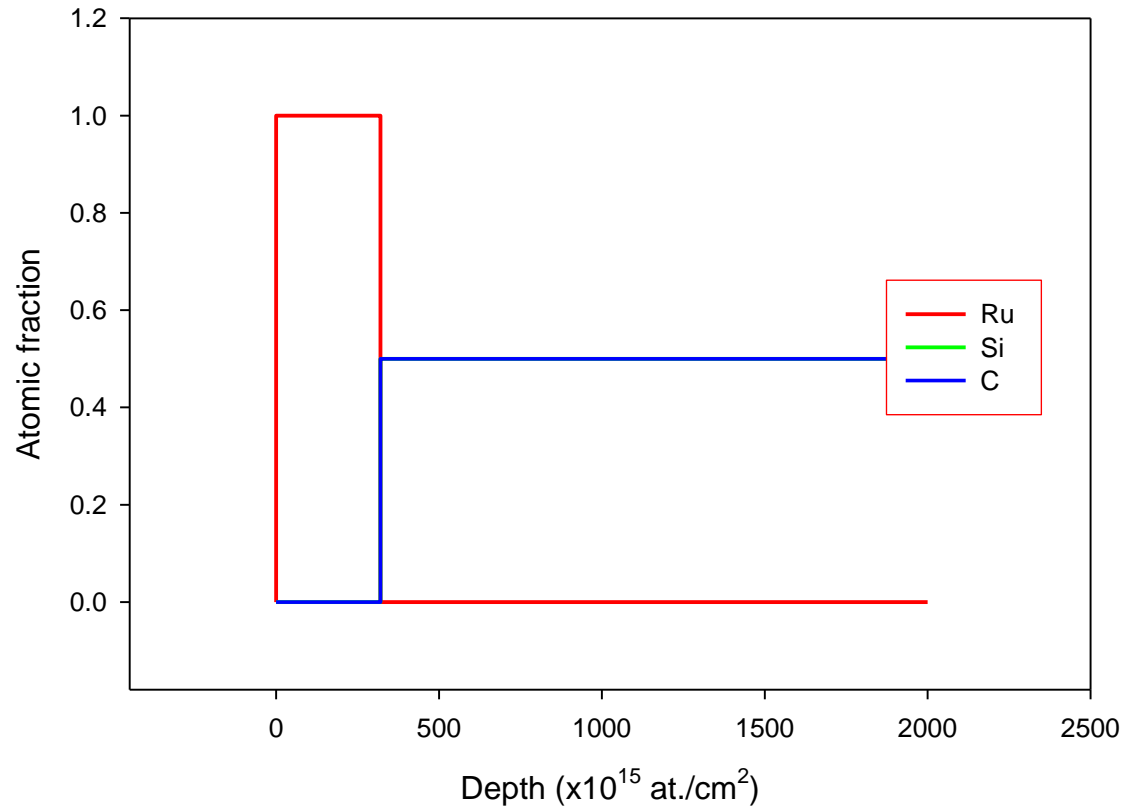
Fig. 4.36. Depth profile of as-deposited Ru/6H-SiC. The profile shows the presence of a pure Ru on 6H-SiC.
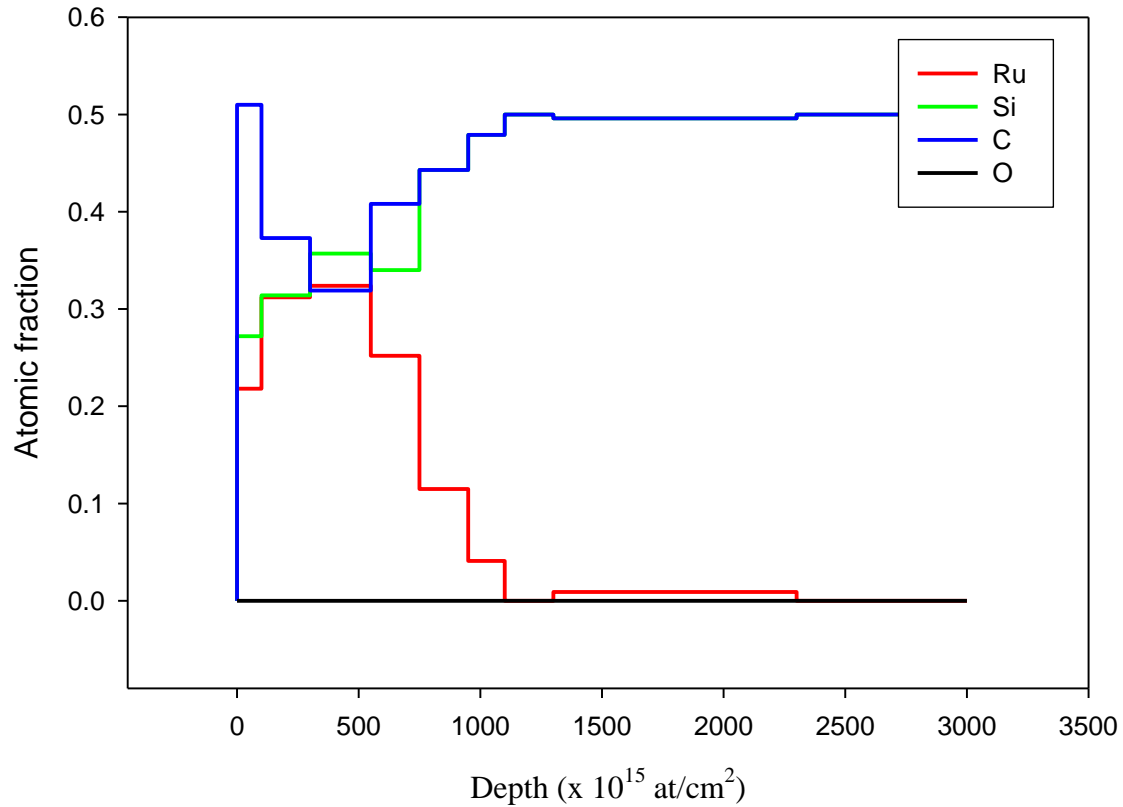
Fig. 4.37. Depth profile of Ru/6H-SiC annealed at 1000 °C in a vacuum. The profile shows the interdiffusion of Ru, Si, and C at the interface.
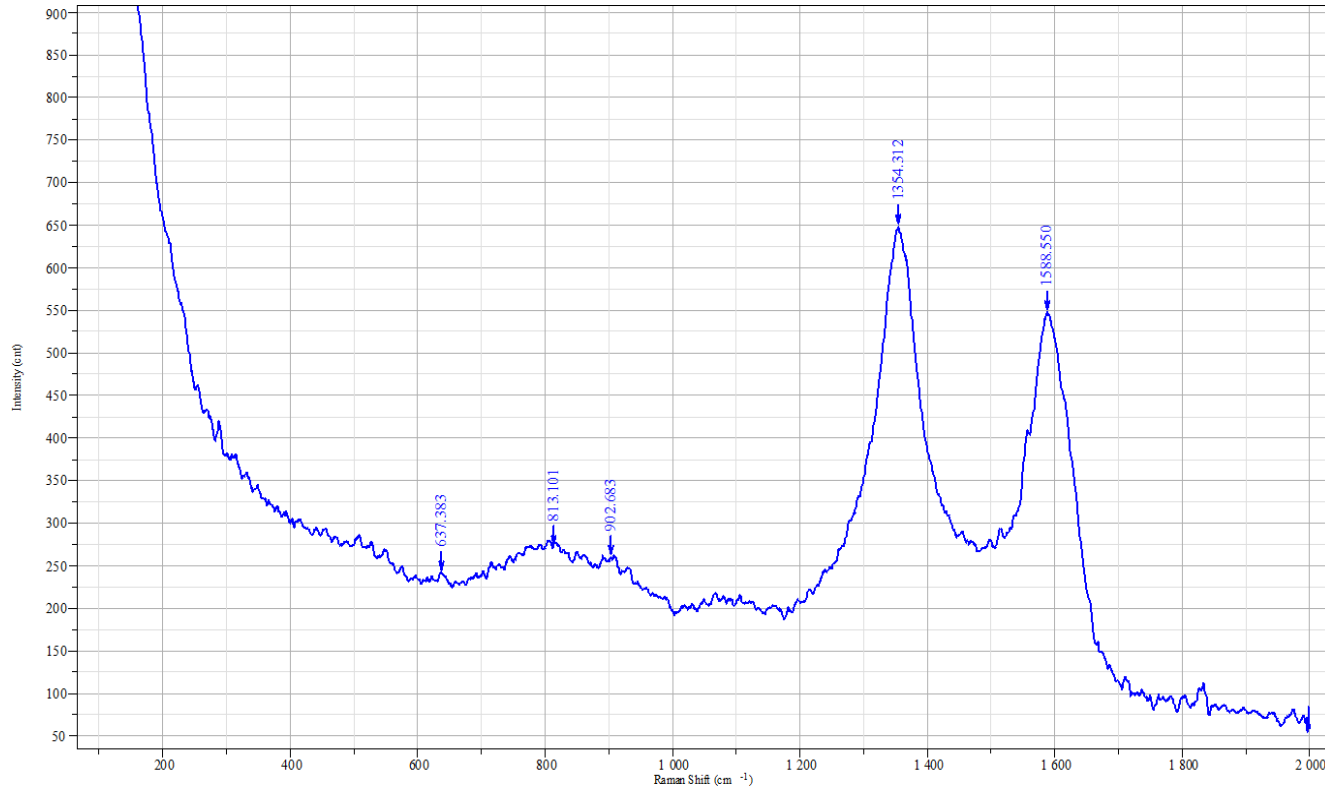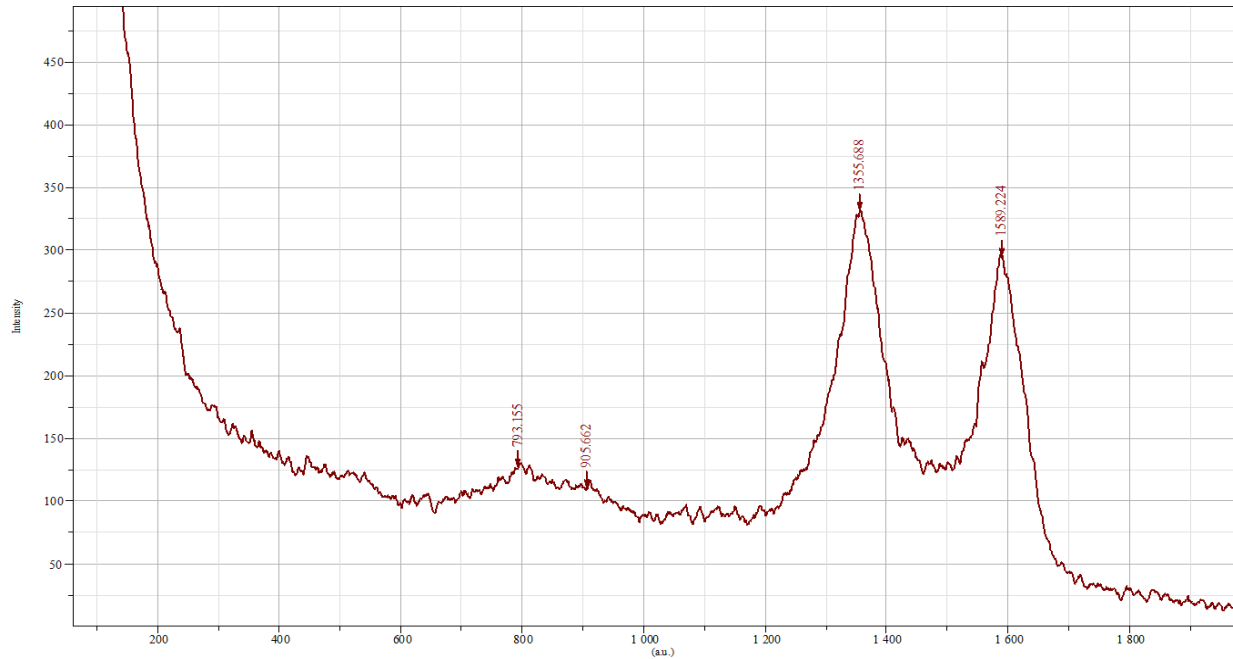
Fig 4.38. Raman spectrum of Ru/6H-SiC film annealed in vacuum at 1000 °C. The spectrum shows the formation of graphite flakes as evidenced by D and G peaks at 1356 cm^{-1} and 1589 cm^{-1} respectively.

4.3 Discussion

This investigation has shown that there is diffusion of Ru into 4H-SiC and 6H-SiC under vacuum, air, and argon annealing. Under argon annealing, Ru diffusion in 6H-SiC starts at a higher temperature compared to its diffusion in 4H-SiC. Diffusion of Ru starts at a much lower temperature for both SiC polytypes under air annealing as compared with vacuum annealing. The results have also shown that Ru interfaces on both SiC polytypes undergo silicidation in air, argon (except for Ru/6H-SiC) and vacuum annealing environments and that there is a formation of ruthenium oxide under air and argon annealing.

Let us discuss the implications of these results on the effectiveness of SiC as a containment layer of fission products in TRISO coated nuclear fuel particles. From these findings, we can conclude that in TRISO coated fuel particles, where actinide oxide fuels are used and oxygen is released in the fission reaction [20], there will be oxidation of Ru as has been demonstrated by the air annealing of Ru-SiC thin films in this investigation. Ru

penetration into the SiC substrate has also been verified by RBS analysis of thin films of Ru/SiC annealed in the air, argon and vacuum. This confirms that the SiC layer is not effective in containing metal fission products in TRISO particles. However, before we get carried away, there is a need to outline the differences between this investigation experimental-set-up and the actual burn-up process of TRISO particles.

In general, the results in the previous section have provided some important information on Ru-SiC interface behaviour at different temperatures and in different annealing environments. The results shed more light on the ineffectiveness of SiC as a diffusion barrier to fission products in TRISO particles. However, there are some differences between this diffusion study experiment and the actual process of burn-up in TRISO particles in nuclear reactors. In TRISO particles, the concentration of Ru on the SiC surface is likely to be lower than in this thin film experiment, and consequently, the reaction penetration depth into SiC should be lower as well. The reasoning behind this assession is that in TRISO particles burn-up process, Ru with other elements which are released have to pass through layers of carbon before reaching the SiC layer. This means that not all the Ru that is released in the burn-up process will reach the SiC layer. Experiments have shown that the rate-limiting step in fission product palladium (Pd) attack on SiC depends on the supply of Pd from the kernel and the rate of diffusion of Pd through the buffer and inner PyC layer [21]. According to Sawa *et al* [21], studies of the interaction of Pd with SiC have shown that the maximum reaction depth will depend on the amount of Pd released from the kernels. The penetration depth has been shown to be directly proportional to the cube root of the concentration of Pd. The maximum penetration depth for the fuel lifetime has been calculated to be 11 μm which is less than half of the SiC layer thickness of 35 μm [22] in TRISO particles. Since Ru just like Pd belongs to the platinum metal group and has similar chemical and physical characteristics, the expectation is that its diffusion depth should closely mirror that of Pd.

The other difference between the thin film experiments in this study and TRISO particles is that during burn-up of TRISO particles, extreme pressure is created in the coated fuel particle due to the formation of fission gases such as xenon and krypton. The amount of fission gases released from the kernel of a TRISO particle depends on temperature, burnup, and time [23]. Experiments have shown that as burn-up increases, there is a concomitant increase in pressure and temperature in the fuel particle. Metallic fission product release is usually modeled by Fickian diffusion with Arrhenius diffusion coefficients, and from this modeling, diffusion is shown to be a function of time and temperature. From this information, we can conclude that extreme pressure will increase the rate of diffusion of fission metals. In this investigation, the thin films were not subjected to extreme pressure. The samples were only subjected to high temperatures especially those under vacuum and argon annealing environments.

In UO_2 fuel particles, the fission reaction produces a net excess of free oxygen as the fission products that are produced do not consume all the oxygen that is released [23]. This is due to the fact that the thermo-chemical conditions are unfavourable for these fission metals to form stable oxides [24].This excess oxygen reacts with the buffer to form CO gas which greatly increases the internal pressure in the particle. This CO may break into the PyC layer and then react with SiC to form SiO. The breaking of the PyC layer by CO will enhance the diffusion of fission metal

products such as Ru which will react with SiC as well as oxygen. Londono-Hurtado *et al* [25] in their paper argued that there is a possibility of the introduction of defects in the SiC crystal through the incorporation of the fission product Ru and oxygen into the crystal under some favourable oxygen partial pressure. The introduction of the defects will increase the diffusion of the fission metal product through the crystal. The behaviour of Ru-SiC annealed in air in this study directly mirrors this situation. This investigation has shown that diffusion of Ru into SiC starts at a much lower temperature in air annealing as compared to vacuum annealing.

The SiC layer in TRISO particles is commonly deposited by a chemical-vapour-deposition (CVD) process, and the resulting SiC is the 3C-SiC. The physical and chemical properties of 3C-SiC are very similar to those of 4H-SiC and 6H-SiC used in this investigation. The only difference among these three SiC polytypes is the arrangement of the Si-C atomic planes as explained in Chapter 2. Therefore, the findings from air and vacuum annealing of Ru-SiC thin films obtained in this study are very much applicable to the CVD SiC used in TRISO fuel particles. Furthermore, studies have shown that 3C-SiC transforms to hexagonal SiC (α-SiC) at temperatures between 1600 ^{o}C to 2000 ^{o}C [24]. Some high-temperature-gas-cooled reactors (HTGR) operate at temperatures of around 950 ^{o}C [23], therefore, the results of this investigation will be directly applicable to such reactors. Furthermore, from having a fore-knowledge that diffusion of fission products is a function of time and temperature, and having established in this study that there is Ru diffusion in SiC beginning from a low temperatures of 400 ^{o}C and 500 ^{o}C in the air and vacuum respectively, and up to a maximum annealing temperature of 1000 ^{o}C in very low annealing times of 15 minutes and 1 h, the extrapolation is that there will be increased diffusion if the temperatures were increased above 1000 ^{o}C and the annealing time increased to more than 1 year as normally happens in actual irradiation in high-temperature nuclear reactors.

From Raman analysis of the Ru-SiC samples annealed in a vacuum at 1000 ^{o}C, it has been shown that graphite structures are formed during the annealing process. Annealing for longer periods results in the formation of graphene. Graphene has interesting electronic properties which find applications in the miniaturisation of electronic devices in nano-electronics. Even though this was not the main aim of the investigation, the possibility of producing graphene through a vacuum annealing process of Ru-SiC can be further explored so as to produce commercially viable amounts of this interesting product.

Having shown in this study that the SiC layer is ineffective as a fission product containment layer, it is necessary to explore other ceramic compounds, such as zirconium carbide, to replace the SiC layer in TRISO coated fuel particles.

Ru diffusion, phase transformation and solid state reactions at the Ru-SiC interface and their implications on the performance of Ru-SiC Schottky diodes will be dealt with in the next chapter.

4.4 Conclusion

This study has shown that there is solid state diffusion of Ru in both 4H-SiC and 6H-SiC thereby showing that SiC is not a perfect barrier to metal fission products in TRISO coated fuel particles. Diffusion of Ru into SiC has been shown to start at a lower temperature in the air annealing environment compared to argon and vacuum annealing environments. Silicides and oxides of ruthenium (in argon and air annealing) are also produced during the annealing process. These interface processes have a direct bearing on the electrical performance of Ru/SiC based Schottky barrier diodes which will be explained in detail in the next chapter.

4.5 Reference

[1] L.R. Dolittle, *Algorithms for the rapid simulation of Rutherford backscattering spectra*, Nuclear Instruments and Methods in Physics Research Section B: Beam Interactions with Materials and Atoms, Volume 9, Issue 3, pp 344-351, (1985).

[2] S. Roy, C. Jacob, M.Zhang, S. Wang, A.K. Tyagi, S. Basu, *SIMS, RBS and glancing incidence X-ray diffraction studies of thermally annealed Ru/β-SiC interfaces*, Applied Surface Science **211** 300–307, (2003).

[3] E.V. Jelenkovic, K.Y. Tong, *Thermally grown ruthenium oxide thin films*, Journal of Vacuum Science Technology B 22(5), (2004).

[4] M.M. Steeves, Electronic transport properties of ruthenium and ruthenium oxide thin films, A Ph.D. thesis, University of Maine (unpublished results).

[5] A.G. Birdwell, Optical properties of β-FeSi$_2$, Ru2Si$_3$, and OsSi$_2$: semiconducting silicides, Ph.D. Thesis, The University of Texas at Dallas, (2009).

[6] M. Chafai, A. Jaouhari, A. Torres, R. Anton, E. Martin, J. Jimenez, W.C. Mitchel, *Raman scattering from LO phonon-plasmon coupled modes and Hall-effect in n-type silicon carbide 4H-SiC*, Journal of Applied Physics, vol 90, Number 10, (2001).

[7] S.K. Kannan, M. Sundrarajan, Green synthesis of ruthenium oxide nanoparticles: Characterization and its antibacterial activity, Advanced Powder Technology, Vol. 26, Issue 6, pp. 1505-1511, (2015)

[8] J. Ahn, W. Choi, W. Lee, H. Kim, *Annealing of RuO2 and Ru bottom electrodes and its effect on the electrical properties of (Ba, Sr)TiO$_3$ thin films*, Japanese Journal of Applied Physics, vol. 37, pp 284-289, (1998).

[9]] A. Perez-Rodriguez, Y. Pacud, L. Calvo-Barrio, C. Serre, W. Skorupa, J.R. Morante, *Analysis of ion beam induced damage and amorphization of 6H-SiC by Raman scattering,* Journal of Electronic Materials, Vol. 25, No.3, (1996).

[10] W. Lu, W.C. Mitchel, C.A. Thornton, G.R. Landis, W.E. Collins, *Carbon structural transitions and ohmic contacts on 4H-SiC,* Journal of Electronic Materials, Vol. 32, No.5, (2003).

[11] H.Y.H. Chan, C.G. Takoudis, M.J. Weaver, *High-Pressure Oxidation of Ruthenium as Probed by Surface-Enhanced Raman and X-Ray Photoelectron Spectroscopies,* Journal of Catalysis, Volume 172, Issue 2, Pages 336–345, (1997).

[12] J. Musschoot, Q. Xie, D. Deduytsche, K. De Keyser, D. Longrie, J. Haemers, S. Van den Berghe, R.L. Van Meirhaeghe, J. D'Haen, C. Detavernier, *Texture of atomic layer deposited ruthenium,* Microelectronic Engineering 87, 1879–1883, (2010).

[13] Zhen-Yu Juang, Chih-Yu Wu, Chien-Wei Lo, Wei-Yu Chen, Chih-Fang Huang, Jenn-Chang Hwang, Fu-Rong Chen, Keh-Chyang Leou, Chuen-Horng Tsai, *Synthesis of graphene on silicon carbide substrates at low temperature*, Carbon vol 47, 2026 –2031, (2009).

[14] V. Mennella, G. Monaco, L. Colangeli, E. Bussoletti, *Raman spectra of carbon-based materials excited at 1064 nm*, Carbon vol 33, No. 2, pp 115-121, (1995).

[15] H. Hiura, T.W. Ebbesen, K. Tanigaki, *Raman studies of carbon nanotubes*, Chemical Physics Letters vol 202, number 6, (1993).

[16] P.C. Eklund, J.M. Holden, R.A. Jishi, *Vibrational modes of carbon nanotubes; Spectroscopy and Theory*, Carbon vol. 33, No. 7 pp. 959-972, (1995).

[17] S. Nakashima, Y. Nakatake, H. Harima, M. Katsuno, N. Ohtani, *Detection of stacking faults in 6H-SiC by Raman scattering*, Applied Physics Letters, Vol. 77, No.22, (2000).

[18] M. Wieligor, Y. Wang, T.W. Zerda, *Raman spectra of silicon carbide small particles and nanowires*, Journal of Physics: Condensed Matter, 17, 2387-2395, (2005).

[19] E.V. Jelenkovic, K.Y. Tong, W.Y. Cheung, S.P. Wong, *Physical and electrical properties of sputtered Ru2Si3/Si structures*, Semiconductor Science Technology, 18, 454-459, (2003).

[20] T.M. Besmann, R.E. Stoller, G. Samolyuk, P.C. Schuck, S.I. Golubov, S.P. Rudin, J.M. Wills, J.D. Coe, B.D. Wirth, S. Kim, D.D. Morgan, I. Szlufarska, *Modeling Deep Burn TRISO particle nuclear fuel*, Journal of Nuclear Materials 430 181-189, (2012).

[21] K. Sawa, S. Ueta, *Research and development on HTGR fuel in the HTTR project*, Nuclear Engineering and Design 233, 163-172, (2004).

[22] G.K. Miller, D.A. Petti, J.T. Maki, D.L. Knudson, *An evaluation of the effects of SiC layer thinning on failure of TRISO-coated fuel particles,* Journal of Nuclear Materials, Volume 355, Issues 1-3, 150–162, (2006).

[23] J.T. Maki, D.A. Petti, D.A. Knudson, G.K. Miller, *The challenges associated with high burnup, high temperature and accelerated irradiation for TRISO-coated particle fuel,* Journal of Nuclear Materials 371, 270-280, (2007).

[24] X.W. Zhou, C.H. Tang, *Current status and future development of coated fuel particles for high temperature gas-cooled reactors,* Progress in Nuclear Energy 53 182-188, (2011).

[25] A. Londono-Hurtado, A.J. Heim, S. Kim, I. Szlufarska, D. Morgan, *Cs and Ag co-incorporation in cubic silicon carbide,* Journal of Nuclear Materials 439, 65-71, (2013).

CHAPTER 5

RESULTS OF OPERATIONAL INTEGRITY OF RUTHENIUM-SiC SCHOTTKY BARRIER DIODES ANNEALED IN THE AIR, ARGON AND A VACUUM.

5.1 Introduction

SiC has a number of polytypes, but 4H-SiC and 6H-SiC are the two main polytypes which are commonly used for fabricating devices owing to the fact that they can be produced with very low micropipe densities. Ru properties of high melting point (2250° C), high chemical stability, low electrical resistance, and high mechanical resistance to abrasion and fatigue [1, 2] make it a suitable candidate for Schottky contacts for high temperature operating SBDs. However, there has been limited literature [1-7] on the comparative analysis of solid state reaction, electrical performance and failure mechanism of Ru Schottky contacts on 6H-SiC and 4H-SiC at various annealing temperatures as previously discussed in chapter 1.

To investigate solid state reaction and microstructure evolution of the Schottky contact, thin films of Ru on 6H-SiC and 4H-SiC were analysed with RBS, Raman spectroscopy, and XRD technique after various annealing temperatures as outlined in the preceding chapter. In order to gauge the electrical performance of the SBDs, electrical parameters of SBH, ideality factor, saturation current, and series resistance were extracted from IV and CV characteristics of Ru/6H-SiC and Ru/4H-SiC SBDs (with nickel back ohmic contacts) after various air annealing temperatures.

5.2 Experimental Method

N-type-bulk grown 6H-SiC and n-type 4H-SiC with an epilayer from Cree Research were prepared for metallization by degreasing, using an ultra-sonic bath for a period of 5 minutes for each step, in trichloroethylene, acetone, methanol, and deoxidizing 10% HF. The samples were finally rinsed with deionised water and then dried with nitrogen before loading them into the vacuum chamber where 200nm of nickel (Ni) was deposited on the rough surface of both samples by vacuum resistive evaporation. The samples were then annealed in an argon atmosphere in a Lindberg Heviduty furnace at a temperature of $950^{o}C$ for 1 minute to make the contact ohmic. The annealed samples were then chemically cleaned again in trichloroethylene, acetone, and methanol, and deionised water before a 50 nm thick of Ru was deposited on the polished surface of both samples by e-beam through a metal contact mask at 10^{-6} mbar pressure. The Ru film thickness was monitored by Infincon meter until the required thickness was obtained. Dots of Schottky contacts of diameter 0.6mm were fabricated.

The Ru-4H-SiC and Ru-6H-SiC Schottky diodes were annealed in the air and argon environment by using a Lindberg Heviduty furnace for a period of 15 minutes at various temperatures. The third set of samples was also annealed in a vacuum for a period of 60 minutes at various temperatures. Full IV and CV characterisation of the diodes were performed at an ambient temperature of 24 ^{o}C after each annealing process using 4140B pA meter /DC voltage source by Hewlett Packard which was interfaced to a LabVIEW operated computer. The CV measurements were done at a frequency of 1MHz. Both the IV and CV measurement data were automatically saved on the computer by LabVIEW. For all the samples CV and IV measurements were made on one dot of contact.

5.3. Experimental results for Ru/4H-SiC Schottky barrier diodes annealed in the air.

5.3.1 Experimental Results and Discussion

The Ru-4H-SiC Schottky diodes were evaluated using IV and CV characteristics. The SBH, ideality factor and saturation current were obtained from IV characteristics by assuming that the Schottky diodes obeyed the thermionic emission current transport model given by equation 2.14 in

chapter 2. From this equation, a plot of ln J versus voltage V will give a straight line graph whose slope will be equal to $\frac{q}{\eta kT}$ where the ideality η can be extracted. The intercept of the graph will give the saturation current density J_s which can then be used to extract the barrier height ϕ_{Bn}.

Series resistance R_s is the resistance of the bulk material of the semiconductor plus that of the back ohmic contact, and to account for the series resistance, the modified current-voltage equation given by equation 2.16 in chapter 2 is used. The parameters from CV characteristics are obtained from the junction capacitance of the SBD which is given by equation 2.26 in Chapter 2. From this equation, a plot of $\frac{1}{C^2}$ versus V will give a straight line, and a donor doping density N_D can be extracted from the graph. The SBH is determined from the voltage intercept [8] by the equation $\phi_{Bn} = V_i + V_O$, where V_i is the voltage intercept and V_O is given by equation 2.28 in chapter 2.

The parameters that were extracted after annealing the Ru-4H-SiC SBDs in the air are displayed in Table 1.

Table 1. Parameters of Ru/4H-SiC SBDs annealed in air.

*The SBDs temperature as high series -The computer did values.

Annealing Temp	Ideality factor η	SBH from IV (eV)	SBH from CV (eV)	Series Resistance R_s (Ω)	Saturation Current I_S (A)	Donor Density N_D (cm^{-3})	Reverse Current (A) at -2V
As dep	2.636	0.95	2.38	20	2.1x10^{-12}	9.68x10^{15}	3.29x10^{-13}
300ºC	1.399	1.44	2.27	17	1.4x10^{-20}	9.56x10^{15}	2.96x10^{-13}
400ºC*	1.341	1.27	2.31	9207	1.1x10^{-17}	8.38x10^{15}	-
500ºC	1.372	1.25	2.40	19266	2.1x10^{-17}	8.30x10^{15}	-

breakdown at this indicated by a very resistance. not record these

From Table 1, it is observed that the Ru/4H-SiC SBDs degrade at a surprisingly low annealing temperature of 400 ºC as demonstrated by the extremely large series resistance. RBS analysis of Ru/4H-SiC thin film reveals that oxidation of Ru begins at this annealing temperature. The extremely large series resistance is attributed to the formation of oxide compounds that are not semiconducting oxides such as RuO, low temperature melting RuO$_4$ or RuO$_3$, and Ru$_2$O$_3$ as previously explained in chapter 4. The SBHs obtained from CV characteristics were slightly higher than those from IV characteristics. Normally SBH obtained from CV measurements are slightly higher than those obtained from IV characteristics due to the fact that there might be an additional capacitance at the metal-semiconductor interface due to the presence of a thin oxide which comes as a result of surface preparation[9]. The variation of SBH as observed in the table may be attributed to the presence of an inhomogeneous barrier at the metal-semiconductor interface. The existence of inhomogeneous interfaces

results in non-uniform Schottky contacts where current can flow via two pathways (i.e. over a lower barrier or a higher barrier) [10]. According to Osvald *et al* [9], SBH inhomogeneity may be due to the fact that there are different crystallographic orientations of the grains in the polycrystalline structure of the metallic layer and also there is a possibility that the phase composition of the interface materials may change after annealing. The changes in the phase composition of the interface materials have been confirmed by RBS, Raman and XRD analyses as discussed in Chapter 4. Another observation from Table 1 is that the saturation current decreases in size when the SBD is annealed at 300 °C. These findings are in agreement with those of Sochacki *et al* [11] who also found a decrease in saturation current for Ni-SiC Schottky diodes when annealed in an argon and hydrogen mixture. The authors argue that defects in the interface between metal and semiconductor, which are generated near the semiconductor surface when the metal contact is deposited on this surface, heavily influence the reverse current of the diode. Annealing reduces these defects which result in the reduction of the saturation current as observed in this investigation.

The exponential shape of IV characteristics(not shown) and the linear nature of log IV (in some areas) and CV characteristics (Fig. 5.1, and Fig. 5.2) are indications of the thermal stability of the SBDs just before they breakdown. The best fit line was drawn for the as-deposited sample because of the instability of the measuring instrument. The donor densities N_D for the Ru/4H-SiC SBDs which have been extracted from the CV characteristics are in close agreement with donor density specification of $1.16 \times 10^{16} \, \text{cm}^{-3}$ given by Cree Research Inc. Even though the free carrier densities for 4H-SiC agree with that given by the manufacturer, they are not constant at different annealing temperatures. The net doping concentration that is obtained from CV characterisation is the difference of the electrically active concentration of donors and acceptors. If there is leakage current in the Schottky contacts, there is a disturbance in the capacitance measurements and, therefore, errors in the estimation of the net doping concentration arise [12]. This leads to non-constant values of free carrier densities.

Another reason for this variation might be due to the variation of the series resistance. According to Frojdh C *et al* [13], a resistance in series with a capacitor makes the measured value of capacitance to decrease. From this assertion, an increase in series resistance will lead to a decrease in the capacitance measured. Rearranging equation 2.26 in chapter 2 we get

$$N_D = \frac{2(V_{bi} - V)C^2}{q\varepsilon_s} \tag{5.1}$$

Comparing the values of series resistance and donor density in Table 1, and then linking the values with equation 5.1, one should observe that for high values of resistance, the capacitance measured will be low and, therefore, N_D values extracted from the equation should be low as well. The data in Table 1 largely agrees with this view.
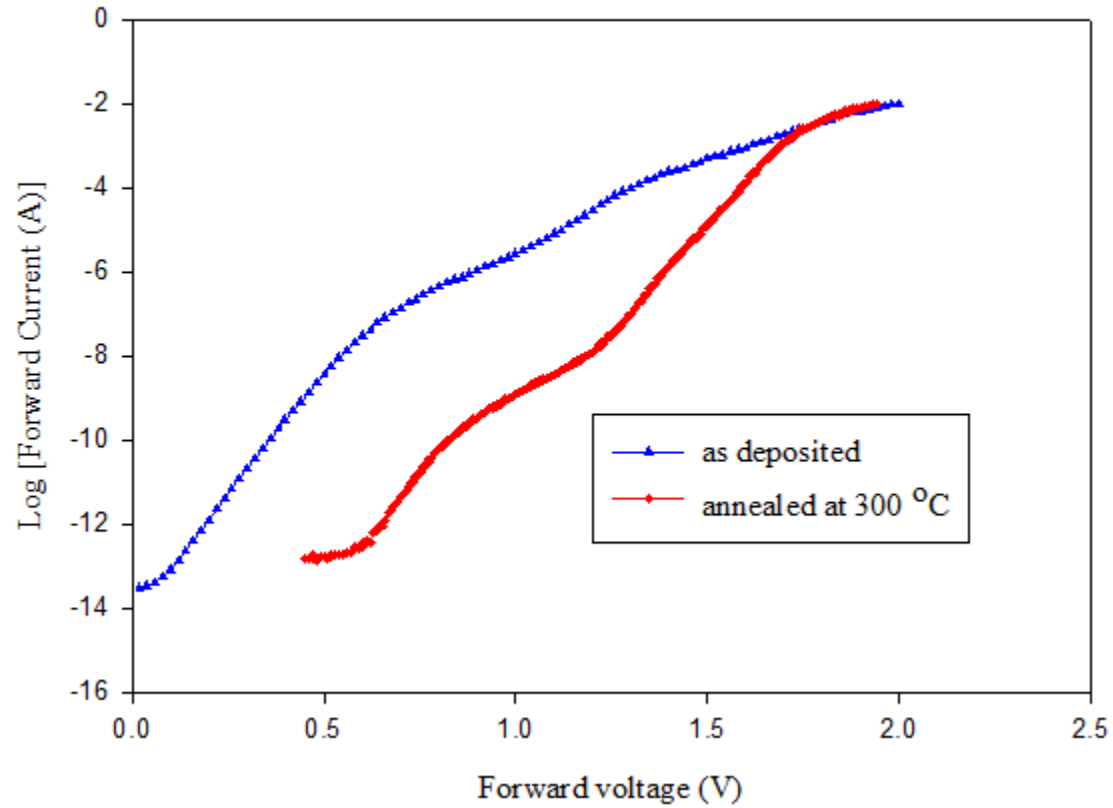
Fig. 5.1. Log IV characteristics of Ru/4H-SiC SBDs annealed in air.
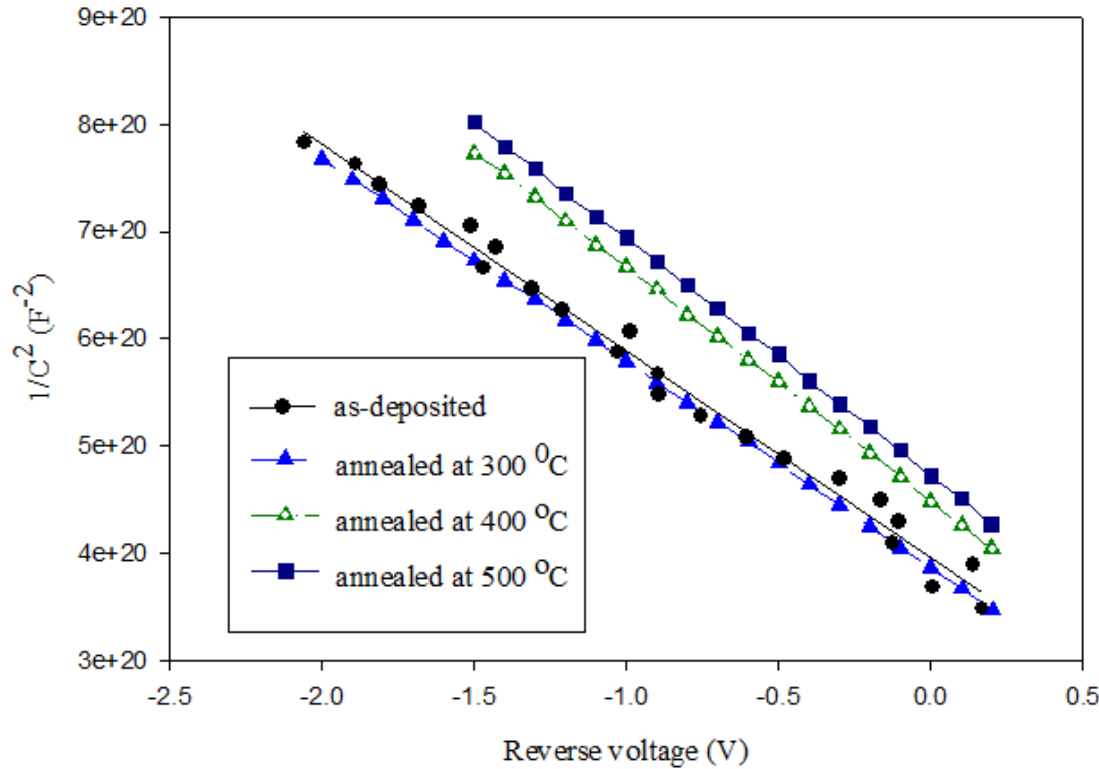
Fig. 5.2. CV characteristics of Ru/4H-SiC SBDs annealed in air.

5.3.2 Conclusion

This study has shown that Ru/4H-SiC SBDs after annealing in air exhibit operational stability after annealing temperatures of up to 300 °C and degrade above this temperature as evidenced by the extremely high series resistance. The cause of degradation of the Ru/4H-SiC SBDs might be the silicidation and oxidation of Ru to form a non-conducting oxides and slicides as indicated by Raman and XRD analyses. The investigation has also shown that annealing causes diffusion and phase transformation at the Schottky-substrate interface.

5.4. Experimental results for Ru/6H-SiC Schottky barrier diodes annealed in the air.

5.4.1 Experimental Results and Discussion

The various parameters of the Ru/6H-SiC SBDs were extracted from the IV and CV data as explained in section 5.3.1. Table 2 is a collection of parameters that were extracted.

Table 2. Parameters of Ru-6H-SiC SBDs annealed in air.

Annealing Temperature	Ideality factor η	SBH From IV (eV)	SBH From CV (eV)	Series Resistance R_s (Ω)	Saturation Current I_S (A)	Donor Density N_D (cm^{-3})	Reverse Current (A) at -2V
As dep	2.062	0.74	0.73	250	8.6×10^{-9}	2.55×10^{18}	1.06×10^{-5}
100ºC	1.470	0.79	0.59	76	1.5×10^{-9}	2.42×10^{18}	2.93×10^{-5}
200ºC	1.596	0.70	0.65	88	5.3×10^{-8}	2.95×10^{18}	5.81×10^{-5}
300ºC	1.495	0.88	0.76	131	3.8×10^{-11}	2.47×10^{18}	2.2×10^{-7}
400ºC	1.764	0.72	0.66	80	2.5×10^{-8}	2.23×10^{18}	2.02×10^{-5}
500ºC	1.318	0.62	0.85	67	1.2×10^{-6}	2.59×10^{18}	-
600ºC	1.612	0.84	0.69	85	2.1×10^{-10}	2.74×10^{18}	7.02×10^{-6}
700ºC*	2.120	0.97	25.77	222465	1.5×10^{-12}	9.24×10^{16}	1.1×10^{-7}

*The SBDs breakdown at this temperature as evidenced by a high series resistance and awkward value of SBH obtained from CV characteristics.

From Table 2, it can be seen that the ideality factor for the as-deposited Ru/6H-SiC SBD is very high, but generally decreases as the annealing temperature is increased (with the exception of degradation temperature of 700ºC). These findings are in agreement with Buc *et al* [3] who also found that the ideality factor of RuO$_2$ Schottky contacts on SiC decreased with increasing annealing temperature. Annealing, therefore, improves the performance of the Schottky diode. Even though the ideality factors found in this investigation agree with those in literature, they are not unity. This means current conduction in the diode is not only thermionic, but other modes of conduction such as recombination current or tunneling effect are available as well. It is also observed that the SBH does not change much with annealing temperature. Furthermore, the difference between SBHs obtained through CV and IV characteristics are so small as to be negligible. Another observation from Table 2 is that the series resistance generally decreases with increasing annealing temperature before the degradation of the diode. One possible explanation for the decrease in series resistance with annealing temperature is that annealing makes the Schottky metal contact to be more intimate with the semiconductor substrate. The formation of RuO$_2$ at the surface of Ru as observed from Raman, XRD and RBS analyses and the interdiffusion of Ru and Si at the Ru/6H-SiC interface did not lead to dramatic changes in SBH, ideality factor and other parameters of the SBD below annealing temperature of 700 ºC. One possible explanation of the small variation of SBH after the formation of RuO$_2$ is that the SBHs of Ru and RuO$_2$ on SiC are nearly equal to each other [14]. At an annealing temperature of 700 ºC, the series

resistance astronomically increases to a very large value which basically indicates that the SBD has degraded. The degradation of the Ru Schottky contact can be explained by the fact that at this annealing temperature there are indications from the RBS spectra of deep inter-diffusions of Ru and Si at the Ru/6H-SiC interface, and there is also a possibility of oxidation of Ru to form gaseous RuO and low temperature melting Ru_2O_3 and other Ru oxide gas phases such as RuO_3 and RuO_4 [14,15].

The linear nature of log IV and CV characteristics (5.3 and Fig. 5.4) are indications of the thermal stability of the SBDs just before degradation. The donor densities N_D for Ru-6H-SiC which have been extracted from the CV characteristics are in close agreement with that of $9 \times 10^{14} - 1 \times 10^{19} \, cm^{-3}$ given by Cree Research Inc. Although the free carrier densities of 6H-SiC agree with that given by the manufacturer, they are not constant at different annealing temperatures. These differences may be due to the variation of series resistance and the existence of a leakage current in the Schottky contacts which results in the disturbance in the capacitance measurements and, therefore, errors in the estimation of the net doping concentration arise [12,13].
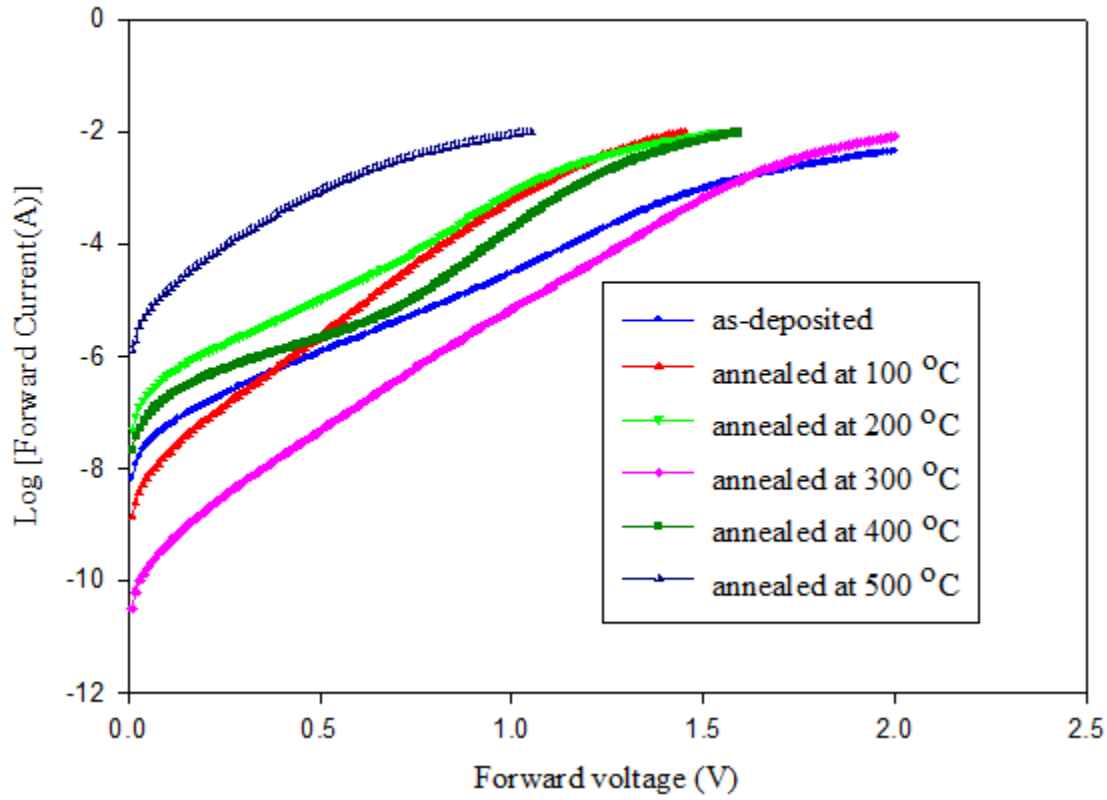
Fig. 5.3. Log IV characteristics of Ru/6H-SiC SBDs annealed in air.
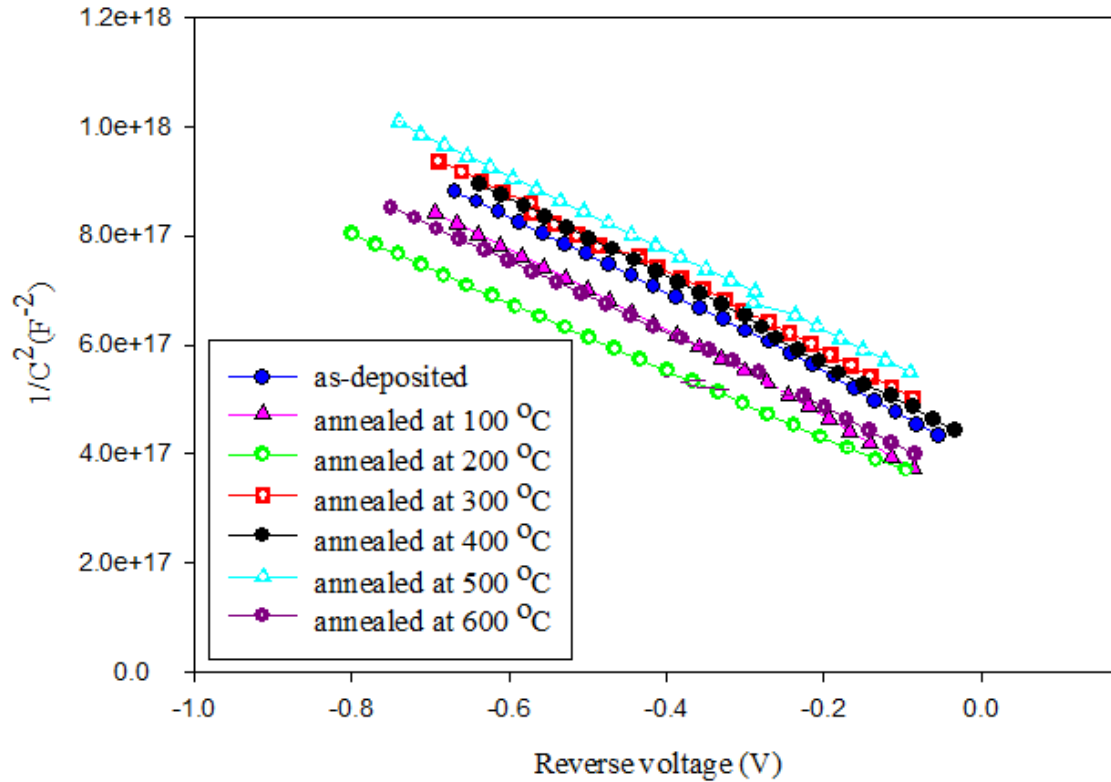
Fig.5. 4. CV characteristics of Ru/6H-SiC SBDs annealed in air.

5.4.2 Conclusion

This study has shown that Ru/6H-SiC SBDs, after annealing in air, exhibit operational integrity up to 600 ºC, and degrade above this temperature as indicated by the extremely high series resistance. The cause of degradation of the Ru/6H-SiC SBDs annealed in the air might be the inter-diffusion of Ru and Si at Ru/6H-SiC interface which has been confirmed by the RBS analysis. It is also noted that the 6H-SiC-based SBDs degrade at a much higher temperature when compared with the 4H-SiC-based SBDs.

5.5 Experimental results for Ru/4H-SiC Schottky barrier diodes annealed in argon.

5.5.1. Experimental Results and Discussion.

The electrical parameters of Ru/4H-SiC SBDs annealed in argon, which are displayed in Table 3, were extracted from IV and CV data as explained in section 5.3.

Annealing Temp	Ideality factor η	SBH from IV (eV)	SBH from CV (eV)	Series Resistance R_s (Ω)	Saturation Current I_S (A)	Donor Density N_D (cm^{-3})	Reverse Current (A) at -2V

As dep	2.636	0.95	2.38	20	2.1×10^{-12}	9.68×10^{15}	3.29×10^{-13}
400ºC	1.008	1.08	2.07	20	1.8×10^{-14}	1.00×10^{16}	3.13×10^{-13}
500ºC	1.191	1.42	3.13	952	3.3×10^{-20}	7.62×10^{15}	2.14×10^{-13}
600ºC	1.692	1.45	2.26	34	8.2×10^{-21}	8.86×10^{15}	1.79×10^{-13}
700ºC	1.660	1.42	2.24	176	1.7×10^{-20}	1.12×10^{16}	1.27×10^{-12}
800ºC	1.259	1.67	1.96	138	2.0×10^{-24}	1.10×10^{16}	6.83×10^{-11}
900ºC*	**		48				-

Table 3. Parameters of Ru/4H-SiC Schottky diodes after various argon annealing temperatures.
** non-exponential IV graph.
      *The Schottky diodes breakdown at this temperature.

From Table 3, ideality factor is observed to generally decrease with annealing temperature. The lowest ideality factor which is very close to unity is obtained for the diode annealed at 400 ºC. This shows that annealing improves the performance of the Schottky diode. The other ideality factors are not very close to unity which means that current conduction in the diodes is not wholly thermionic. There may be other modes of conduction such as tunneling effect and recombination conduction mode. The SBH obtained from CV characteristics is observed to higher than the SBH from IV characteristics. Normally the SBHs that are obtained from CV measurements are slightly higher than those from IV characteristics, as there is a possibility of the existence of an additional capacitance at the metal-semiconductor interface due to the presence of a thin oxide layer which comes as a result of surface preparation [10]. Another explanation for the differences may be the existence of inhomogeneous interfaces, which result in non-uniform Schottky contacts where current can flow via two pathways (i.e. over a lower barrier or a higher barrier) [10]. The formation of Ru_2Si_3, RuO_2 and the interdiffusion of Ru and Si at the Ru/4H-SiC interface as observed by RBS analysis did not lead to dramatic changes in SBH below the annealing temperature of 900 ºC. One possible explanation of the small variation of SBH after the formation of RuO_2 is that the SBHs of Ru and RuO_2 on SiC are nearly equal to each other [14]. Furthermore, Ru_2Si_3 is semiconducting and has a barrier height close to that of Ru on SiC. The SBH of Ru_2Si_3 on silicon (which one can conjecture to be close to that on SiC) of 0.76 eV [16] is very close to the SBH of Ru on SiC.

The donor densies obtained from the CV characteristics closely agree with the carrier density of the wafer of $1.16 \times 10^{16} cm^{-3}$ specified by Cree Research Inc. The non-constant values of free carrier densities can be attributed to capacitance measurement disturbances due to leakage currents in the Schottky contact [12] as explained previously.

It is also observed from Table 3 that there is a general decrease in the saturation current with increasing annealing temperature. We can, therefore, infer that annealing improves the reverse performance of the SBDs.

The series resistance, as observed from Table 3, exhibits some randomness in value after each annealing temperature. These findings are in agreement with Chand [17] who attributed the variation in series resistance to inhomogeneous Schottky contacts.

The SBDs exhibit exponential IV characteristics(Fig. 5.5), partly linear log IV characteristics (Fig. 5.6) and linear CV characteristics (Fig. 5.7) after annealing up to a temperature of 800 ^{o}C despite the occurrence of chemical reactions, and Ru and Si diffusions at the Ru/4H-SiC interface. The best fit line was drawn for the as-deposited CV plot due to the fact that the measuring instrument exhibited some instability during the measurement process. The Schottky diodes degraded and became unusable after annealing at 900 ^{o}C as indicated by the non-exponential IV characteristics (not shown) and awkward value of SBH obtained from CV characteristics. The device failure is attributed to the deep inter-diffusion of Ru and Si at the Ru/4H-SiC interface as indicated by RBS analysis.
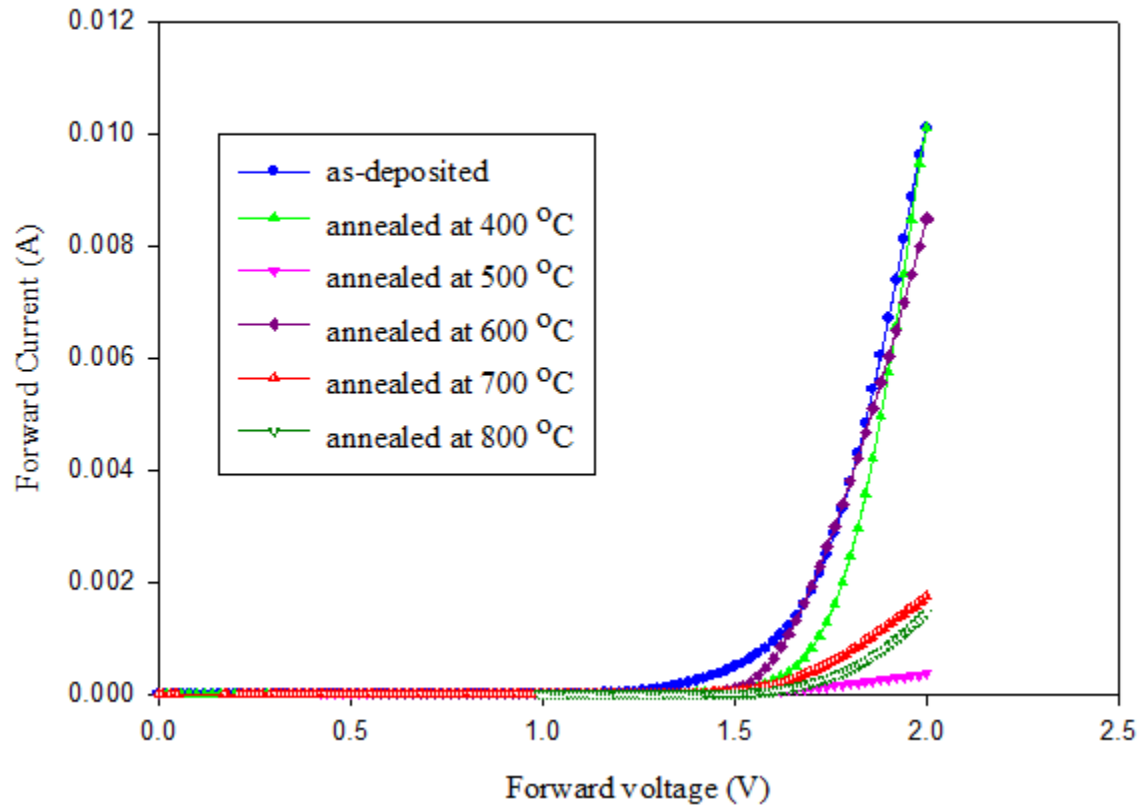
Fig. 5.5. Forward IV characteristics of Ru/4H-SiC SBDs annealed in argon.
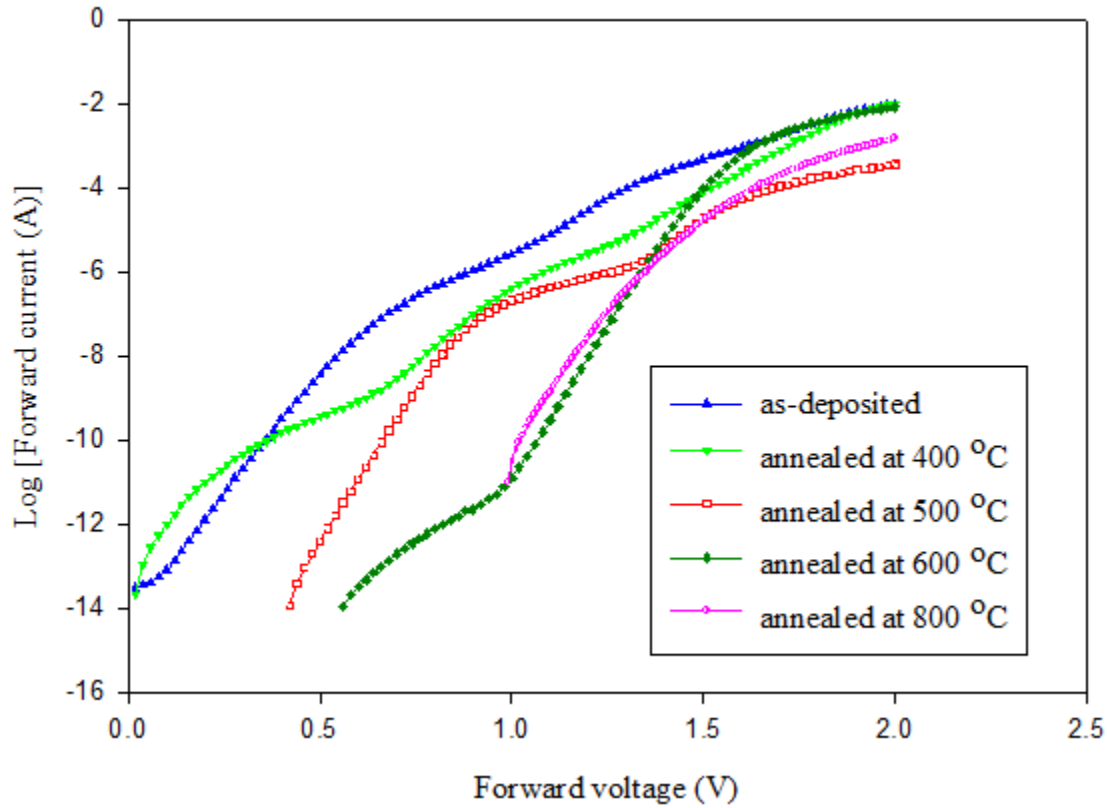
Fig. 5.6. Log IV characteristics of Ru/4H-SiC SBDs annealed in argon.
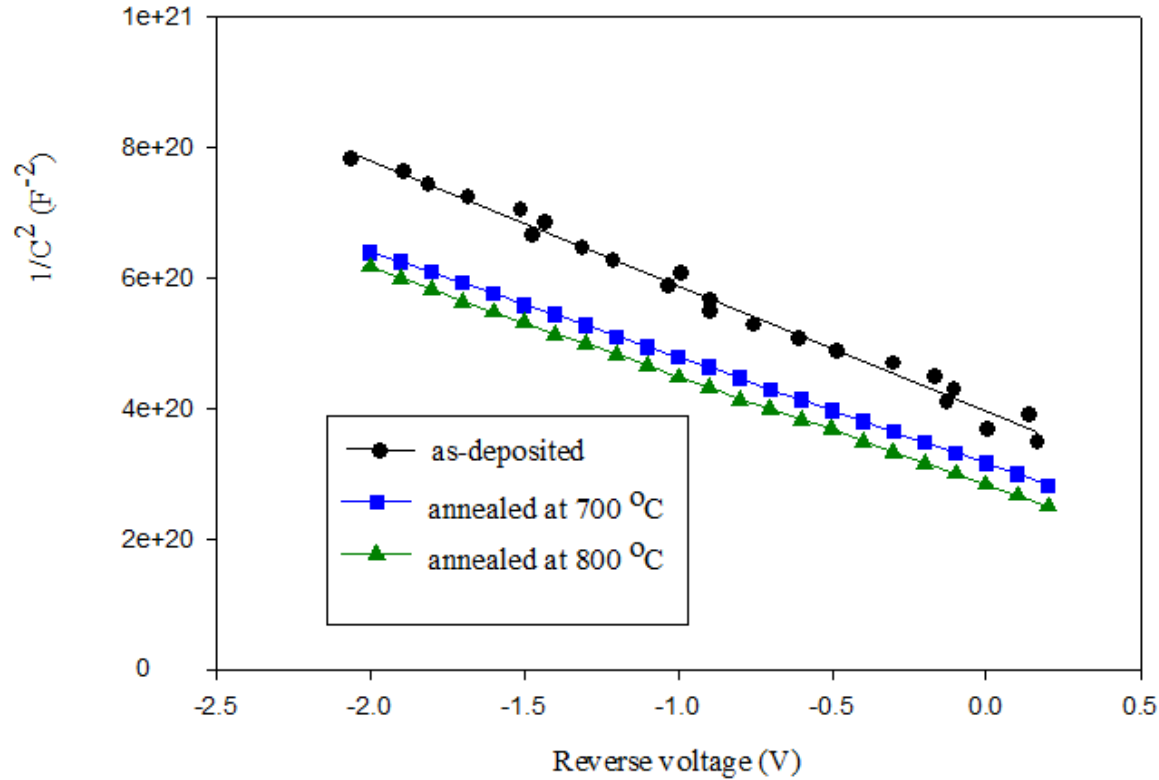
Fig. 5.7. CV characteristics of Ru/4H-SiC SBDs annealed in argon.

5.5.2 Conclusion

The Ru/4H-SiC SBDs exhibit electrical-operational stability, after annealing in argon, up to a temperature of 800 °C. The diodes degrade above this temperature, and the device failure is attributed to the deep inter-diffusion of Ru and Si at the Ru-4H- SiC interface as indicated by the RBS analysis of the sample. It is also noted that the 4H-SiC based diodes breakdown at a much higher temperature when annealed in argon as compared to air annealing.

5.6 Experimental Results for Ru/6H-SiC Schottky barrier diodes annealed in argon

5.6.1 Experimental Results and Discussion

The various electrical parameters of Ru/6H-SiC Schottky diodes annealed in argon which were obtained using the procedures outlined in section 5.3 are displayed in Table 4.

Table 4. Parameters of Ru/6H-SiC Schottky diodes after the various argon annealing temperatures.

Annealing Temperature	Ideality factor η	SBH from IV (eV)	SBH from CV (eV)	Series Resistance R_s (Ω)	Saturation Current I_S (A)	Donor Density N_D (cm^{-3})	Reverse Current (A) at -2V
As deposited	2.770	0.81	0.63	188	7.39×10^{-10}	1.62×10^{18}	3.18×10^{-6}
100°C	2.165	0.78	0.58	175	1.8×10^{-9}	2.24×10^{18}	1.66×10^{-5}
200°C	1.876	0.75	0.81	410	8.1×10^{-9}	2.85×10^{18}	2.21×10^{-5}
300°C	1.995	0.78	0.99	462	2.6×10^{-9}	2.45×10^{18}	6.09×10^{-6}
400°C	1.830	0.72	0.82	292	2.4×10^{-8}	2.73×10^{18}	2.19×10^{-5}
500°C	1.655	0.76	0.94	462	5.1×10^{-9}	1.97×10^{18}	1.86×10^{-5}
600°C	1.949	0.73	0.54	47	1.3×10^{-8}	2.79×10^{18}	8.85×10^{-5}
700°C	1.616	0.85	0.64	114	1.5×10^{-10}	2.47×10^{18}	9.10×10^{-6}

800°C	1.576	0.95	0.96	667	3.0×10^{-12}	2.35×10^{18}	3.11×10^{-7}
900°C	2.050	1.17	1.83	579	5.8×10^{-16}	1.86×10^{18}	2.69×10^{-9}

From Table 4, it is observed that the ideality factor and SBH (obtained from IV characteristics) exhibit some variations with increasing annealing temperature. The fact that the ideality factor is higher than the ideal value of unity may be attributed to the current flow being not by thermionic emission only, but there might be some tunnelling effects and recombination currents involved as well.

The SBHs obtained from CV characteristics were slightly higher than those from IV characteristics. Normally SBH obtained from CV measurements are slightly higher than those obtained from IV characteristics due to the fact that there might be an additional capacitance at the metal-semiconductor interface due to the presence of a thin oxide which comes as a result of surface preparation [9]. The variation of SBH as observed in the table may be attributed to the presence of an inhomogeneous barrier at the metal-semiconductor interface. According to Osvald *et al* [9], SBH inhomogeneity may be due to the fact that there are different crystallographic orientations of the grains in the polycrystalline structure of the metallic layer and also there is a possibility that the phase composition of the interface materials may change after annealing. Both arguments are very applicable to this investigation as there is evidence, from RBS analysis, of the formation of Ru oxide and Ru and Si interdiffusion at the interface at higher annealing temperatures as explained in chapter 4. From the SEM images, there is evidence of a change in the crystallinity of the Ru at higher annealing temperatures.

The saturation current at temperatures less than 600 °C exhibits a randomness in values but decreases at higher annealing temperature up to a final value of 5.78×10^{-16} A. The decrease in saturation current at higher annealing temperatures indicates that annealing improves the reverse performance of the Schottky diode.

The series resistance exhibited some randomness in value after each annealing temperature. This randomness in the value of series resistance is supported by investigations of Chand [17] who in his research paper found out that there is a random variation of series resistance of elementary diodes in inhomogeneous Schottky diodes. At 600 °C, the series resistance is observed to decrease to a low value of 47 Ω. RBS analysis of the thin Ru/6H-SiC film indicates the formation of RuO_2 at this temperature. The SBH of RuO_2 on SiC of 0.88eV [1] does not explain this change in resistance. A comparison of the electrical resistivities of Ru and RuO_2, which are 7.4 μΩcm (polycrystalline) and 35.2 μΩcm respectively, does not offer a plausible explanation for the decrease of series resistance as well. Jelenkovic *et al* [16] similarly observed the reduction of resistivity of

Ru deposited on silicon after annealing at 400 ºC in nitrogen, and they attributed the drop in resistivity to the improvement in grain quality of Ru films. The decrease in series resistance can be attributed to the improvement in the grain quality of Ru or the microcrystalline nature of the Ru oxide formed during the annealing process as evidenced by the SEM images of the thin film of Ru/6H-SiC in Chapter 4.

One can also note that there is a little variation of SBH even after the formation of Ru oxide. One possible explanation of the small change in SBH variation is that the SBH of Ru oxide on SiC of 0.88 eV [14] is very close to the SBH of Ru on SiC.

A plot of $\dfrac{1}{C^2}$ vs reverse voltage (Fig.5.8) exhibits excellent linearity from the as-deposited diodes to the diodes annealed at the final annealing temperature of 900 ºC. The linearity indicates the operational integrity of the Schottky diodes after annealing at extremely high annealing temperatures.

The factory specification of N_D for the 6H-SiC wafer that was used in this investigation was $9 \times 10^{14} - 1 \times 10^{19}\,\text{cm}^{-3}$. The values of N_D obtained in this investigation are within the range of the specification given by Cree Research Inc.

The forward log IV characteristic for the Schottky diodes (Fig. 5.9) shows good rectification behaviour. The Ru/6H-SiC Schottky diodes degrade when annealed at 1000 ºC as evidenced by a non-linear CV graph (not shown). The degradation of the Schottky diode can be attributed to the deterioration of the Ru Schottky contact due to the inter-diffusion of Ru and Si at the Ru/6H-SiC interface as indicated by RBS analysis of the sample at 1000 ºC as described in Chapter 4.
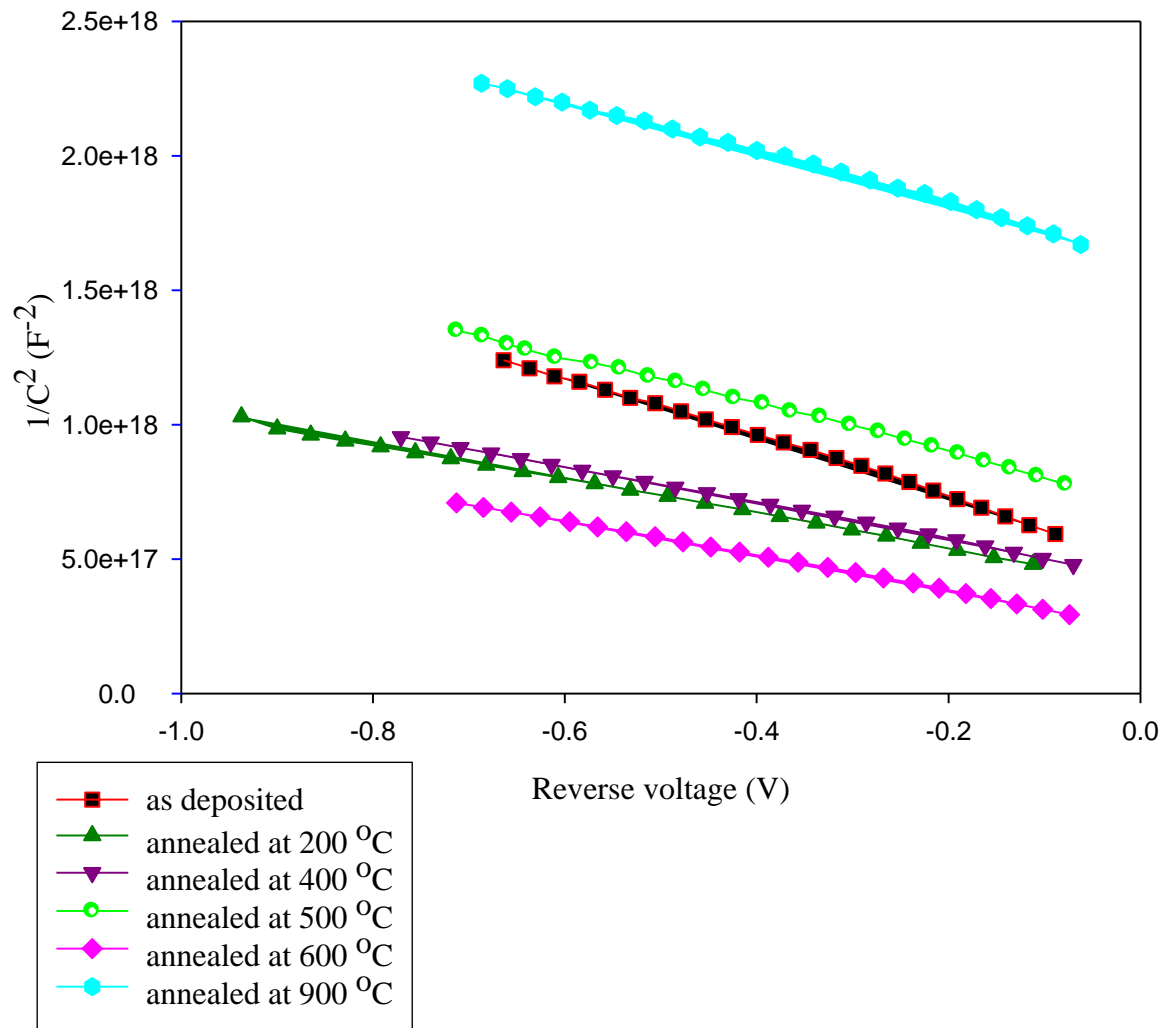
Fig. 5.8. A plot of $1/C^2$ vs reverse voltage for Ru/6H-SiC SBDs after annealing at various temperatures in argon.
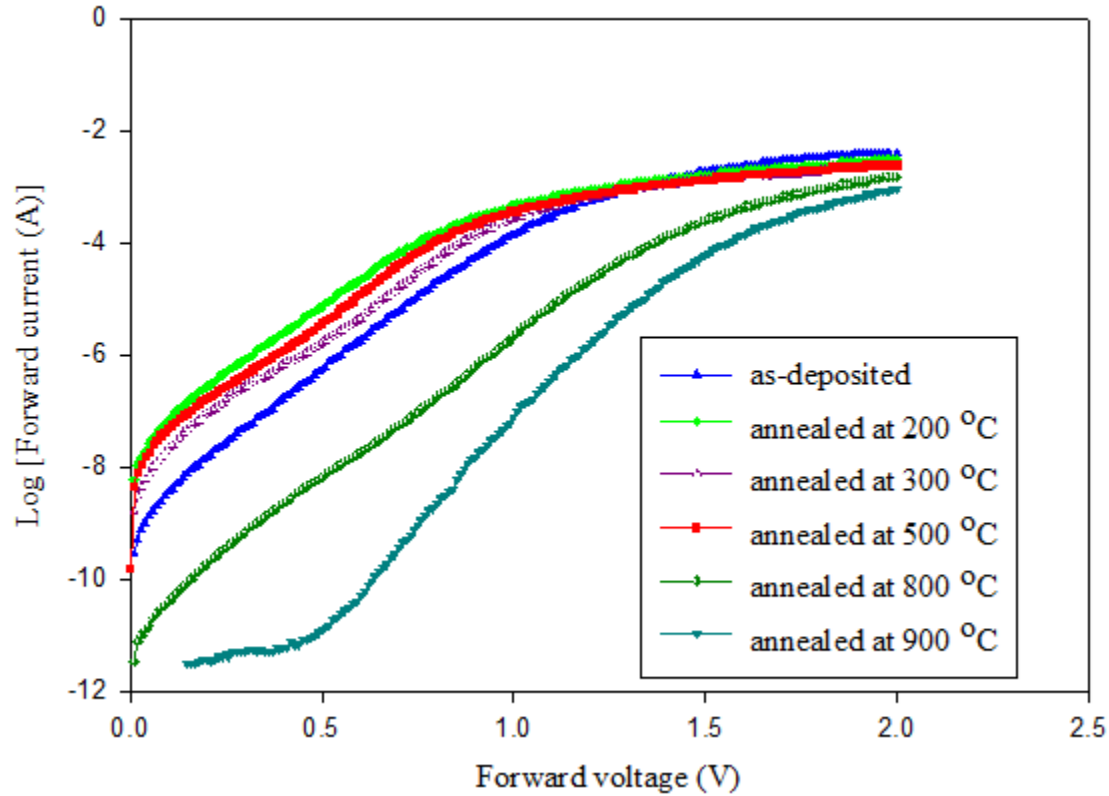
Fig. 5.9. Log IV characteristics for Ru/6H-SiC SBDs annealed in argon at various temperatures.

5.6.2. Conclusion

The Ru/6H-SiC Schottky diodes that were fabricated showed good rectification behaviour and exhibited linear CV characteristics after annealing in argon up to the final temperature of 900 °C. From the data obtained in this investigation, annealing the SBDs in argon at a temperature of 600 °C gives the lowest series resistance of the SBDs. The investigation has shown that 6H-SiC without an epilayer is able to produce excellent Schottky diodes which can operate at extremely high temperatures. The degradation mechanism of the Schottky diodes has been shown to be the inter-diffusion of Ru and Si at the Ru/SiC interface.

5.7 Experimental results for Ru/4H-SiC Schottky barrier diodes annealed in a vacuum.

5.7.1. Experimental Results and Discussion.

Table 5 shows the parameters that were extracted at room temperature by using IV and CV characteristics, as explained in section 5.3, of the Ru/4H-SiC diodes which were annealed in a vacuum.

Table 5. Parameters of Ru/4H-SiC Schottky diodes extracted at room temperature.

Annealing temperature	Ideality factor η	SBH from IV (eV)	SBH from CV (eV)	Series Resistance R_s (Ω)	Saturation Current I_S (A)	Donor Density N_D (cm^{-3})	Reverse Current (A) at -2V
As dep	2.636	0.95	2.38	20	2.1×10^{-12}	9.68×10^{15}	3.29×10^{-13}
500ºC	1.350	1.27	1.91	17	5.8×10^{-18}	7.88×10^{15}	3.09×10^{-13}

600ºC	1.336	1.33	2.41	92	1.0×10^{-18}	9.25×10^{15}	1.12×10^{-12}
700ºC	1.822	0.79	2.30	12	1.2×10^{-12}	9.80×10^{15}	1.48×10^{-12}
800ºC	1.211	1.11	1.93	7	6.0×10^{-15}	9.36×10^{15}	1.5×10^{-10}
900ºC	1.448	0.95	1.83	8	2.6×10^{-12}	9.35×10^{15}	5.42×10^{-8}
1000ºC*	1.376	0.76	1.53	13	4.9×10^{-9}	8.67×10^{15}	4.86×10^{-5}

*SBDs were still functional after annealing at this temperature.

From the data in Table 5, it is observed that the saturation current shows some fluctuations at different annealing temperatures. This fluctuation is explained by using equation 5.2 and the SBH values obtained from IV characteristics.

$$J_S = A^*T^2 \exp\left(-\frac{q\phi_{Bn}}{kT}\right) \tag{5.2}$$

From the equation, it can be seen that if the SBH decreases, there should be a corresponding increase in the saturation current. An increase of SBH should lead to a decrease in the reverse saturation current. The data in the table clearly confirms this relationship. The log IV plots (Fig 5.10) exhibit linearity for the most part after annealing at different temperatures which is an indication of the SBDs operational integrity.

A plot of IV characteristics (Fig .5.11) exhibits excellent exponential curves which indicate that SBDs generally obey the thermionic emission current transport model. A close scrutiny of the IV characteristics reveals that the forward voltage drop of the SBDs, V_F, generally decreases with increasing annealing temperature. This behaviour can be explained by using the equation 5.3 of the forward voltage drop of the Schottky diode [18].

$$V_F = \frac{\eta kT}{q} \ln\left(\frac{J_F}{A^*T^2}\right) + \eta\phi_{Bn} + R_{on,sp}J_F \tag{5.3}$$

J_F is the forward current density, and $R_{on,sp}$ is the specific on-resistance which is equal to the sum of the series resistance of a substrate and drift region.

From Table 5, it can be observed that the series resistance generally decreases after annealing temperatures of 700 ºC and above. The decrease in series resistance may be attributed to the increase in ionization of the donor atoms at high annealing temperatures [18].The other reason may be that the Schottky contact becomes more intimate with the substrate after annealing. It is also observed from the table that fluctuations of ideality factor and SBH at various annealing temperatures are very small. Using these data and equation 5.3, the forward voltage drop of the Schottky diodes should be expected to decrease with increasing annealing temperature. This is generally demonstrated by the IV characteristics of the SBDs in Fig.5.11. From the data in the table, it can also be easily seen that there is an inverse relationship between ideality factor and SBH obtained

from IV characteristics. That is, when the SBH increases, the ideality factor decreases and vice-versa. This observation is in agreement with that of Guy *et al* [19] who suggested that the two parameters are not independent of one another.

Another observation that can be made from the data in Table 5 is that the SBHs which were obtained from CV characteristics are higher than those which were obtained from IV characteristics. Normally SBHs which are obtained from CV measurements are slightly higher than those from IV characteristics due to the fact that there might be an additional capacitance at the metal-semiconductor interface due to the presence of a thin oxide which comes as a result of surface preparation [10]. The other reason for the differences might be due to the presence of inhomogeneous interfaces which result into non-uniform Schottky contacts where current can flow via two pathways (i.e. over a lower barrier or higher barrier) [10].

The linear nature of the CV characteristics of SBD in Fig.5.12 is an indication of the electrical operational-integrity of the Schottky diodes even after annealing at extremely high temperatures. The donor density that was extracted from the CV characteristics closely agrees with the donor density specification of the 4H-SiC wafer of $1.16 \times 10^{16} cm^{-3}$ given by Cree Research Inc. The best fit line was drawn for CV characteristics for the as-deposited SBD because the data was scattered due to the instability of the measuring instruments. The operational stability of the SBDs can be explained by looking at the individual processes that occur at the surface of the Schottky contact, and interface of the Schottky contact and 4H-SiC. What can be noted from the outset is that the fluctuations of SBH are small even after the formation of ruthenium silicide and graphite. The formation of Ru_2Si_3 at temperatures of 700 °C and above, as indicated by RBS analysis and Raman spectroscopy, does not lead to dramatic changes to electrical properties of the SBDs because Ru silicide is semiconducting and has a barrier height which is close to that of Ru on SiC. The SBH of Ru_2Si_3 on silicon (which we can conjecture to be close to that on SiC) of 0.76 eV [16] is very close to the SBH of Ru on SiC. The graphite that is formed has been found to behave as a Schottky contact at an annealing temperature of 1000 °C [20, 21]. Lu *et al* [21] also found out that the carbon contact on SiC exhibited Schottky and ohmic contact behaviour in the annealing temperature range of 900-1350 °C. From their study, they found that the temperature of transition from Schottky to an ohmic contact in Carbon/SiC structure depended on two conditions namely, the doping concentration of SiC and amount of nano-graphitic flakes formed. Amorphous carbon has been found to convert to conducting graphite-like structures around 900 °C.

In this investigation, the Ru/4H-SiC Schottky contact did not transform to an ohmic contact at 1000 °C. The Ru/4H-SiC SBDs did not breakdown even after annealing at 1000 °C. The researcher intended to anneal at temperatures above 1000 °C, but the vacuum annealing equipment was limited to an operating temperature of 1000 °C.
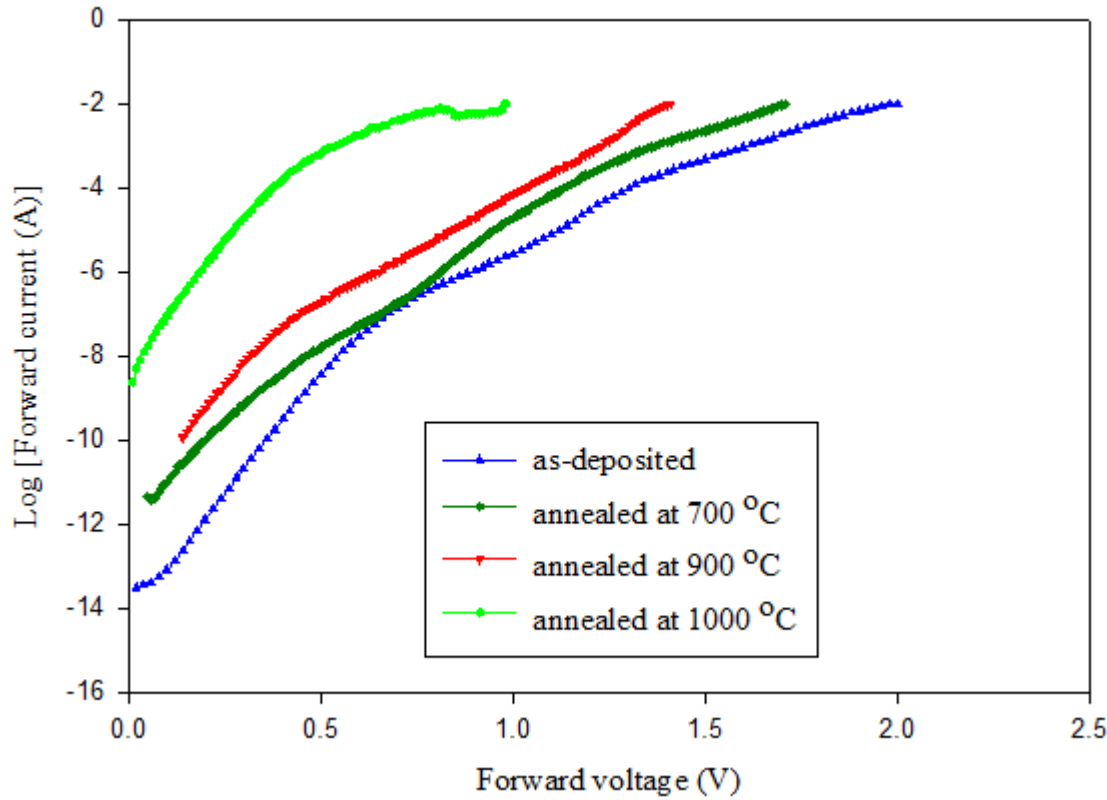
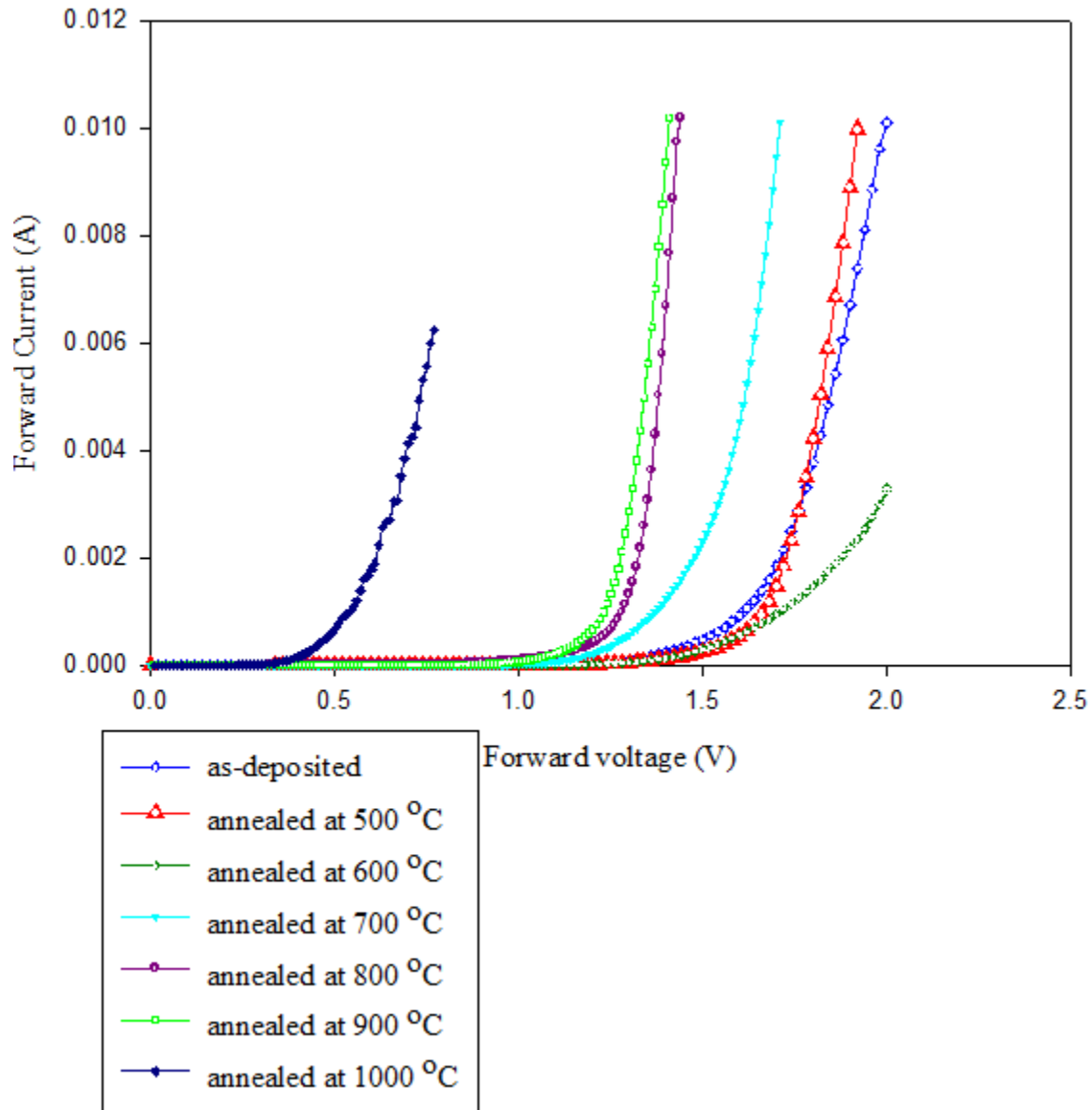Fig.5.10 Log IV characteristics of Ru/4H-SiC SBDs annealed in a vacuum.

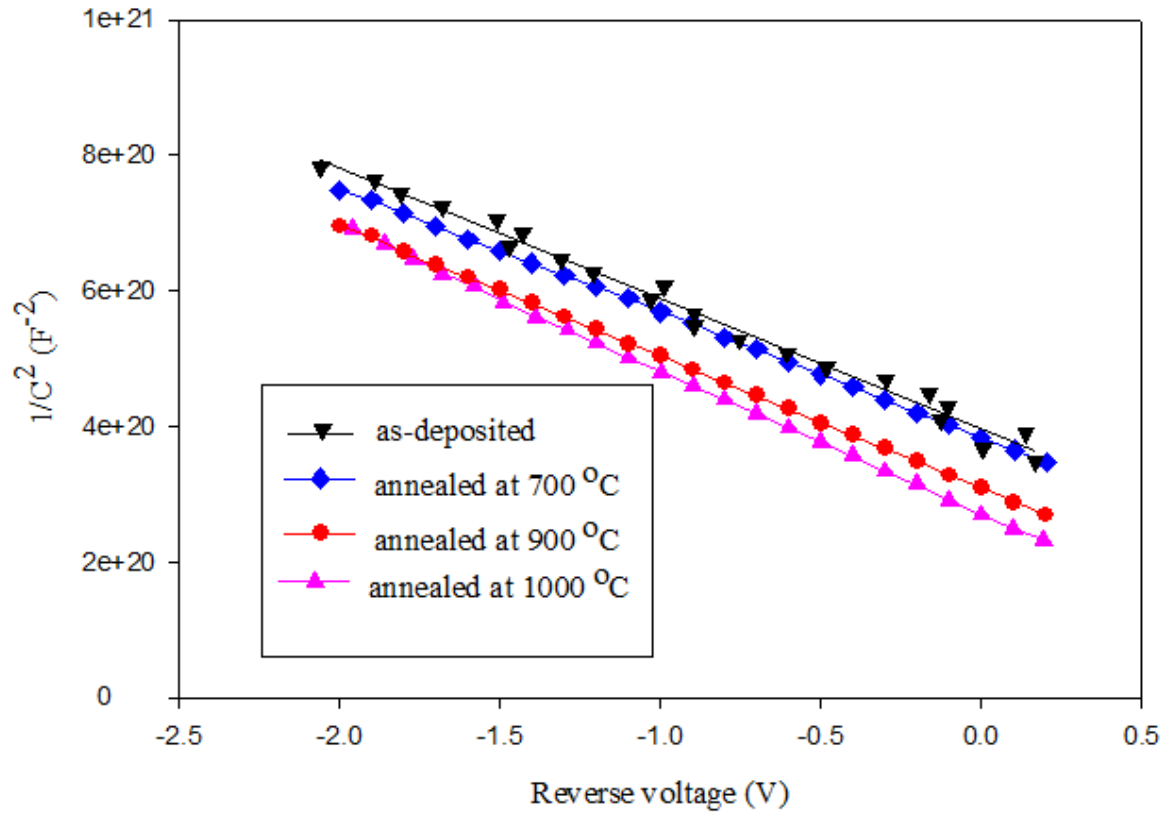Fig.5.11. IV characteristics (obtained at room temperature) of Ru/4H-SiC SBDs annealed in a vacuum.

Fig. 5.12. CV characteristics of Ru/4H-SiC SBDs annealed in vacuum.

5.7.2. Conclusion

This investigation has shown that even though there was interdiffusion at the interface of ruthenium and 4H-SiC, and evidence of formation of ruthenium silicide and graphite after annealing at temperatures of 700 °C and above, there were no dramatic changes in the electrical properties of the SBDs. Furthermore, the SBDs did not degrade even after annealing at 1000 °C. The Ru/4H-SiC Schottky diodes that were fabricated showed excellent rectifying behaviour by exhibiting linear CV characteristics and exponential IV characteristics up to the final annealing temperature of 1000 °C. These findings provide a hopeful future in the commercial fabrication of extremely high-temperature 4H-SiC-based diodes. However before commercial fabrication of these high temperature operating Schottky diodes is done, further investigations should be carried out to ascertain the occurrence of this excellent rectification behaviour during the annealing process. This can be done by doing the CV and IV characterisation during the annealing process (that is, one needs to perform *in situ* CV and IV characterisation). In addition a method of making hermetically sealed SBDs will need to be explored.

5.8 Experimental results for Ru/6H-SiC SBDs annealed in a vacuum.

5.8.1. Experimental Results and Discussion.

Table 6 contains the diode parameters that were extracted from CV and IV characteristics with the help of procedures outlined in section 5.3.

Table 6. Parameters of Ru/6H-SiC Schottky diodes at various vacuum annealing temperatures.

Annealing Temp.	Ideality factor η	SBH From IV (eV)	SBH From CV (eV)	Series Resistance R_s (Ω)	Saturation Current I_S (A)	Donor Density N_D (cm^{-3})	Reverse Current (A) at -2V
As dep	3.511	0.49	0.60	31	7.6×10^{-5}	2.34×10^{18}	7.69×10^{-3}
500°C	2.845	0.53	1.70	25	1.7×10^{-5}	7.85×10^{18}	-

600°C	1.962	0.54	1.26	16	1.4×10^{-5}	5.25×10^{18}	4.23×10^{-3}
700°C	1.271	0.49	1.73	20	7.5×10^{-5}	3.28×10^{18}	-
800°C	1.296	0.53	*	12	1.7×10^{-5}	*	-
900°C	1.472	0.42	**	5	1.4×10^{-3}	**	-

*SBDs breakdown at this temperature as indicated by non-linear CV characteristics.
** CV data is scattered all over the graph area.

From the Table 6, it is observed that the as-deposited ideality factor is high but generally decreases with annealing temperature. This shows that the performance of the SBD improves with annealing temperature. Another observation that can be made is that SBHs obtained from IV characteristics are lower than those obtained from CV characteristics. Normally the SBHs that are obtained from CV measurements are slightly higher than those from IV characteristics due to the possibility of the existence of an additional capacitance at the metal-semiconductor interface which results from the presence of a thin oxide layer which comes as a result of surface preparation [10]. Another reason for the differences may be due to the existence of inhomogeneous interfaces, which result in non-uniform Schottky contacts where current can flow via two pathways (i.e. over a lower barrier or a higher barrier) [10]. A plot of the CV characteristics (Fig.5.13) indicates that the SBDs are stable after annealing up to a temperature of 700 °C, and above this temperature the performance of the SBD deteriorates as evidenced by the non-linear nature of the CV characteristic. This deterioration in performance may be attributed to the diffusion of Ru into SiC as indicated by RBS analysis of Ru/6H-SiC thin films. The formation of Ru_2Si_3 at temperatures of 800°C as indicated by RBS analysis cannot be the cause on its own for the worsening of the performance of the Schottky diode as the silicide is semiconducting and has a barrier height close to that of Ru. The SBH of Ru_2Si_3 on silicon (which one can conjecture to be close to that on SiC) of 0.76 eV [16] is very close to the SBH of Ru on SiC. It is the carbon released during the reaction process that may be the cause of poor performance of the diode.

The free carrier density of 6H-SiC wafer that was extracted from the CV characteristics is within the range of 9×10^{14}-1×10^{19} cm^{-3} that was specified by the manufacturer of the wafer, Cree Research Inc. Even though the free carrier densities extracted from CV characteristics are within the range given by the manufacturer, they are not constant at different annealing temperatures. The non-constant values of free carrier densities might be due to errors that arise due to variation in series resistance and the disturbances in the capacitance measurements which come from the existence of leakage currents in the Schottky contacts [12, 13].

From the plot of IV characteristics (Fig.5.14), it is observed that the forward voltage drop V_F generally decreases with higher annealing temperatures. This electrical behaviour is similar to the one in section 5.7.1 and can be explained in a similar manner with the help of the equation 5.3. The log IV plots (Fig 5.15) for the most part exhibit linearity at different annealing temperatures.

From Table 6, it can be observed that there is a general decrease of series resistance with increasing annealing temperature. The decrease in series resistance may be attributed to the increase in ionization of the donor atoms at high annealing temperatures [18]. The other reason may be that the contact becomes more intimate with the substrate as the annealing temperature is increased.

The SBDs become ohmic after annealing at 900 $^{\circ}$C as evidenced by a straight line IV characteristic in Fig 5.10. The ohmic behaviour exhibited by the Ru/6H-SiC SBDs at this annealing temperature may be attributed to the formation of graphite at the metal-SiC interface as confirmed by Raman analysis. This finding is supported by Seyller et al [20] who in their studies found that the formation of graphite at the metal-SiC interface may lead to ohmic contact formation as the SBH of graphite on n-type 6H-SiC is very small (about 0.3 eV). Lu et al [21] also found out that the carbon contact on SiC exhibited Schottky and ohmic contact behaviour in the annealing temperature range of 900-1350 $^{\circ}$C. They found that the temperature of transition from Schottky to an ohmic contact in Carbon/SiC structure depended on the doping concentration of SiC and amount of nano-graphitic flakes formed. They concluded that the lower doping concentration in SiC requires higher annealing temperature to achieve ohmic contacts in carbon/SiC structures. These findings agree with this investigation in that the 6H-SiC which had a higher doping concentration (than 4H-SiC) had a lower temperature Schottky-ohmic transition.
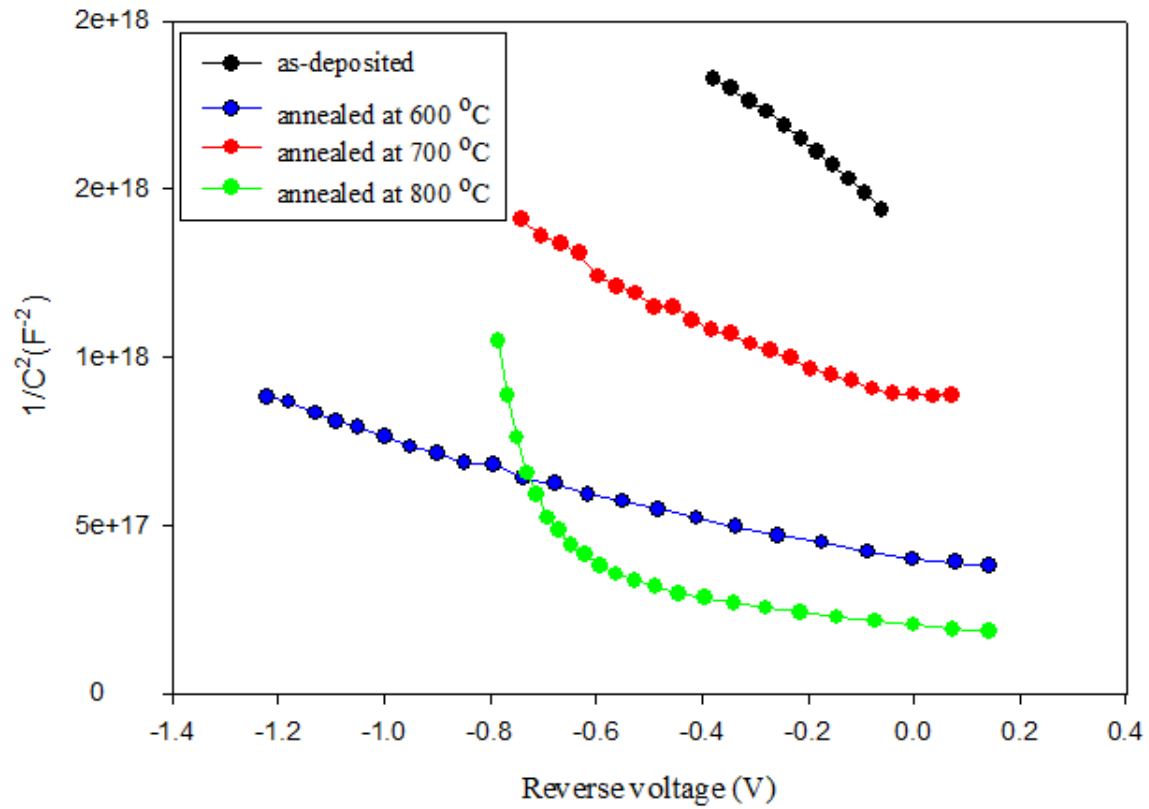
Fig. 5.13. CV characteristics obtained at room temperature of Ru/6H-SiC annealed in a vacuum.
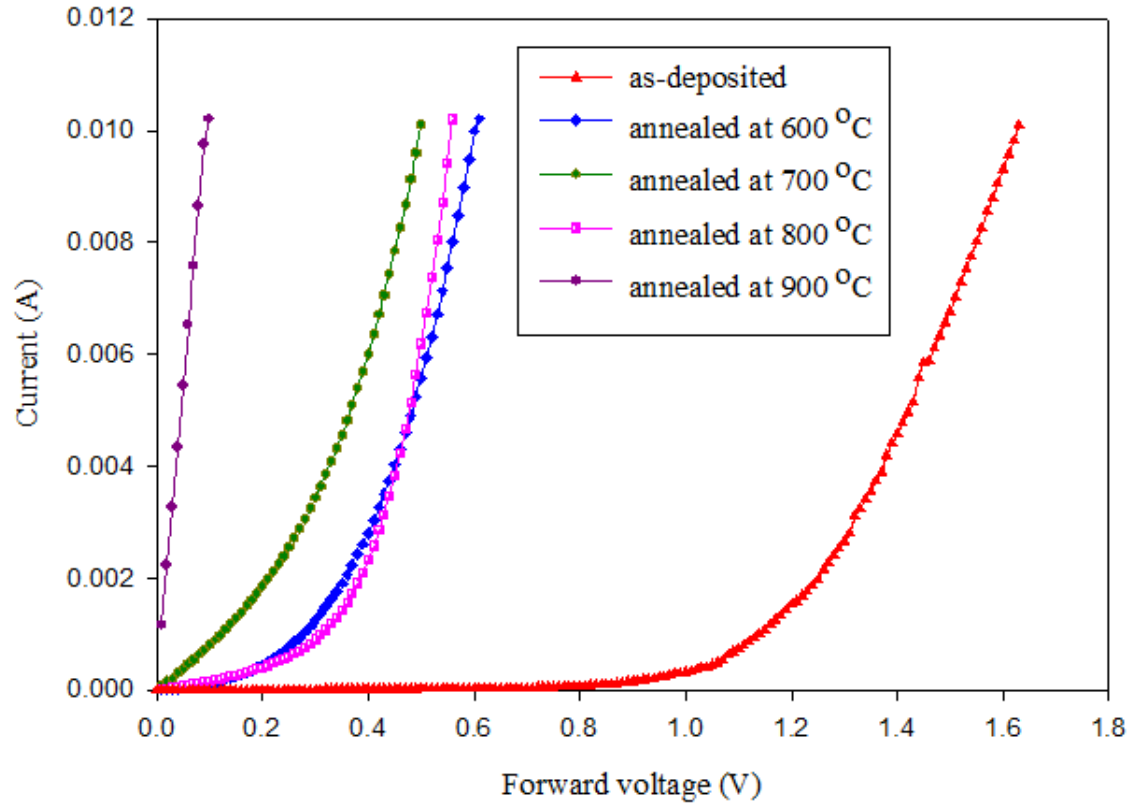
Fig. 5.14. IV characteristics obtained at room temperature of Ru/6H-SiC annealed in a vacuum.
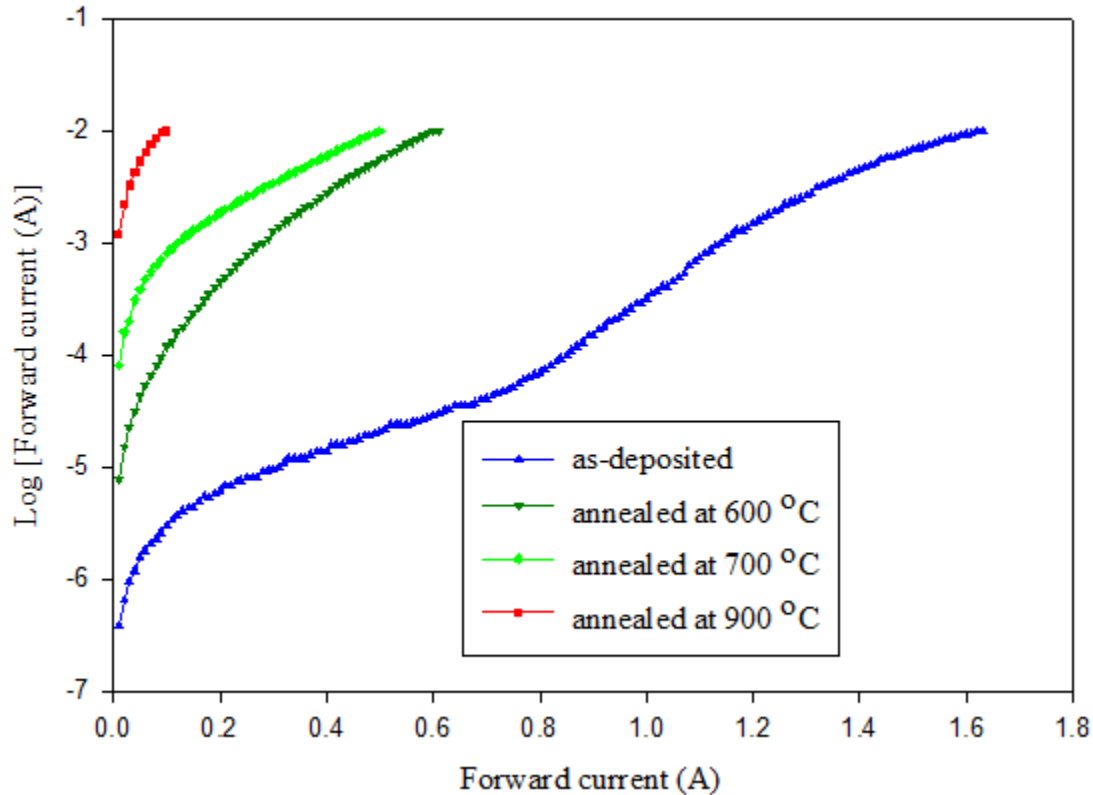
Fig. 5.15. Log IV characteristics obtained at room temperature of Ru/6H-SiC annealed in a vacuum.

5.8.2. Conclusion

This investigation has shown that the Ru/6H-SiC SBDs after annealing in a vacuum remain operational after annealing up to a temperature of 700 °C and degrade above this temperature. The degradation of the Schottky diode is explained by the fact that the Schottky contact becomes ohmic due to the formation of graphite. The formation of graphite results from the silicide formation which releases free carbon from SiC. Silicide

formation has been confirmed by Raman spectroscopy.The diffusion of Ru into the SiC layer might be another reason for the poor performance of the diode after an annealing temperature of 700 ºC as indicated by RBS analysis of thin films of Ru/6H-SiC.

5.9 Discussion

This investigation has shown that SBDs of both SiC polytypes degrade at a much lower temperature when annealed in the air when compared to those annealed in argon and a vacuum. The reason for low-temperature degradation in air annealing is attributed to the excessive inter-diffusion of Ru, Si and C at the Schottky interface, and the formation of non-semiconducting oxides of Ru. Londono-Hurtado *et al* [22] argued in their paper that there is a possibility of the introduction of defects in the SiC crystal through the incorporation of Ru and oxygen into the crystal under some favourable oxygen partial pressure. They further argued that the introduction of the defects will increase the diffusion of Ru through the crystal. A comparison of the two polytypes of SiC shows that 6H-SiC based diodes degrade at a higher temperature that 4H-SiC based diodes when annealed in air. This difference in performance may be explained by the fact that the 4H-SiC had an epilayer (while the 6H-SiC was bulk-grown) whose integrity might have been compromised by interdiffusion of the elements and oxidation at the Ru-SiC interface. Epilayers which are not grown properly have been found to have high defect densities of dislocations and stacking faults, interface defects, and tendency to crack [23] .

From the results, it can also be said that SBDs of both SiC polytypes which are annealed in argon degrade at a relatively higher temperature when compared with those that are annealed in air. The 6H-SiC-based diodes degrade after annealing at 1000 ºC in argon which is slightly higher than that of the 4H-SiC-based diodes which degrade after annealing at 900 ºC. The SBDs of both SiC polytypes annealed in argon degrade due to interdiffusion of elements at the Schottky interface. A similar reason to the case of lower degradation temperature of air-annealed 4H-SiC based diode can be given for the lower degradation temperature of the argon annealed 4H-SiC-based diodes (when compared to 6H-SiC diodes).

The 6H-SiC based SBDs annealed in a vacuum degrade due to the transformation of the Schottky contact to an ohmic contact. This Schottky contact to ohmic contact transformation is due to the formation of graphite flakes at the Schottky interface as evidenced from the Raman analysis of the thin film samples as explained in chapter 4.

The 4H-SiC based SBDs annealed in a vacuum did not degrade up to the final annealing temperature of 1000 °C. These diodes could not be annealed to a temperature higher than 1000 °C because the vacuum annealing system had a maximum annealing temperature of 1000 °C. From the Raman analysis of the Ru/4H-SiC thin films, there is evidence of formation of graphite flakes at the Schottky interface at this maximum temperature. Even though there is a formation of graphite, the Schottky contact did not transform to an ohmic contact. According to Lu *et al* [21], the temperature of transition from Schottky to an ohmic contact in Carbon/SiC structure depends on the doping concentration of SiC and amount of nano-graphitic flakes formed. Since the 6H-SiC and 4H-SiC used in this research had different doping densities, the Schottky to ohmic transition temperatures should be different.

This study has also shown that 4H-SiC based diodes can operate at extremely high temperatures of more than 1000 °C when operated in a vacuum. However before technologies of building vacuum enclosures for diodes can be explored, more work needs to be done to establish the operational integrity of the diodes during the annealing process. This can be done by carrying out *in-situ* IV and CV characterisation. The investigation has also shown that the breakdown temperature of diodes made from both polytypes is extremely high in argon annealing. Enclosing the diodes in an argon environment can be technologically easier than that of vacuum enclosure. The lowest operating temperatures are obtained when the diodes are annealed in air. The possible reasons for low air-operation temperature are excessive elemental diffusion at the Ru-SiC interface and the oxidation of Ru to form non-semiconducting phases as explained in chapter 4.

5.10 Conclusion

The Schottky diode results have shown that diodes which are annealed in argon and vacuum will breakdown at extremely higher temperatures than those annealed in air. This means that for extreme temperature applications, the SiC diodes must be hermetically sealed in an argon or vacuum environment. The study has also shown that 4H-SiC based diodes have a higher breakdown temperature when compared to the 6H-SiC based diodes when both are annealed in a vacuum. These findings have huge positive implications in the exploitation of SiC-based diodes in applications which involve extremely high operating temperatures. These applications can include rectification and sensor applications in avionics, motor vehicles, nuclear power production instrumentation and space rockets.

5.11 References

[1] L. Stuchlikova, D. Buc, L. Harmatha, U. Helmersson, W. H. Chang, I. Bello, *Deep energy levels in RuO₂/4H–SiC Schottky barrier structures*, Applied Physics Letters 88, 153509, (2006).

[2] D. Buc, L. Stuchlikova, U. Helmersson, W.H. Chang., I. Bello, *Investigation of RuO2/4H–SiC Schottky diode contacts by deep level transient spectroscopy*, Chemical Physics Letters **429** 617–621, (2006).

 [3] D. Buc, L. Stuchlikova, L. Harmatha, I. Hotovy, *Electrical characterization of 4H–SiC Schottky diodes with a RuO₂ and a RuWOₓ Schottky contacts*, Journal of Materials Science: Materials in Electronics **19**:783–787, (2008).

 [4] S. Roy, C. Jacob, M.Zhang, S. Wang, A.K. Tyagi, S. Basu, *SIMS, RBS and glancing incidence X-ray diffraction studies of thermally annealed Ru/β-SiC interfaces*, Applied Surface Science **211**, 300–307, (2003).

 [5] A. Venter, M.E.Samiji, A.W.R.Leitch , *Thermal stability of Ru, Pd and Al Schottky contacts to p-type 6H-SiC*, Physica Status Solidi (c) **1**, No. 9, 2264– 2268, (2004).

 [6] A. Venter, M.E. Samiji, A.W.R. Leitch, *Formation of surface states during Schottky barrier fabrication on Al-doped p-type 6H–SiC*, Diamond and Related Materials **13**,1166–1170, (2004).

[7] K.V. Munthali, C. Theron, F.D. Auret, S.M.M. Coelho, E. Njoroge, L. Prinsloo, *Solid state reaction of ruthenium with silicon carbide, and the implications for its use as a Schottky contact for high temperature operating Schottky diodes*, Material Science and Engineering B 181, 9-15, (2014).

[8] S.M. Sze, Semiconductor Devices Physics Technology, John Wiley & Sons, New York, (2002).

[9] J. Osvaldy, E. Dobrockaz, *Generalized approach to the parameter extraction from I –V characteristics of Schottky diodes*, Semiconductor Science Technology, 1198-1202, (1996).

[10] F. La Via, F. Roccaforte, A. Makhtari, V. Raineri, P. Musumeci, L. Calcagno, *Structural and electrical characterisation of titanium and nickel silicide contacts on silicon carbide*, Microelectronic Engineering, 60, 269–282, (2002).

 [11] M. Sochacki, J. Szmidt, M. Bakowski, A. Werbowy, *Influence of annealing on reverse current of 4H–SiC Schottky diodes*, Diamond and Related Materials 11, 1263–1267, (2002).

[12] M. Siva Pratap Reddy, V. Rajagopal Reddy, Chel-Jong Choi, *Electrical properties and interfacial reactions of rapidly annealed Ni/Ru Schottky rectifiers on n-type GaN*, Journal of Alloys and Compounds, 503, 186–191,(2010).

[13]C. Frojdh, G.Thungstrom, H.E. Nilsson, C.S. Petersson, *Schottky Barriers on 6H-SiC*, Physica Scripta Vol. T79, page 297-302, (1999).

[14] E. Stuchlikova, L. Harmatha, D. Buic, J. Benkovska, B. Hlinka, G. G. Siu, *4H-SiC Diode with a RuOX and a RuWOₓ Schottky Contact Irradiated by Fast Electrons*, IEEE, (2006).

[15] M.M. Steeves, Electronic transport properties of ruthenium and ruthenium oxide thin films, A Ph.D. thesis, (unpublished results).

[16] E.V. Jelenkovic, K .Y. Tong, W. Y. Cheung, S. P. Wong, *Physical and electrical properties of sputtered Ru2Si3/Si structures*, Semiconductor Science Technology **18**, 454-459, (2003).

[17] S. Chand, *Theoretical evidence for random variation of series resistance of elementary diodes in inhomogeneous Schottky contacts*, Physica B **373**, 284-290, (2006).

[18] R. Raghunathan, D. Alok, B.J. Baliga, *High Voltage 4H-SiC Schottky Barrier Diodes*, IEEE Electron Device Letters, Vol. 16. No. 6, (1995).

[19] O.J. Guy, M. Lodzinski, A. Castaing, P.M. Igic, A. Perez-Tomas, M.R. Jennings, P.A. Mawby, *Silicon carbide Schottky diodes and MOSFETS: solutions to performance problems,* 2008 13th International Power Electronics and Motion Control Conference.

[20] T. Seyller, K.V. Emtsev, F. Speck, K.Y. Gao, L. Ley, *Schottky barrier between 6H-SiC and graphite: Implications for metal/SiC contact formation*, Applied Physics Letters 88, 242103 (2006).

[21] W. Lu, W.C. Mitchel, C.A. Thornton, G.R. Landis, W.E. Collins, *Carbon Structural Transitions and ohmic contacts on 4H-SiC*, Journal of Electronic Materials, Vol. 32, No. 5 (2003).

[22] A. Londono-Hurtado, A.J. Heim, S. Kim, I. Szlufarska, D. Morgan, *Cs and Ag co-incorporation in cubic silicon carbide*, Journal of Nuclear Materials 439, 65-71, (2013).

[23] Y. K. Yeo, A. C. Bergstrom, R. L. Hengehold, J. W. Wei, S. Guha, L. P. Gonzalez, G. Rajagopalan, Mee-Yi Ryu, *Optical and Electrical Properties of Bulk-grown Ternary $In_xGa_{1-x}As$*, Journal of the Korean Physical Society, Vol. 58, No. 5, pp. 1267-1273, (2011).

CHAPTER 6

GENERAL SUMMARY, CONCLUSION AND FUTURE WORK.

6.1 General Summary and Conclusion

This study has shown that there is solid state diffusion of ruthenium in both 4H-SiC and 6H-SiC in the air, argon and vacuum annealing environments. Diffusion of ruthenium into SiC starts at a much higher annealing temperature in a vacuum, whereas in air annealing diffusion commences at a much lower temperature.

In the air, surface oxidation of Ru/4H-SiC happens after annealing at a temperature of 400 ^{o}C as indicated by RBS analysis. From Raman spectroscopy, it has been shown that the oxide formed is not RuO_2. So we can conjecture that other stoichiometries of oxides such as gaseous RuO and low temperature melting RuO_4 or RuO_3 (which is known to vaporise at 1200 ^{o}C) or Ru_2O_3 may have been formed. According to Di Lemma *et al* [1], the phase changes of gaseous oxides namely RuO_3 and RuO_4 depend on temperature. These gaseous oxides normally decompose to the most stable solid Ru oxide of the form RuO_2. The formation of a silicide of stoichiometry Ru_2Si_3 after air annealing at a temperature of 600 ^{o}C has also been shown by Raman analysis of the sample. Diffusion of Ru into 4H-SiC takes place after an air annealing temperature of 500 ^{o}C as indicated by RBS analysis.

As for the Ru/6H-SiC film annealed in the air, oxidation is seen to commence at 400 ^{o}C and the oxide formed is RuO_2 as indicated by Raman spectroscopy. XRD analysis of the sample indicates the formation of a silicide of stoichiometry RuSi. However, RBS analysis of the sample does not corroborate the formation of this silicide. The reason for this anomaly might be that the atomic composition of Si in both RuSi and SiC is the same thereby making it difficult for RBS to distinguish between them.

For the Ru/4H-SiC thin film annealed in argon, there is an indication of commencement of oxidation, the formation of a silicide and inter-diffusion at the interface after annealing at 400 ^{o}C as evidenced from the RBS analysis of the sample. Raman analysis of the sample annealed at 900 ^{o}C also indicates the presence of a silicide and an oxide of stoichiometries Ru_2Si_3 and RuO_2 respectively.

In the case of the Ru/6H-SiC film annealed in argon, oxidation of Ru is observed after annealing at a temperature of 500 °C, diffusion of Ru into the SiC layer is seen to commence at 700 °C and no silicide formation is indicated from RBS analysis of the samples. SEM analysis of as-deposited thin film of Ru-6H-SiC and the sample annealed in argon at 500 °C indicates that the as-deposited thin film contains a mix of randomly oriented grains while the sample annealed at 500 °C is smooth which is generally an indication of the improvement in the grain quality of Ru or the microcrystalline nature of the ruthenium oxide formed during the annealing process.

In a vacuum, Ru diffusion and silicide formation are observed for the Ru/4H-SiC films annealed at 700 °C as evidenced from RBS analysis. Raman analysis of the Ru-4H-SiC film annealed in a vacuum at 1000°C indicates the formation of graphite flakes and a silicide of stoichiometry Ru_2Si_3.

For the Ru/6H-SiC film annealed in a vacuum, Ru diffusion is observed to take place after annealing a temperature of 800 °C, and formation of a silicide takes place at 600 °C as evidenced from RBS analysis. Raman analysis of the thin films annealed in a vacuum at 1000 °C indicates the formation of graphitic structures.

This investigation has shown that Ru diffuses through and reacts with SiC at certain temperatures in the three annealing environments namely air, argon and vacuum. The reaction of Ru with SiC leads to the formation of silicides. This reaction also produces graphite flakes in a vacuum annealing environment. This corrosive reaction may compromise the integrity of the SiC layer when it is used in TRISO particles in nuclear reactors. The temperature range of this investigation covers some of the operating temperatures of very high temperature nuclear reactors (VHTR). There have been a number of theories in the last three decades on the migration mechanism of fission products through SiC. In the case of Ag, which has been widely studied, the diffusion coefficients which have been calculated span 3 orders of magnitude and a number of theories have been proposed for its migration mechanism [2]. Some of these are grain-boundary and triple junction migration mechanisms, bulk diffusion and vapour or surface transport through pores and cracks [2,3,4]. However, up to now there has not been a definite proof in support of these migration mechanisms. The common agreement in these theories is that the concentration of the fission product on the SiC layer and thermal gradient will influence the diffusion behaviour of fission materials. From our investigation, it has been shown that annealing temperature and environment influence the on-set of diffusion and the type of reactions at the Ru-SiC interface.

The experimental results of our investigation have shown that the SiC layer in TRISOcoated fuel particles is not a perfect barrier to the diffusion of Ru. Therefore, there is a need to explore the possibility of replacing the SiC layer in TRISO particles with other materials such as zirconium carbide.

From the investigation of SBDs, it has been shown that Ru Schottky diodes made from 4H-SiC will remain operational, after annealing in vacuum, up to temperatures of above 1000 °C and that the diodes degrade at a very low temperature of 400 °C when annealed in air. Ru-4H-SiC

SBDs under argon annealing degrade at a temperature of 1000 °C. The degradation of the Ru/4H-SiC SBDs, when annealed in the air, is explained by the fact that there is a possibility of the formation of an oxide of Ru which is not conducting which leads to a high series resistance of the diode at the degradation temperature of 400 °C. In the case of argon annealing, the degradation of Ru/4H-SiC SBDs is due to the diffusion of Ru into 4H-SiC.

Under the same vacuum annealing condition of Ru/4H-SiC SBDs, the Ru/6H-SiC SBDs degrade at a much lower temperature of 800 °C. The IV data show that the Ru Schottky contact on 6H-SiC becomes ohmic at 900 °C, and the RBS spectrum indicates the formation of ruthenium silicide at this temperature. The transformation from Schottky contact to ohmic contact is due to the formation of graphite flakes at an annealing temperature of 900 °C and above.

In atmospheric annealing environment, the Ru/6H-SiC SBDs degrade at a higher temperature (700 °C) than that of Ru/4H-SiC SBDs (400 °C). This difference in degradation temperature may be explained by the fact that the 4H-SiC had an epilayer (while the 6H-SiC was bulk-grown) whose integrity might have been compromised by elemental interdiffusion and oxidation at the Ru/4H-SiC interface. Epilayers which are improperly grown have been found to have high defect densities of dislocations and stacking faults, interface defects, and tendency to crack.

Under argon annealing, there is very little difference in the degradation temperature between 4H-SiC and 6H-SiC-based diodes. From the SBD analysis, it is seen that the Schottky diodes degrade at higher temperatures when annealed in vacuum and argon while in air annealing degradation takes place at a very much lower temperature.

This investigation has broadly managed to link the electrical performance and failure mechanism of the SBDs with the processes occurring at the Ru-SiC interface such as solid state reactions, phase transformation, and diffusion at different annealing temperatures and in different environments.

For these results to be conclusive, further experiments need to be done to characterise the diodes by performing *in-situ* IV and CV measurements.

6.2 Future Work

In this investigation, the thin films and SBDs were annealed in the air and argon for 15 minutes, and in a vacuum for 60 minutes. Future work may need to explore the behaviour of the thin films and SBDs in an annealing environment that lasts for a number of days. This long annealing time will properly mimic the operating conditions of TRISO particles in nuclear reactors and application conditions of electronic devices in jet engines, car engines, and space rockets.

More additional work needs to be done to determine the performance of both Ru-6H-SiC and Ru-6H-SiC diodes during the annealing process. In this work all the electrical and physical characterisation were done after annealing the samples. In order to mimick real time operating behaviour, there is a need to do *in situ* physical and electrical characterisation of the thin films and electronic devices respectively.

If this real-time characterisation confirms the operational integrity of the diodes, especially those annealed in argon and a vacuum, at extreme temperatures then the next step will be to look at production methods of hermetically sealed SBDs. The final step will be to commercialise the SBDs.

6.3 Reference

[1] F.G. Di Lemma, J.Y. Colle, O. Benes, R.J.M. Konings, *A separate effect study of the influence of metallic fission products on CsI radioactive release from nuclear fuel*, Journal of Nuclear Materials 465, 499-508,(2015)

[2] T.M. Lillo, I.J. van Rooyen, *Associations of Pd, U and Ag in the SiC layer of neutron-irradiated TRISO fuel*, Journal of Nuclear Materials 460, 97–106, (2015).

[3] D. Shrader, S.M. Khalil, T. Gerczak, T.R. Allen, A.J. Heim, I. Szlufarska, D. Morgan, *Ag diffusion in cubic silicon carbide*, Journal of Nuclear Materials 408, 257–271,(2011).

[4] I.J. van Rooyen, M.L. Dunzik-Gougar, P.M. van Rooyen, *Silver (Ag) transport mechanisms in TRISO coated particles: A critical review*, Nuclear Engineering and Design 271, 180–188, (2014).